TECHNICAL QUARTERLY PROGRESS REPORT

Prepared By

Advanced Gas Turbine Systems Research
Clemson University Research Foundation

For

U. S. Department of Energy
National Energy Technology Laboratory

Contract No. DE-FC21-92MC29061

Reporting Period: July 1, 2002 to September 30, 2002

Advanced Gas Turbine Systems Research
South Carolina Institute for Energy Studies
Clemson, South Carolina

Technical Quarterly Progress Report
Advanced Gas Turbine Systems Research
Cooperative Agreement DE-FC21MC29061

July 1, 2002 to September 30, 2002

SUMMARY

The activities of the Advanced Gas Turbine Systems Research (AGTSR) program for this reporting period are described in this quarterly report.

The AGTSR program is now functioning under a time extension approved by DOE/NETL. The AGTSR completion date is set for June 30, 2003. During the time extension period, no new activities will be added to AGTSR. Research work will continue as the university subcontractors continue/complete their work and SCIES will provide the necessary oversite to assure progress is made. No new Membership, Workshop, Research Projects, Internships, Faculty Fellows or Special Studies will be initiated under AGTSR.

ADMINISTRATION

- The AGTSR/ATS Quarterly Technical Report for the reporting period of April to June 2002 was submitted to NETL on July 30, 2002. The report was submitted via hard copy and disk.
- The annual Industrial Review Board (IRB) meeting was held at SCIES on September 24-25, 2002. During the meeting, the financial status of the program and research contracts was reviewed. The remainder of the meeting was focused on the HEET/UTSR activities.
- Normal administrative functions required to monitor existing AGTSR contracts continued through the reporting period. The University of Central Florida research program (SR080) is having difficulty making progress. SCIES staff and the UCF PI will meet at the Workshop to be held at LSU on November 11-13, 2002 to determine a path forward.

RESEARCH

- Attachment I contains a listing of the AGTSR technical progress reports released during this reporting period.
- No new activities have been added.

ATTACHMENT I

AGTSR Progress Reports Received

July 1, 2002 – September 30, 2002

Aero-Heat Transfer	University of North Dakota Semi-Annual Report 11/01-5/02 Subcontract #00-01-SR086 **LINK TO REPORT**	"Characterization of Catalytic Combustor Turbulence and Its Influence on Vane and Endwall Heat Transfer and Endwall Film Cooling" *PI – Forrest Ames*
Aero-Heat Transfer	Texas A&M University Annual Report 8/31/02 Subcontract #01-01-SR094 **LINK TO REPORT**	"Rotating Heat Transfer in High Aspect Ratio Rectangular Cooling Passages with Shaped Turbulators *PI – J. C. Han*

Characterization of Catalytic Combustor Turbulence and its Influence on Vane and Endwall Heat Transfer and Endwall Film Cooling

Semiannual Report to AGTSR

By Forrest E. Ames

Mechanical Engineering Department

University of North Dakota

Grand Forks, ND 58202-8359

June 2002

Characterization of Catalytic Combustor Turbulence and its Influence on Vane and Endwall Heat Transfer and Endwall Film Cooling

Executive Summary

Objective. The objective of the current investigation is to help reduce the risk associated with developing new gas turbine systems with advanced low NOx combustors. The current experimental investigation, which is being conducted at the University of North Dakota, involves developing a heat transfer and film-cooling database for two cascade geometries. One geometry involves a linear cascade, which uses a fully loaded vane design and the second cascade has a strongly contracting inlet and features an aft loaded vane design. The large-scale low speed cascades used in this study have eleven to one scaling to allow well-resolved heat transfer and film cooling measurements. The current analytical investigation, which is being conducted at Rolls Royce, involves developing predictions for the heat transfer and film cooling database and using the computational models to transfer the results to engine-like conditions. The heat transfer and film cooling data are being acquired over chord exit Reynolds numbers ranging from 500,000 to 2,000,000 using up to five different turbulence inlet conditions tested over two separate cascade geometries.

The computational predictions are being conducted using a 3-D RANS method, which uses a multiblock method to speed computation convergence time. Vane and endwall heat transfer predictions are being made for both cascade geometries by the Aerothermal Methods Group at Rolls Royce. Selected results will be transferred to engine relevant conditions using the code.

Experimental Effort. The experimental effort has resulted in acquisition of full surface heat transfer data on the endwall of the conventionally loaded cascade for four turbulence generator geometries at Reynolds numbers ranging from 500,000 to 2,000,000. Inlet boundary layer profiles and turbulence spectra have been acquired for all test conditions. Midline vane heat transfer measurements have been acquired for six turbulence conditions taken over the full range of Reynolds numbers. These data have are viewed as an excellent test case for grounding predictive methods for vane and endwall heat transfer.

Work continues on the current cascade to obtain endwall film cooling distributions for both two rows of film cooling holes and for a slot. The film cooling supply system has been completed and the film cooling plenums have been installed. One of the problems we have encountered in developing our system includes uncovering and fixing a temperature stratification in the film cooling supply system. This anomaly was reduced by adding a mixer for our film cooling air upstream of our plenum distribution holes. Another problem we are currently encountering is related to having an uncooled laboratory. During the summer temperatures can rise to well over 30 C inside our laboratory and cooling water temperatures can rise to over 20 C. Since we use 29 C and 37 C start narrow band liquid crystals, we have difficulty maintaining the inlet air at a low enough temperature to acquire the lower effectiveness levels. However, we are planning to acquire endwall heat transfer measurements with film cooling through the remainder of the summer and will defer the film cooling measurements until cooler weather arrives.

Contoured Endwall Cascade Fabrication. The contoured endwall cascade is nearing completion and we expect to begin qualification measurements by the beginning of September. This summer we have cast and assembled the instrumented vanes for heat transfer and pressure distributions, laid up the instrumented endwall surface, assembled and installed the bleed flow

adjustments, and are currently in the process of adding the tailboards and installing the slave vanes. We have already completed both the nozzle and the turbulence generator casing to accommodate the contoured inlet.

Analytical Effort. We have had a significant setback in the analytical portion of this contract due to changes in personnel at Rolls Royce. In the last half year the engineer at Rolls Royce responsible for the project, Eric Bermingham, and the technical lead on the project, Dr. Edward Hall have both left Rolls Royce. Unfortunately, the majority of the analytical work has not been completed. On the brighter side, the new CFD specialist on the project, Dr. Todd Simmons comes highly recommended. Additionally, due to the problems encountered by the change of employment of two key people on the subcontract, we are currently focusing on developing analytical solutions for vane and endwall heat transfer for the two cascade geometries.

Graduate Student Education. Three graduate students are currently associated with the project. Pierre Barbot who was responsible for acquiring and analyzing the endwall heat transfer measurements is currently working as a CNA to gain medical experience for entry into medical school and is working part time on this master's thesis. Chao Wang, an Engineering Ph.D student from China, is currently responsible for acquiring endwall film cooling measurements and endwall heat transfer measurements with film cooling. Chao Wang was also responsible for acquiring all the hot wire anemometry data to date on the cascade. Chao is being supported ¼ time through the UND's School of Engineering and Mine's Energy Engineering Ph.D program and ¼ time by the current AGTSR contract. In addition, this spring we were able to attract Matthew Argenziano to work on the program. Matt is responsible for the new contoured endwall cascade and is expected to acquire vane and endwall heat transfer data with the cascade. Matt is receiving half-time support through the University of North Dakota.

Presentations, Papers, and Information Requests. Through the efforts of AGTSR and the PI information about this research is spreading throughout the gas turbine community. On February 9th, I was invited to make a presentation to Catalytica Energy Systems in Phoenix, Arizona. On the 25th and 26th of February a poster entitled "The Influence of Catalytic and Dry Low NOx Combustor Turbulence on Vane and Endwall Heat Transfer" was presented at the NETL sponsored Turbine Power Systems Conference in Galveston, Texas. Addtionally, two papers covering the vane and endwall heat transfer measurements are attached to this report. These papers were presented at Turbo Expo 2002 in Amsterdam and have been accepted to appear in the ASME Journal of Turbomachinery. In addition, Dr. Thomas Praisner from Pratt and Whitney requested information on the vane coordinates and turbulence conditions in February to conduct benchmarking tests on an in-house predictive method. Additionally, two abstract have been submitted and accepted for Turbo Expo 2003 in Atlanta and are attached to the end of this document.

Attachments

Ames, F. E., Wang, C., and Barbot, P. A., "Measurement and Prediction of the Influence of Catalytic and Dry Low NOx Combustor Turbulence on Vane Surface Heat Transfer," ASME Paper No. GT-2002-30524.

Ames, F. E., Barbot, P. A., and Wang, C. "Effects of Aeroderivative Combustor Turbulence on Endwall Heat Transfer Distributions Acquired in a Linear Vane Cascade," ASME Paper No. GT-2002-30525.

Abstract 1:

Effects of Catalytic and Dry Low NOx Combustor Turbulence on Endwall Heat Transfer Distributions

Abstract No. GT2003-38507

By F.E. Ames, P.A. Barbot, and C. Wang

Abstract

Endwall heat transfer distributions taken in a large-scale low speed linear cascade facility are documented for mock catalytic and dry low NOx (DLN) combustion systems. Inlet turbulence levels range from about 1.0 percent for the mock Catalytic combustor condition to 14 percent for the mock dry low NOx combustor system. Stanton number contours are presented at both turbulence conditions for Reynolds numbers based on true chord length and exit conditions ranging from 500,000 to 2,000,000. Catalytic combustor endwall heat transfer shows the influence of the complex three-dimensional flow field, while the effects of individual vortex systems are less evident for the mock dry low NOx cases. Turbulence scales have been documented for both cases. Inlet boundary layers are relatively thin for the mock catalytic combustor case while inlet flow approximates a channel flow with high turbulence for the mock DLN combustor case. Inlet boundary layer parameters are presented across the inlet passage for the three Reynolds numbers and both the mock catatlytic and DLN combustor inlet cases. Both midspan and 95 percent span pressure contours are included. This research provides a well-documented database taken across a range of Reynolds numbers and turbulence conditions for assessment of endwall heat transfer predictive capabilities.

Abstract 2:

Measurement and Prediction of Heat Transfer Distributions on an Aft Loaded Vane Subjected to the Influence of Catalytic and Dry Low NOx Combustor Turbulence

Abstract No. GT2003-38509

By F.E. Ames, M. Argenziano, and C. Wang

Abstract

Aft loaded vane designs can have an impact on surface heat transfer distributions by accelerating boundary layers for a greater portion of the suction surface. New combustion systems developed for low emissions have produced substantial changes to the characteristics of inlet turbulence entering nozzle guide vanes. This paper documents heat transfer rates on an aft

loaded vane subject to turbulence generated by mock combustion system configurations representative of recently developed catalytic and dry low NOx combustors. Four different inlet turbulence conditions with levels ranging up to 14 percent are documented in this study and vane heat transfer rates are acquired at vane exit chord Reynolds numbers ranging from 500,000 to 2,000,000. Heat transfer distributions show the influence of turbulence level and scale on heat transfer augmentation and transition. Cascade aerodynamics are well documented and match pressure distributions predicted by a commercial CFD code for this large scale low speed facility. The aft loaded vane pressure distribution exhibits a minimum value at about 60 percent arc on the suction surface. This comprehensive vane heat transfer data set is expected to represent an excellent test case for vane heat transfer predictive methods. Predictive comparisons are shown based on a two-dimensional boundary layer code using an algebraic turbulence model for augmentation as well as a transition model.

Proceedings of
ASME TURBO EXPO 2002
June 3-6, 2002, Amsterdam, The Netherlands

GT-2002-30524

MEASUREMENT AND PREDICTION OF THE INFLUENCE OF CATALYTIC AND DRY LOW NO_X COMBUSTOR TURBULENCE ON VANE SURFACE HEAT TRANSFER

Forrest E. Ames, Chao Wang, and Pierre A. Barbot
University of North Dakota
Mechanical Engineering Department
Grand Forks, ND, USA

ABSTRACT

New combustion systems developed for low emissions have produced substantial changes to the characteristics of inlet turbulence entering nozzle guide vanes. This paper documents the characteristics of turbulence generated by mock combustion system configurations representative of recently developed catalytic and dry low NOx combustors. Additionally, heat transfer rates are determined on the surface of a vane subjected to inlet turbulence generated by these mock combustor configurations. Six different inlet turbulence conditions with levels ranging up to 14 percent are documented in this study and vane heat transfer rates are acquired at vane exit chord Reynolds numbers ranging from 500,000 to 2,000,000. Heat transfer distributions show the influence of turbulence level and scale on heat transfer augmentation and transition. Cascade aerodynamics are well documented and match pressure distributions predicted by a commercial CFD code for this large scale low speed facility. The vane pressure distribution could be characterized as a conventional or fully loaded distribution. This comprehensive data set on vane heat transfer is expected to represent an excellent test case for vane heat transfer predictive methods. Predictive comparisons are shown based on a two-dimensional boundary layer code using an algebraic turbulence model for augmentation as well as a transition model.

NOMENCLATURE

C	vane true chord length, m
Cp	specific heat at constant pressure, J/(kg K)
C_μ	A k – ε model constant, $C_\mu = 0.09$
D	vane leading edge diameter or effective diameter based on $D = 3.62\ U_\infty/(dU_\infty/dx)$
D_v	A near wall viscous damping function
$E_1(f)$	one dimensional spectrum as a function of frequency, f, of the streamwise fluctuation velocity, u', m^2/s
$E_1(k_1)$	one dimensional energy spectrum function, $E_1(k_1) = U\ E_1(f)/2/\pi$, m^3/s^2
f	frequency, 1/s
h	heat transfer coefficient, $W/m^2/K$, based on T_r and T_w
k	thermal conductivity, W/m/K
K	free stream acceleration parameter, $K = \nu/U_\infty^2 \bullet (dU_\infty/dx)$
k_1	wavenumber, $k_1 = 2\pi f/U$, m^{-1}
Lu	energy scale, $Lu = 1.5\ \|u'\|^3/\varepsilon$, m
Lx	longitudinal integral scale of u' fluctuation, m
Nu	Nusselt number, hD/k
P	Pressure, Pa
Pr	Prandtl number, $Pr = \rho Cp\nu/k$
Pr_t	turbulent Prandtl number, see Eqn. (13)
Re_C	true chord Reynolds number, based on exit conditions
St	Stanton number, $St = h/(\rho Cp U_\infty)$
Tu	turbulence level, $Tu = \|u'\|/U_\infty$
TRL	turbulence, Reynolds number, length scale parameter for correlating stagnation region heat transfer, $TRL = Tu \bullet Re_D^{5/12} \bullet (D/Lu)^{1/3}$
u'	streamwise fluctuation velocity, m/s
|u'|	rms streamwise fluctuation velocity, m/s
Y	normal distance from test surface, m

Greek Letter Symbols

ε	turbulent dissipation rate, m^2/s^3
η	the Kolmogoroff micro length scale, $\eta = (\nu^3/\varepsilon)^{1/4}$, m
ν	kinematic viscosity, m^2/s
ν_M	eddy diffusivity for momentum, m^2/s
ρ	fluid density, mass per unit of volume, kg/m^3

Subscripts

0	refers to value at same position for low turbulence condition
i	refers to "inner region" of the boundary layer
o	refers to "outer region" of the boundary layer
s	refers to static condition
t	refers to total or stagnation condition
∞	evaluated in the free stream

INTRODUCTION

Turbulence from combustion systems has a very large influence on heat transfer distributions of first stage vanes. New strategies for achieving very low NOx levels have produced a variety of new combustor technologies, which have a significant influence on the turbulence levels at the entrance of high-pressure turbines. Consequently, gas turbine engineers are being challenged with developing component cooling schemes, which match the heat load requirements for these new systems. In order to achieve reliable yet efficient cooling schemes for first vanes, gas turbine engineers must be equipped with knowledge of the turbulence characteristics produced by these new low NOx combustion systems. They also need an understanding of the impact that turbulence with these characteristics has on heat transfer distributions.

The objective of this research has been to investigate the characteristics of turbulence generated by new low NOx combustion systems and to acquire heat transfer distributions on the surface of a vane and endwall in a linear cascade facility. Consequently, a mock dry low NOx (DLN) combustion system was designed and fabricated based on two industrial representative configurations. A mock catalytic combustion system (CC) was also developed based on an industry representative catalytic surface. In addition, for comparison purposes turbulence was generated with a low turbulence (LT) configuration, a mock aero-derivative combustion (AC) system at two upstream positions (ACS), and a biplanar square-mesh square bar grid (Grid). Turbulence levels and scales have been comprehensively documented for the six turbulence configurations. Vane heat transfer distributions were taken over a four to one range of chord exit Reynolds numbers and provide a comprehensive test case to ground heat transfer predictive capabilities.

BACKGROUND

Heat transfer on the central portion of a turbine vane is predominately two-dimensional. Consequently, heat transfer on a vane surface can be discussed in terms of the different regimes of flow. In addition to the specific velocity distribution on the surface of a vane, inlet turbulence boundary conditions are the major driver of heat transfer augmentation and transition on smooth airfoils. Therefore, this background section will discuss typical inlet turbulence conditions from combustion systems, stagnation region heat transfer augmentation, heat transfer augmentation to the laminar region on the pressure surface, transition, and augmentation to the turbulence boundary layer.

Combustor Turbulence. Values of turbulence intensity at the exit of gas turbine combustion systems reported in the literature have ranged from about 7 percent to nearly 30 percent (see Dils and Follansbee [1], Zimmerman [2], Bicen and Jones [3], Ames and Moffat [4], Moss and Oldfield [5], Goebel et al. [6], Zhang and Glezer [7], Ames [8], and Van Fossen and Bunker [9]. Ames [8] measured turbulence downstream from a mock aero-derivative combustor and suggested that turbulence scale, Lu, was typically 1/3 to ½ of the inlet passage. For most conventional combustion systems, which depend on large-scale recirculation to stabilize flames, turbulence level seems to depend on length to height ratio of the combustor and on the main flow to turbine inlet contraction ratio. For example in this present paper, the turbulence intensity downstream from the mock dry low NOx (DLN) combustor is about 14.3 percent for the two to one combustor area to inlet flow contraction ratio. Van Fossen and Bunker [9] report turbulence levels of 27 percent downstream from their DLN combustion system with its 1 to 0.9 combustor flow to inlet area contraction. Since the local fluctuation velocity and scale are the main drivers for heat transfer augmentation and transition, understanding turbulence conditions in turbine passages is critical for accurate predictions.

Stagnation Region Heat Transfer Augmentation. Stagnation regions often have the highest heat transfer rates on a turbine airfoil. Relative heat transfer rates in stagnation regions tend to increase with lower chord Reynolds numbers and higher inlet to exit velocity ratios. Inlet turbulence can produce augmentation levels more than 50 percent greater than the low turbulence baseline level. Recent research (Ames and Moffat [4] and Van Fossen, Simoneau, and Ching [10]) has shown that both scale and turbulence intensity have a significant impact on stagnation region heat transfer. Hunt [11] predicted that relatively small-scale turbulence is amplified by vortex stretching resulting from the strain field applied by a stagnation region flow. Britter, Hunt, and Mumford [12] later corroborated this theory. Ames and Moffat applied Hunt's work to the development of an algebraic eddy viscosity model and a correlating parameter, which are used to predict and correlate the results of this experimental investigation.

Laminar Region Heat Transfer Augmentation. In spite of significant disturbances due to free-stream turbulence, the pressure surface of a vane is typically laminar when exit chord Reynolds numbers are below one million due to the high flow field acceleration. However, a significant level of heat transfer augmentation can take place due to mixing caused by the external turbulence. For example, Arts, et al. [13] found augmentation levels of up to 100 percent on the laminar portion of a vane subjected to 6 percent grid turbulence. Ames [8] found laminar augmentation scaled on turbulence intensity, chord to length-scale ratio to the $1/3^{rd}$ power, and Reynolds number to the $1/3^{rd}$ power. He suggested that this $1/3^{rd}$ power Reynolds number scaling was consistent with no noticeable amplification of turbulence occurring. However, his Reynolds numbers range was limited. Wang, Goldstein, and Olson [14] looked at the effect of high turbulence levels with large scale on turbine blade mass transfer. The suction surface of their blade had a favorable pressure gradient to mid chord and they found increasing mass transfer augmentation and earlier transition with increasing turbulence level and Reynolds number. The pressure surface of their blade had an overspeed region, which made comparative assessment of parametric affects more difficult.

Transition. Mayle [15] presented a relatively comprehensive account of transition on the surface of a turbine airfoil. He suggests onset of transition is largely affected by the momentum thickness Reynolds number and turbulence level. However, he indicates that turbulent scale likely impacts transition onset as well. In addition, transition is suppressed on surfaces with high acceleration rates, where K is greater than 3E-6, even at high levels of turbulence. Zhang and Han [16] looked at the effect of grid generated turbulence on heat transfer augmentation and transition on a turbine blade. Their results showed that at roughly equivalent turbulence levels, their finer grid produced earlier transition on the suction surface. This study indicates that turbulent length scale may have an impact on transition onset. In addition, Boyle and Simon [17] suggest that Mach number significantly influences transition length.

Turbulent Boundary Layer Augmentation. Ames and Moffat [4] and Thole and Bogard [18] have shown that relatively large-scale turbulence has a reduced influence on turbulent boundary layer heat transfer augmentation. Consequently, thin turbulent boundary layers on first vane suction surfaces are typically not

strongly influenced by the relatively large-scale turbulence produced by combustion systems.

EXPERIMENTAL APPROACH

This heat transfer research has been conducted in the University of North Dakota's large-scale low speed cascade facility. This facility is configured in a steady state blow down arrangement. The cascade test section is shown schematically in figure 1. Air enters the facility through a large inlet filter, which protects the hot wires from fouling. The wind tunnel is powered by a 45 kW blower capable of providing 6.6 m^3/s of air at a static pressure rise of 5000 Pa. The blower outlet flow is directed through a two stage multivane diffuser section to distribute and diffuse the flow prior to entering a heat exchanger. The heat exchanger system, which uses a cooling water recirculation system, helps to provide a steady and controllable inlet air temperature. The flow is further conditioned downstream of the heat exchanger in a four section screen box. The low turbulence baseline configuration uses a 3.6:1 area ratio two-dimensional nozzle to further accelerate the air prior to entrance into the linear vane cascade test section.

The cascade test section used in this study is based on an eleven times scale mid span vane profile representative of a modern mid-sized industrial gas turbine and is displayed in figure 2. The vane profile was designed specifically for incompressible flow and has a velocity distribution, which is consistent with current conventionally or fully loaded vanes in industrial engines. The cascade test section, shown in figure 1, was designed to produce accurate two-dimensional aerodynamics with a four-vane three-passage configuration. The cascade has inlet bleeds designed along 2-D streamlines to allow for the proper flow around the top and bottom vanes. These inlet bleed sections were calculated using a 2-D FLUENT [19] simulation. These inlet bleeds provide control of the inlet flow uniformity, which is verified by a row of 30 static pressure taps placed 7 cm upstream from the vane leading edge plane. The cascade also has flexible exit tailboards, which can be shaped along exit streamlines to control of the exit flow periodicity. The cascade has a row of exit taps one-quarter axial chord downstream to monitor the exit flow periodicity. Ten probe access ports are provided along the row of inlet static pressure taps to measure inlet temperature and total pressure and to survey inlet turbulence characteristics.

The eleven times scale vane has a true chord of 47.8 cm and an axial chord of 25.0 cm. The vanes have a 38.4 cm spacing and a height of 25.4 cm. The diameter of the leading edge is 5.59 cm and the diameter of the trailing edge is 0.98 cm. The stagger angle of the vane is 55.1 degrees and the calculated air exit angle is 73.4 degrees.

The cascade was run at exit Reynolds numbers based on true chord of 500,000, 1,000,000, and 2,000,000. Exit velocity and pressure were calculated based on inlet total pressure and temperature and the average exit static pressure at the row of exit static pressure ports. This range of Reynolds numbers is consistent with values for small to medium industrial or propulsion gas turbine engines.

Turbulence Generators. This study was designed to investigate turbulence characteristics representative of modern low NOx combustion systems and their influence on vane heat transfer. Two separate low NOx configurations were developed. One configuration represented a conventional dry low NOx combustion system and the other a catalytic combustion system. In addition, an aeroderivative combustion system was developed to provide turbulence with characteristics, which are representative of with many current engines and has been documented in the literature. All three mock combustion systems used the same combustor liner and nozzle configuration, which is shown with the aero-derivative geometry in figure 3. This liner geometry replaces the 3.6:1 area ratio nozzle for the high turbulence test cases. For the low NOx combustor configurations the side panels of the mock combustor system are replaced with solid panels and either the swirler arrangement or the catalytic surface are attached at the back panel position. The swirler arrangement for the conventional DLN is shown in figure 4 while the mock catalytic surface is shown in figure 5.

The back panel for the mock DLN combustor consists of 10 swirlers. Each swirler is fabricated from a 20.3 cm schedule 40 PVC pipe and has a 5.1 cm centerbody. Each swirler has 12 vanes, which are essentially a 36 degree projection of a 45 degree slice through the pipe. The design of the low NOx combustion system is a compromise between the model dry low NOx system published by Van Fossen and Bunker [9] and a green thumb combustor system of Rolls Royce [19]. The Van Fossen mock combustor had a swirler flow to combustor liner flow area ratio of 33 percent and a vane inlet flow to combustor liner flow area ratio of 90 percent. The swirlers used by Van Fossen had 45 degree vanes. The Rolls Royce green thumb combustor has a swirler to combustor flow area ratio of 40 percent and a vane inlet area to combustor flow area ratio of 33 percent. The swirler vane angles range from 45 to 60 degrees. The current design has a swirler flow to combustor flow ratio of 46 percent and an inlet to liner flow ratio of 50 percent.

The mock catalytic combustion system was crafted after the system used by Catalytica. Catalyica's foil has a serpentine groves running across it. These grooves are spaced 2.2 mm apart. As the foils are folded back across each other and rolled together to form a round porous structure, grooves from one side of the foil cross with grooves from the adjacent foil helping to promote mixing. UND's mock catalytic combustor is made from evaporative cooling pads, which contain the same type of crossing grooved channels. The evaporative cooling pads are 12 times the size of the actual catalytic combustor surface. This scaling is very similar to the vane scaling, which is 11 times the actual size.

Turbulence was also generated using a square bar square mesh biplanar grid. The grid used 1.27 cm square bars, which were spaced on 6.35 cm centers producing a 64 percent open area grid. The grid was held 63.5 cm or 10 mesh lengths upstream of the vane leading edges for the heat transfer tests. The grid was held in a 25.4 cm by 127 cm rectangular spool section, which was 91.5 cm long and attached between the 3.6:1 area ratio nozzle and the cascade test section.

In addition, a second level of turbulence was generated with the mock aero-combustor turbulence generator using the 91.5 cm long, 25.4 cm wide, and 127 cm high rectangular spool as an extended development length. For this condition the spool section was placed between the mock combustor and the inlet to the cascade to allow for the decay of turbulence.

Vane Pressure Distribution. The third vane from the bottom was used to acquire the heat transfer and pressure distributions. This "instrumented" vane can be inserted through a machined hole in the acrylic endwall where it is held in place using a flange. The pressure vane was cast out of epoxy with 82 pressure tubes incrementally spaced along and cast adjacent to its surface. Static pressure taps were fabricated by drilling through the epoxy surface into the brass tube with a 0.8 mm diameter drill bit. The baseline pressure distribution for the low turbulence case is shown in figure 6 where it is compared to a prediction using FLUENT. On this figure negative surface distance is

taken from the calculated stagnation point (0 cm) along the pressure surface toward the trailing edge and positive surface distance is determined along the suction surface. The viscous prediction matches the data with precision. Overall, the comparison is excellent and provides confidence in the quality of the midspan aerodynamics produced by the cascade. Developing accurate aerodynamics is critical to producing a heat transfer database, which is valuable for understanding the impact of new combustion systems and for grounding predictive methods.

Heat Transfer Vane Description. The heat transfer vane has a polyurethane foam core with a 1.6 mm epoxy shell cast around it. The present heat transfer data were acquired using the 52 fine wire chromel-alumel thermocouples cast around the surface. The vane was covered with a 0.023 mm Inconel foil bonded to a 0.127 mm sheet of Kapton and backed with 0.05 mm of high temperature acrylic adhesive. The 101.6 cm by 25.4 cm foil has 6.35 mm by 0.5 mm copper bus bars soft soldered to its end to evenly distribute the large DC current used to produce the constant surface heat flux. These copper bus bars are recessed into the surface of the epoxy near the trailing edge on both the pressure and suction surfaces. The resulting Inconel foil, as adhered to the epoxy surface, produces an aerodynamically smooth visually attractive heat transfer surface. The heating ends 1.3 cm from the trailing edge on both the pressure and suction surfaces.

Heat transfer baselining tests were conducted for the low turbulence condition over the four to one range in Reynolds numbers. Prior to heating the foil, the recovery temperature distribution was acquired for each Reynolds number. Subsequently, the midline surface temperature distribution was acquired at the desired surface heat flux condition. Surface heat flux was determined by measuring the voltage across and the current through the heater. The heater current was determined using a precision shunt resistor. Only radiation losses were accounted for. Due to the relatively thick and very low conductivity polyurethane core, conduction through the vane was ignored. Conduction along the surface of the foil was also ignored due to the thin Inconel foil. Radiation losses were estimated using the local surface temperature radiating to the inlet total temperature using a foil emissivity of 0.21 and assuming a blackbody background. As a consistency check heat transfer data were acquired at one-half and full power. The resulting root mean square difference was only 0.5 percent with a maximum variation of 1.7 percent.

A comparison between the experimentally determined Stanton number distribution and a finite difference boundary layer calculation (STAN7 Kays [21]) using the predicted pressure distribution is shown in figure 7 for the three low turbulence cases. Notice that all three distributions are laminar. The comparisons between the predicted and experimental Stanton number distributions are generally better than 10 percent and give confidence in the experimental technique.

Data Acquisition. Pressures were acquired using two Rosemount Smart Pressure Transmitters scaled to ranges of 250 and 5000 Pa full scale with 0.1 percent of scale accuracy. Both transmitters were read for each pressure and the most sensitive reading was kept. Pressures were scanned using a homemade miniature solenoid valve system and were referenced to the inlet total pressure. Transmitters were zeroed at the beginning of each use to minimize uncertainties due to drift. Voltage outputs for both the pressure transmitters and for the chromel-alumel thermocouples were scanned and read using an HP 3497A data acquisition system. The data acquisition unit has an integral voltmeter with 1 μV sensitivity. Thermocouples were all connected through a passive constant temperature junction and were referenced using an ice bath. Hot wires were powered, low pass filtered, bucked and gained using a two channel TSI ISA 300 hot wire anemometry bridge. Raw signals were read with a PC based high-speed data acquisition card with 12 bits of resolution. Mean velocities were acquired at a data acquisition rate equivalent to about three integral time scales. Velocity time records for spectral analysis were acquired in 40 sets of 8192 samples and post processed.

Data Uncertainties. Estimates for the uncertainty in heat transfer, pressure, velocity, and turbulence measurements were determined using the root sum square method described by Moffat [22]. Based on a data reduction program perturbation method, Nth order uncertainty in reported local Stanton number ranged to plus or minus 5 percent at a 95 percent confidence interval. The uncertainty estimate for run-to-run comparisons was estimated at plus or minus 3 percent. Uncertainty in the local vane surface static pressure was estimated at a maximum of 2.5 percent. Exit velocity was determined at a precision of 2 percent. The uncertainty in turbulence level for the single wire was estimated to be 3 percent of the reported value. The experimental error in turbulent scale is estimated to be 11 percent. All uncertainty estimates are quoted for a 95 percent confidence interval.

Inlet Conditions and Turbulence Characteristics. A total of six different turbulence conditions were developed for this midspan heat transfer investigation. Both heat transfer data and turbulence measurements were taken for all turbulence conditions and Reynolds numbers. Velocity and turbulence data were acquired at the midspan of the inlet at five positions distributed evenly across one passage 7 cm upstream from the leading edge plane of the vanes. The turbulence level (Tu), average midspan velocity (U), integral scale (Lx), energy scale (Lu), and dissipation (ε) were determined for each condition and averages are presented in Table 1. Mean velocity and turbulence intensity were determined from 8192 data samples acquired at a time increment equal to about two or three integral time scales. Turbulent scales and dissipation rates were determined from 40 records of 8192 points taken at 10 to 35 kHz depending on the cascade inlet velocity. This allows for better statistical resolution of the power spectrum at the lower wavenumbers. The longitudinal integral scale was determined using Taylor's hypothesis by multiplying the integral time scale by the local convective velocity. The integral time scale was determined by integrating the autocorrelation in time to the first zero crossing. The autocorrelation was calculated using an inverse FFT of the average power spectral density function of the velocity time records.

The energy scale (or dissipation scale of Hancock and Bradshaw [23]), Lu is a macro scale of turbulence estimated from 1.5 times the cube of the rms value of u' divided by the dissipation rate.

$$Lu = 1.5\,|u'|^3/\varepsilon \qquad (1)$$

The dissipation rate is determined from the inertial subrange of the u' power spectrum. Hinze [24] suggests that in the inertial subrange of a turbulent spectrum for u' the spectrum function can be related to the dissipation rate and the wavenumber.

$$E_1(k_1) = 18/55\ A\ \varepsilon^{2/3}\ k_1^{-5/3} \qquad (2)$$

Ames and Moffat [25] suggest that the constant A be taken as 1.62. The energy scale is quite useful because as Hinze [24] suggests, the dissipation rate alone determines the spectrum from the start of the inertial subrange to the end of the dissipation range. Also, since the

integral of the one-dimensional spectrum of u' is equal to $|u'|^2$, the turbulence intensity, local velocity, and energy scale provide a quantitative description of an energy spectrum. A typical one-dimensional spectrum of u' is shown in figure 8 as taken downstream from the mock aero-derivative turbulence generator.

The circumferential uniformity of the streamwise fluctuation velocity, |u'|, and the dissipation level were quite good across the inlet of the cascade for the four highest turbulence levels generated. The grid turbulence dissipation level and |u'| varied by less than 5 percent across the survey plane. The dissipation level and |u'| for the mock aeroderivative combustor varied by no more than 10 percent. The mock DLN combustor produced a dissipation level which was uniform within 11 percent and a |u'| level which was uniform within 15 percent.

HEAT TRANSFER RESULTS

This section examines the vane surface heat transfer results both qualitatively and quantitatively for the influence of turbulence, scale, and Reynolds number on heat transfer augmentation and location of transition. First, the qualitative effects of the turbulence on augmentation and location of transition will be observed. Next, the level of augmentation in the laminar regions of the flow will be examined quantitatively in terms of turbulence level, scale and Reynolds number. Finally, heat transfer predictions will be made using STAN7 [21], the augmentation model of Ames, Moffat, and Kwon [25], and the transition model of Mayle [15].

Stanton Number Results. Stanton number distributions are presented in figures 9 through 11 for all six turbulence conditions for exit chord Reynolds numbers of 500,000, 1,000,000, and 2,000,000. The figures plot Stanton number versus surface distance with negative surface distance taken over the pressure surface and positive surface distance taken over the suction surface. The turbulence intensities quoted in the figures have been adjusted to account for the decay, where $Tu(x) = 1/[1/Tu(0) + x/(2\ Lu)]$. Figure 9 presents the distributions of the six turbulence conditions for the 500,000 Reynolds number case. Here the low turbulence (LT) case shows laminar flow over the entire surface. The catalytic combustor produces a turbulence level of only 1.0 percent with about a 2 cm energy scale (Lu) and shows little effect from the turbulence. This low turbulence level produced by the catalytic combustor has significance for heat transfer designs as flow over the majority of the vane surface will be laminar. Turbulence produced by the grid and the aero-combustor with spool (ACS) significantly augments laminar heat transfer on the pressure surface and stagnation region and leads to transition on the suction surface. Notice that the grid condition transitions earlier than the aero-combustor with spool in spite of the latter's higher turbulence level. This slightly earlier transition is likely the result of the grid turbulence's smaller scale and occurs at all three Reynolds numbers. This observation is consistent with the expectations of Mayle [15]. Results for the mock dry low NOx (DLN) and aero-combustor (AC) show similar trends but higher heat transfer augmentation in the laminar flow regions and earlier transition on the suction surface. Notice that the smaller scale turbulence of the mock AC compensates for the slightly higher turbulence level of the mock DLN combustor in terms of laminar augmentation and transition location.

Figure 10 presents Stanton number distributions for six turbulence conditions for the 1,000,000 chord Reynolds number case. Qualitatively the trends for the six turbulence cases are very similar to the lower Reynolds number data. However, laminar region augmentation levels are higher, suction surface transition occurs at an earlier location, and the AC and DLN cases show signs of the initiation of transition at a surface distance of about –0.3 m. Additionally, at this higher Reynolds number the turbulent boundary layer Stanton numbers on the suction surface now approach the level of heat transfer in the stagnation region. Figure 11 presents Stanton number distributions for the 2,000,000 chord Reynolds number case. Again the trends are qualitatively similar but laminar augmentation levels are higher and suction surface transition occurs even earlier. Also, the four higher turbulence cases (DLN, AC, ACS, and Grid) show signs of transition on the pressure surface at a surface location of about –0.22 m. For this higher Reynolds number case the catalytic combustor now shows some laminar augmentation on the pressure surface and the start of transition on the suction surface at a surface arc of 0.31 m. At this Reynolds number the turbulent boundary layer Stanton numbers on the suction surface exceed those of the laminar stagnation region.

Pressure Surface Heat Transfer Augmentation. Heat transfer augmentation to the pressure surface is presented as $(St-St_0)/St_0$ versus surface distance in figures 12 through 14. Figure 12 presents the 500,000 chord Reynolds number case. The pressure surface or negative surface arc shows a rising increase past the stagnation region and a relatively steady value further downstream past a surface arc of –0.1 m. This behavior indicates laminar augmentation due to turbulence. The augmentation levels at –0.2 m are about 6 percent for the mock catalytic system, 36 percent for the grid and aerocombustor with spool, and about 58 percent for the aerocombustor and DLN combustor. The increase on the suction surface is of course due to transition. Figure 13 shows the fractional increase in Stanton number for the 1,000,000 Reynolds number case. The majority of the pressure surface shows laminar behavior. However, these augmentation curves show a change in behavior toward the aft end of the surface with upturn in augmentation rate. This behavior is consistent with the start of transition on the pressure surface and it occurs for the four highest turbulence levels. The laminar augmentation levels at –0.2 m are about 14 percent for the mock catalytic combustor, 46 percent for the grid and aero-combustor with spool, and 75 percent for the aero and DLN combustors. Figure 14 shows Stanton number augmentation for the 2,000,000 Reynolds number case. The augmentation curves suggest transition starts at about –0.3 m for the grid and aero-combustor with spool and at –0.2 m for the aero and DLN combustors. Since the onset of transition is similar for the grid and aero-combustor with spool, while the scale and turbulence level is somewhat different, these heat transfer data sets may be useful for testing transition models. Further, the laminar augmentation levels at –0.2 m are about 22 percent for the catalytic combustor, 64 percent for the grid and aero-combustor with spool and about 98 percent for the aero and DLN combustors. Augmentation noticeably increases with Reynolds number and turbulence intensity. Comparisons between the grid and aero-combustor with spool suggest that given similar turbulence levels and Reynolds number, augmentation increases with decreasing scale.

Ames [8] suggested that heat transfer augmentation to a laminar boundary layer should scale on turbulence intensity (Tu), Reynolds number to the 1/3rd power and energy scale (Lu) to the negative 1/3rd power. That is $(St-St_0)/St_0 \propto Tu\ Re_C^{1/3}\ (C/Lu)^{1/3}$. This implies that the dissipation of the turbulence adjacent to a pressure surface boundary layer is unaltered by the boundary layer velocity gradient or the streamwise acceleration. Further, as indicated in Ames, Kwon, and Moffat [25] this $Tu * Lu^{-1/3}$ dependency implies that the relatively larger turbulent eddies in the v' spectrum are blocked by the presence

of the wall leaving only the smaller eddies to penetrate into the thin pressure surface boundary layer and augment mixing. Ames [8] studied heat transfer on a vane pressure surface at chord Reynolds numbers of 800,000 and 500,000. He concluded that the data supported a Reynolds number dependence of a 1/3rd power for laminar heat transfer augmentation of the pressure surface boundary layer. He suggested that this dependence was also supported by a simple asymptotic analysis of a laminar boundary after Ames and Moffat [4]. The present data represent an opportunity to test this physical model across a much wider (4 to 1) range in Reynolds numbers. Figure 15 presents augmentation levels $(St-St_0)/St_0$ on the pressure surface versus the heat transfer dependence parameter, $Tu\ (C/Lu)^{1/3}\ Re_C^{1/3}$ for average augmentation levels at –0.162 m and –0.199 m. A best-fit line through the data is shown along with plus and minus 5% error bands with very good results. These data provide support of the above augmentation dependence.

Stagnation Region Augmentation. At lower chord Reynolds numbers heat transfer levels in the stagnation region of a vane or blade are often higher than any other location as shown in figures 9 and 10. Consequently, predicting heat transfer accurately in this region is critical to designing cooling methods, which are reliable and efficient. Heat transfer through the laminar boundary layer in a stagnation region is different than on a pressure surface due to the rate of strain, which is present there. Hunt [11] first predicted the response of small and large scale turbulent eddies to the straining, which occurs in the stagnation region of a cylinder using rapid distortion theory. He concluded that the relatively small scale eddies are amplified as they are stretched around the stagnation region of a cylinder by the approaching flow and the large scale eddies are largely blocked by the cylinders presence. Britter, Hunt, and Mumford [12] later experimentally verified this conclusion. Ames and Moffat [4] used the results of Hunt to develop a simple model spectrum for turbulence approaching a cylinder stagnation point. They used the spectrum model in a simple asymptotic analysis to develop a correlating parameter for stagnation region heat transfer, which included the effect of scale. Based on this analysis heat transfer augmentation $[(Nu-Nu_0)/Nu_0]$ in a stagnation region is expected to increase as a function of turbulence intensity, Reynolds number to the 5/12th power, and diameter to energy scale to the 1/3rd power. That is $(Nu-Nu_0)/Nu_0 \propto Tu\ Re_D^{5/12}\ (D/Lu)^{1/3}$. The different Reynolds number dependence compared to the pressure surface is due to the amplification of the turbulence from the straining effect. Since the present data represents a relatively wide range of turbulence levels and Reynolds numbers, it provides a good test to this correlation. Ames [8] suggests a good engineering approximation for this correlation is $(Nu-Nu_0)/Nu_0 = 0.04\ Tu\ Re_D^{5/12}\ (D/Lu)^{1/3}$. Figure 16 presents stagnation region heat transfer augmentation data in terms of $(Nu-Nu_0)/Nu_0$ versus the $Tu\ Re_D^{5/12}\ (D/Lu)^{1/3}$ for the two data points on either side of the predicted stagnation point (-0.01 m and +0.0088 m). The solid line represents the above correlation, while data for the three Reynolds numbers are presented for each of the five higher turbulence conditions. The data are well correlated by this turbulence parameter and all data fall within +/- 7.4 percent of the line. Considering the collective uncertainty of the turbulence parameter is +/- 5 percent and the repeatability of the heat transfer data is +/- 3 percent, the correlation fits the data with very good accuracy.

Finite Difference Boundary Layer Predictions. These data provide an excellent test for vane heat transfer predictive capabilities due to the range of turbulence conditions and Reynolds numbers present as well as the relevant fully loaded vane design. Two-dimensional finite difference boundary layer predictions were made for this complete data set using the algebraic turbulence model [ATM] of Ames, Kwon, and Moffat [25], the transition model of Mayle [15], and STAN7 [21], a finite difference boundary layer code. The ATM is a simple spectral model of v' turbulence accounting for the attenuation of large eddies in the proximity of the wall due to the wall's blocking effect. It was originally developed to predict the augmentation to a turbulent boundary layer (Ames and Moffat [4]) and was shown to produce the correct near wall eddy viscosity distributions in a laminar boundary layer developing on the pressure surface of a vane by Ames, Kwon, and Moffat [25]. The basic model is given below:

$$\nu_{M,o} = 1.5\ C_\mu\ Tu_\infty\ U_\infty\ Lu_\infty\ [1 - \exp(-2.9\ Y/Lu_\infty)]^{4/3}\ D_\nu \qquad (3)$$

The near wall damping function, D_ν, accounts for the effect of viscous action on the turbulent spectrum and is presented below:

$$D_\nu = (1 - \exp(-y/[\eta C_\eta])) \qquad (4)$$

η is the Kolmogorov length scale and C_η is a constant set equal to 6.7. Note that the constant, C_η was erroneously given in the numerator rather than the denominator of the exponential in Ames, Kwon, and Moffat [25]. STAN7 uses the inlet approach velocity, turbulence level, and energy scale for the inlet turbulence boundary conditions and predicts the decay of turbulence using the freestream turbulent kinetic energy equation. For these heat transfer predictions, the turbulent Prandtl number is taken as 0.85. This value is an estimate and data are needed to determine the actual turbulent Prandtl number across an accelerating laminar boundary layer subjected to high levels of flow field turbulence.

Heat transfer predictions are shown for the three Reynolds numbers in figures 17, 18, and 19. Largely, the level of augmentation predicted by the ATM matches the experimental augmentation on the laminar region of the pressure surface well. On the pressure surface for the lower Reynolds number shown in figure 17, the data are as much as 12 percent below the predictions midway along the pressure surface but improve toward the trailing edge. This represents the largest discrepancy found in the laminar region of the pressure surface for all data sets. On the suction surface near the stagnation region, the calculations underpredict the level of augmentation because the ATM does not account for the action the rapid strain has on the turbulence in the stagnation region. This underprediction for the stagnation region is consistent across all three Reynolds numbers. The pressure surface data of figures 18 and 19 for chord exit Reynolds numbers of one and two million show the start of transition. For the one million Reynolds number, Mayle's [15] transition model begins to predict transition when the acceleration parameter, K, drops below 3E-6 on the pressure surface at a surface arc of –0.35 m. Augmentation data in figure 13 suggest that this location is appropriate for the grid, aero-combustor with spool, and aero-combustor. However, the data for the DLN combustor indicate that transition may start before –0.3 meters. For the highest Reynolds number the acceleration constraint allows transition to proceed after a surface arc of –0.25 m. However, the DLN combustor data indicate transition starts at around –0.2 m. In spite of slight discrepancies in the location of transition, Mayle's transition model performs very well on the pressure surface for these data.

The transition model is shown to predict transition early on the suction surface for all Reynolds numbers at the higher levels of turbulence. For the lowest Reynolds number case, figure 17, transition

is predicted to proceed after the adverse pressure gradient on the suction surface begins. However, after a favorable pressure gradient commences, the spot production rate model drops rapidly producing the wiggle in the prediction.

Stagnation Region Prediction. The ATM given in equation (3) underpredicts the stagnation region heat transfer data as shown in figures 17 through 19. However, stagnation region heat transfer correlates well on the TRL parameter of Ames and Moffat [4] as shown in figure 16. This suggests that the ATM model could be improved if we could account for the effect of the rapid strain in the stagnation region of an airfoil by predicting this turbulence amplification similar to the TRL correlation. Hunt [11] used rapid distortion theory to account for the amplification of small-scale turbulence in the presence of a cylindrical stagnation region. The spectrum function in the inertial subrange can be related to the dissipation rate. By applying Hunt's results to the edge of the stagnation region boundary layer, the increase in the dissipation rate can be correlated by the stagnation region's diameter Reynolds number.

$$\varepsilon/\varepsilon_0 = (Re_D/4)^{1/4} \quad (5)$$

The stagnation region diameter Reynolds number can be estimated using the local streamwise velocity gradient at the stagnation region.

$$Re_D \cong \rho_\infty U_\infty^2 \, 3.62/(dU_\infty(X=0)/dx)/\mu_\infty \quad (6)$$

The change in the dissipation can be related to an increase in the near wall eddy viscosity through the length scale term, Lu_∞ in equation (3). This turbulence amplification is observed to be present around the stagnation region where high strain rates occur but is not noticeably present on the pressure surface as shown by the Reynolds number dependence in the present data as well as by the eddy diffusivity data of Ames, Kwon, and Moffat [25]. Other turbulence models have previously been tied to the local strain rates. For example, Forest [26] used the Pohlhausen parameter to correlate a constant in his eddy viscosity model. In the calculations shown in figure 20 the following function was used "turn on" and "turn off" the amplification of turbulence:

$$f_{amp} = [1 - \exp\{-2.5\,[(dU_\infty(X)/dx)/(dU_\infty(X=0)/dx)]^2\} \quad (7)$$

The increase in eddy viscosity can be estimated as shown below:

$$\nu_M/\nu_{M,o} = 1 + [(Re_D/4)^{1/12} - 1] * f_{amp} \quad (8)$$

This function works well in the stagnation region, where the function f_{amp} is close to 1.0. The accuracy of these predictions in the stagnation region support the appropriateness of the Ames and Moffat [4] stagnation region turbulence model. The function also works well over the pressure surface where the f_{amp} is close to zero. However, the accuracy of the function in estimating the amplification of turbulence as the acceleration changes from the high levels found in the stagnation region to more moderate levels found on the pressure surface has not been determined.

SUMMARY AND CONCLUSIONS

The present vane heat transfer data document the influence of mock DLN and catalytic combustion systems on a conventionally loaded vane over a four to one range in Reynolds numbers. These data should help reduce the risk of integrating these new technology combustors into industrial gas turbine systems. Additionally, heat transfer data have been acquired for low turbulence, grid turbulence, and two levels of aero-derivative combustor turbulence over the same Reynolds number range. These data offer turbine designers heat transfer comparisons between known and new inlet configurations providing information on the likely response of turbine heat transfer to these new systems.

These data provide quantitative information on turbulence characteristics developed in DLN and catalytic combustion systems, which previously have had little documentation in the open literature. Additionally, these data suggest that in clean environments laminar flow is predominately present on first vanes in small to medium sized gas turbine systems with catalytic combustion systems. This knowledge has significant potential for simplifying first vane designs for gas turbine systems with catalytic combustion.

These data help demonstrate the impact of flow field straining on the turbulence in the stagnation region of a vane and the corresponding impact on heat transfer. The resulting difference in the effect of Reynolds number scaling was shown for the pressure surface and the stagnation region. Further, a simple method to account for this leading edge effect has been added to the ATM of Ames, Moffat, and Kwon [25] based on eddy diffusivity scaling ideas developed by Ames and Moffat [4].

Comparative predictions have been made using the STAN7 [21] finite difference boundary layer code with the ATM model of Ames, Moffat, and Kwon [25] and the Mayle [15] transition model. Results showing laminar augmentation in the stagnation region and pressure surface were very good. The location and length of transition were captured well on the pressure surface but appeared slightly conservative on the suction surface. These present midline heat transfer data are expected to provide a useful database for the grounding of vane heat transfer predictive methods.

ACKNOWLEDGEMENTS

The authors would like to gratefully acknowledge support for this work from the Advanced Gas Turbine System Research program, which is funded by a consortium including the Department of Energy and participating industrial members. Additionally, this project was initially funded through a seed grant from the North Dakota EPSCoR program, the University of North Dakota, and the Mechanical Engineering Laboratory endowment fund. The authors would like to acknowledge the turbine aero group at Rolls Royce of Indianapolis for developing a special incompressible vane design in a conventionally loaded configuration for this project. Additionally, the authors would like to thank UND student's Dan Pelarski, Troy Lassle, and Mark Hettwer as well as the senior design team, which helped with this project.

REFERENCES

1. Dils, R. R., and Follansbee, P. S., 1977, "Heat transfer coefficients around cylinders in crossflow in combustor exhaust gases," J. Engr. Power, Vol. 99, pp. 497.
2. Zimmerman, D. R., 1979, "Laser anemometer measurements at the exit of a T63-C20 combustor," NASA CR-159623.
3. Bicen, A. F., and Jones, W.P., 1986, "Velocity characteristics of isothermal and combusting flows in a model combustor," Combust. Sci. and Tech., Vol. 49, pp. 1.
4. Ames, F.E., and Moffat, R.J., 1990, "Heat Transfer with High Intensity, Large Scale Turbulence: The Flat Plate Turbulent

Boundary Layer and the Cylindrical Stagnation Point," Report No. HMT-44, Thermosciences Division of Mechanical Engineering, Stanford University.
5. Moss, R.W., and Oldfield, M.L.G., 1991, "Measurements of Hot Combustor Turbulence Spectra," ASME Paper No. 91-GT-351.
6. Goebel, S. B., Abuaf, W., Lovette, T. A., and Lee, C.-P., "Measurement of Combustor Velocity and Turbulence Profiles," ASME Paper 93-GT-228.
7. Zhang, L.J., and Gleazer, B., 1995, "Indirect turbulence measurement in gas turbine stages using heat flux probe," ASME Paper No. 95-GT-153.
8. Ames, F.E., 1997, "The Influence of Large-Scale High-Intensity Turbulence on Vane Heat Transfer," Journal of Turbomachinery, Vol. 199, pp. 23-30.
9. Van Fossen, G. J., Bunker, R. S., "Augmentation of stagnation heat transfer due to turbulence from a DLN can combustor," ASME Paper No. 2000-GT-215.
10. Van Fossen, G.J., Simoneau, R.J., and Ching, C.Y., 1995, "The influence of turbulence parameters, Reynolds number, and body shape on stagnation region heat transfer," ASME Journal of Heat Transfer, Vol. 117. pp. 597-603.
11. Hunt, J.C.R., 1973, "A Theory of Turbulent Flow Round Two-Dimensional Bluff Bodies," J. Fluid Mech., Vol. 61, Part 4, p. 625.
12. Britter, R. E., Hunt, J.C.R., and Mumford, J.C., 1979, "The distortion of turbulence by a circular cylinder," Journal of Fluid Mechanics, Vol. 92.
13. Arts, T., Lambert de Rouvroit, M., and Rutherford, A.W., 1990, "Aero-thermal Investigation of a Highly Loaded Transonic Linear Turbine Guide Vane Cascade," Technical Note 174, von Karman Institute for Fluid dynamics, Belgium.
14. Wang, H. P., Goldstein, R. J., and Olson, S. J., 'Effect of free-stream turbulence with large length scale on blade heat/mass transfer," Journal of Turbomachinery, Vol. 121, pp. 217-224.
15. Mayle, R.E., 1991, "The Role of Laminar-Turbulent Transition in Gas Turbine Engines," ASME Journal of Turbomachinery, Vol. 113, pp. 509-537.
16. Zhang, L, and Han, J.-C., 1994, "Influence of mainstream turbulence on heat transfer coefficients from a gas turbine blade," ASME Journal of Heat Transfer, Vol. 116, pp. 896-903.
17. Boyle, R.J., and Simon, F.F., 1999, "Mach number effects on turbine blade transition length prediction," ASME Journal of Turbomachinery, Vol. 121. pp. 694-701.
18. Thole, K.A. and Bogard, D.G. 1995, "Enhanced Heat Transfer and Skin Friction due to High Freestream Turbulence," ASME Journal of Turbomachinery, Vol. 117, pp. 418.
19. FLUENT 5.3, 1999, FLUENT 5.3 User's Guide, Fluent, Inc., Lebanon, N.H.
20. Smith, D., 2000, "Private communication," Rolls-Royce, Indianapolis.
21. Kays, W.M., 1987, "STAN7, a finite difference boundary layer code."
22. Moffat, R.J., 1988, "Describing the uncertainties in experimental results," Experimental Thermal and Fluid Science, Vol. 1., pp. 3-17.
23. Hancock, P.E., and Bradshaw, P., 1983, "The effect of free stream turbulence on turbulent boundary layers," J. Fluids Engr., Vol. 105, pp. 284.
24. Hinze, J., 1975, Turbulence, 2nd ed. McGraw-Hill, New York.
25. Ames, F.E., Kwon, K, and Moffat, R.J., 1999, "An algebraic model for high intensity large scale turbulence," ASME Paper No. 99-GT-160.
26. Forest, A.E., 1977, "Engineering Predictions of Transitional Boundary Layers," AGARD-CP-224.

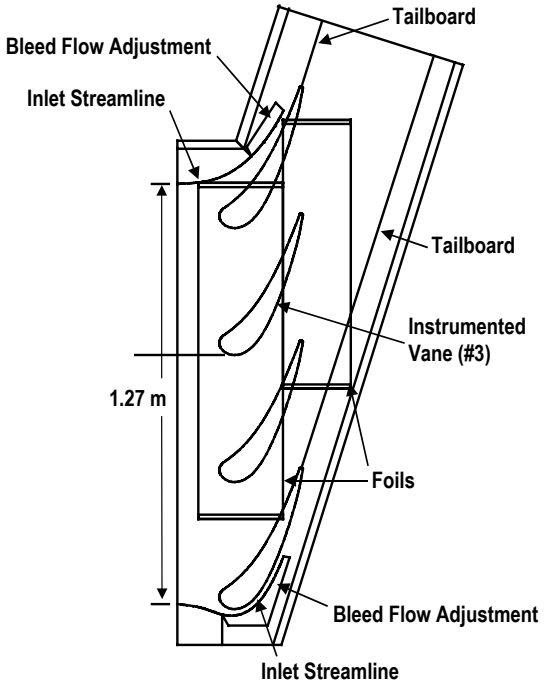

Figure 1. Schematic of cascade test section for large-scale low speed wind tunnel.

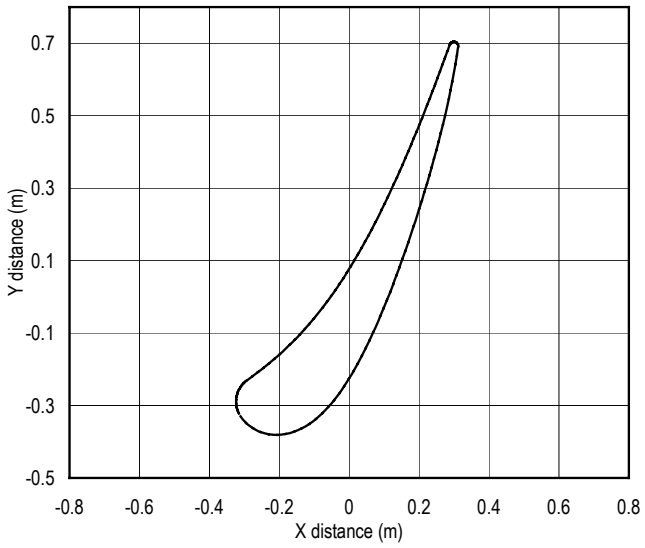

Figure 2. Cross-sectional view of large scale conventionally loaded vane used in this study.

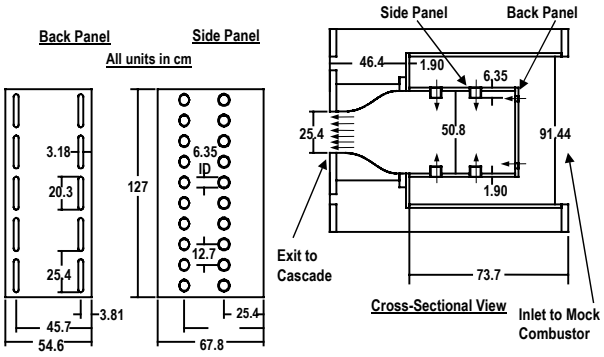

Figure 3. Schematic of mock aeroderivative combustor turbulence generator

Figure 4. Digital photo of dry low NOx swirlers installed in mock combustor liner

Figure 5. Digital photo of catalytic combustor surface installed in mock combustor liner

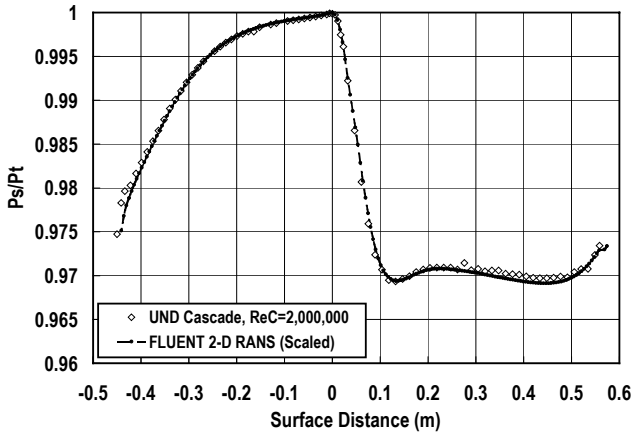

Figure 6. Comparison between measured and predicted vane midspan pressure distribution

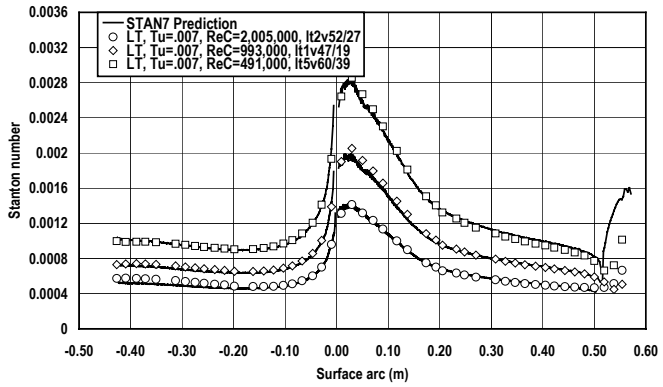

Figure 7. Low turbulence vane Stanton number distributions with STAN7 predictions

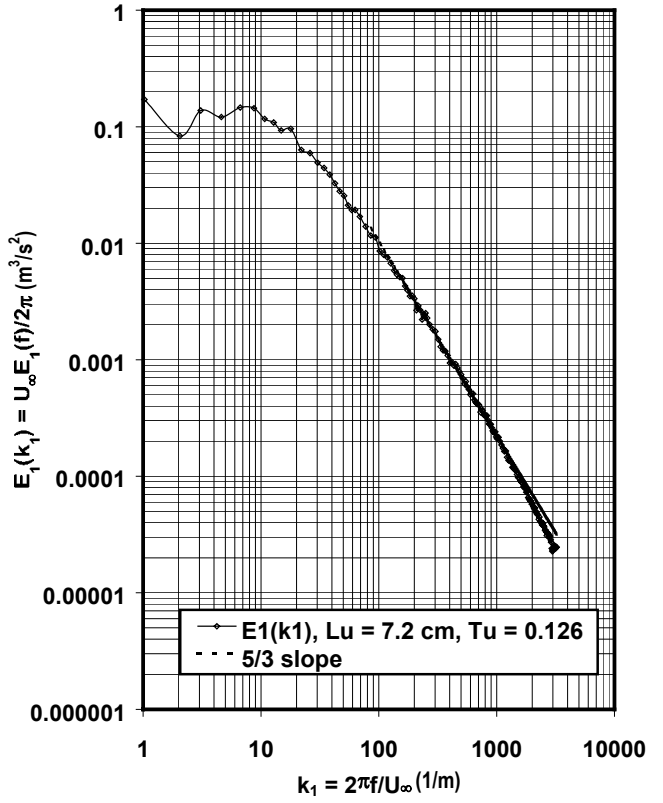

Figure 8. One-dimensional spectra of u' for aero-derivative combustor

	Reynolds	Tu	U (m/s)	Lx (cm)	Lu (cm)	ε (m²/s³)
low turbulence [LT]	500,000	0.0069	4.96	8.12	127.0	0.00005
	1,000,000	0.0076	10.43	5.02	154.5	0.00035
	2,000,000	0.0060	18.71	3.58	15.5	0.0144
aeroderivative combustor [AC]	500,000	0.1313	5.24	3.68	7.24	6.67
	1,000,000	0.1402	9.32	3.52	6.36	51.5
	2,000,000	0.1339	18.39	3.58	7.35	302.0
grid [Grid]	500,000	0.0821	4.77	2.00	3.27	2.70
	1,000,000	0.0861	10.19	2.04	3.35	29.8
	2,000,000	0.0884	19.27	2.35	3.53	206.8
catalytic combustor [CC]	500,000	0.0103	4.95	5.26	3.83	0.0052
	1,000,000	0.0153	9.46	0.62	5.15	0.093
	2,000,000	0.0102	19.63	0.89	1.75	0.680
combustor with spool [ACS]	500,000	0.0915	5.11	5.08	9.03	1.67
	1,000,000	0.0950	9.74	4.61	8.81	13.23
	2,000,000	0.0928	18.19	4.44	9.49	75.17
dry low NOx [DLN]	500,000	0.1342	5.17	4.57	8.78	5.60
	1,000,000	0.1433	9.65	4.34	8.95	43.73
	2,000,000	0.1417	19.11	4.47	10.77	274.5

Table 1. Characteristics of inlet velocities, turbulence level and scale, and dissipation for various turbulence generators

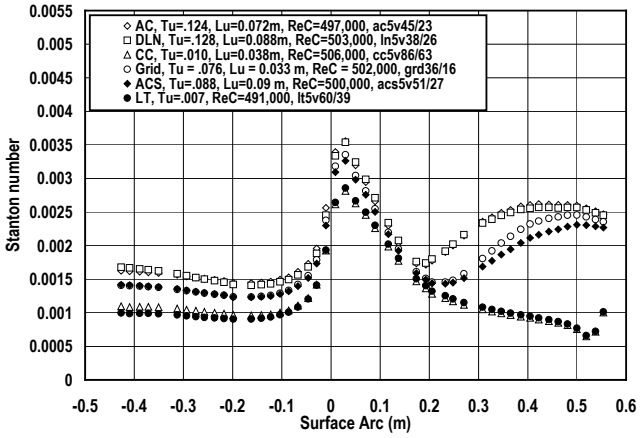

Figure 9. Effects of mock combustor turbulence characteristics on vane Stanton number distributions, Re_C = 500,000

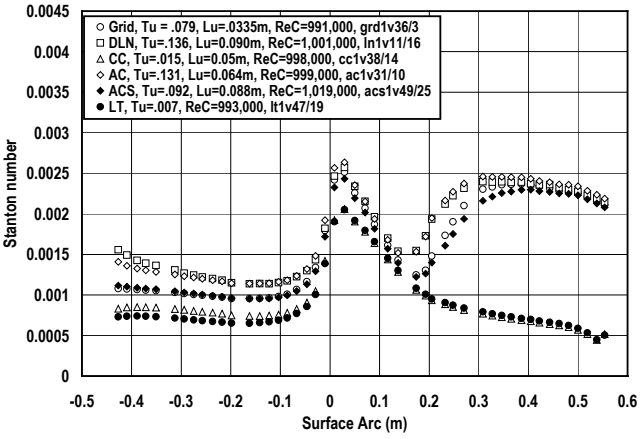

Figure 10. Effects of mock combustor turbulence characteristics on vane Stanton number distributions, Re_C = 1,000,000

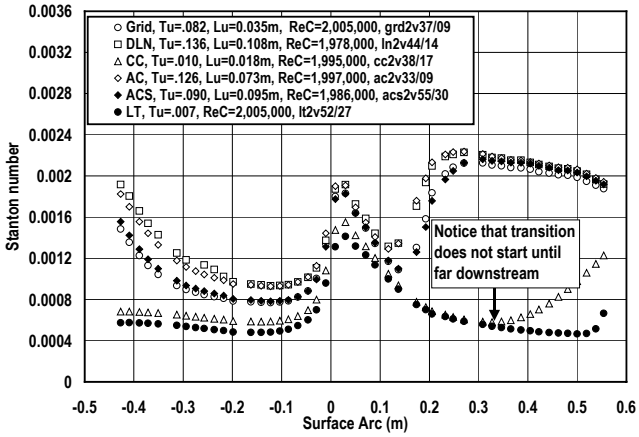

Figure 11. Effects of mock combustor turbulence characteristics on vane Stanton number distributions, Re_C = 2,000,000

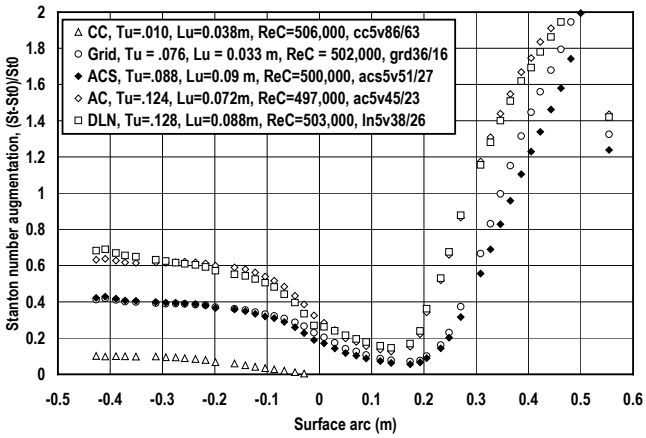

Figure 12. Effects of mock combustor turbulence characteristics on Stanton number augmentation and location of transition, Re_C = 500,000

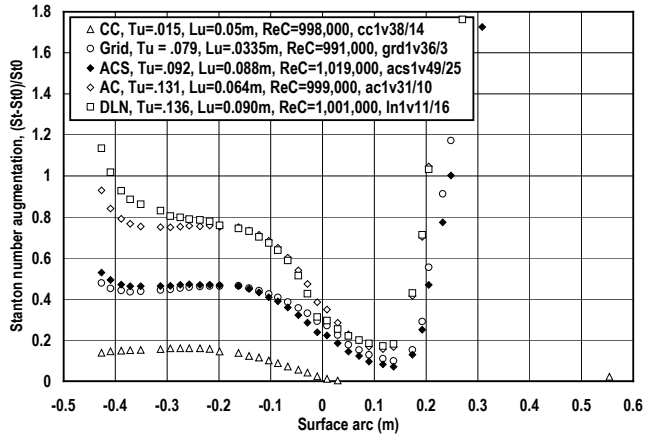

Figure 13. Effects of mock combustor turbulence characteristics on Stanton number augmentation and location of transition, Re_C = 1,000,000

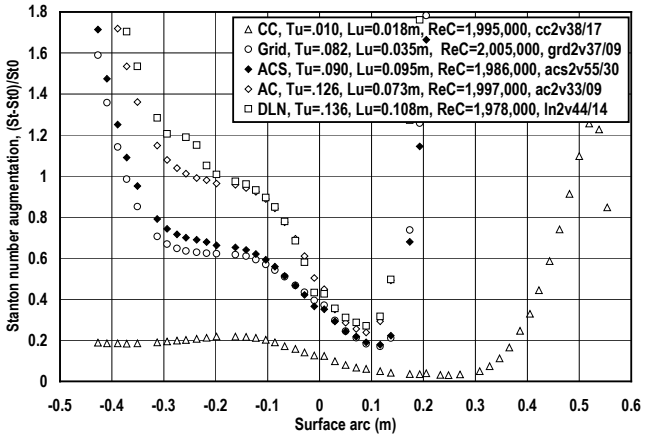

Figure 14. Effects of mock combustor turbulence characteristics on Stanton number augmentation and location of transition, Re_C = 2,000,000

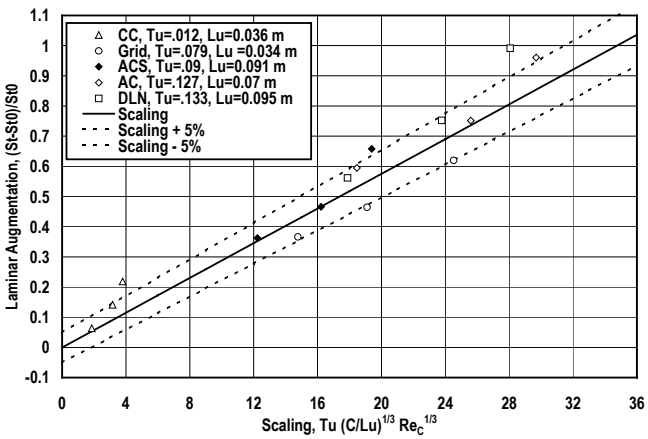

Figure 15. Correlation of pressure surface Stanton number augmentation with turbulence intensity, energy scale, and chord Reynolds number.

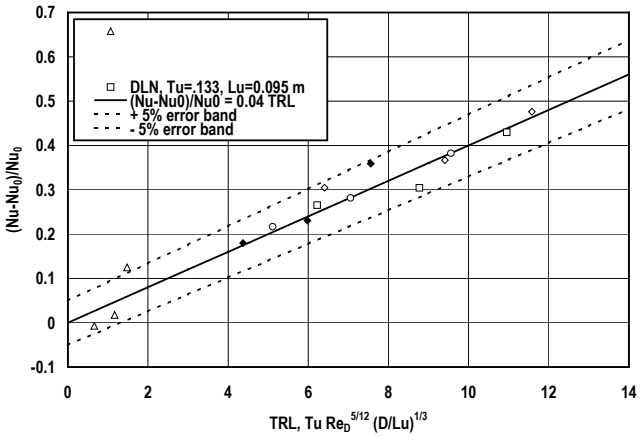

Figure 16. Correlation of stagnation region Nusselt number augmentation with TRL parameter

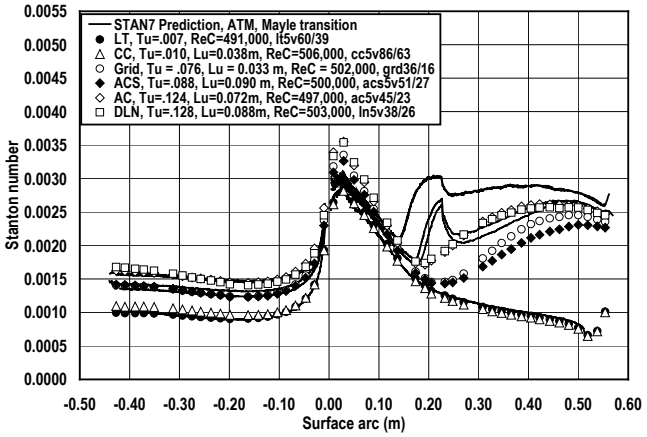

Figure 17. Prediction of turbulence effects on vane Stanton number distributions using STAN7 with ATM and Mayle (1991), Re_C = 500,000

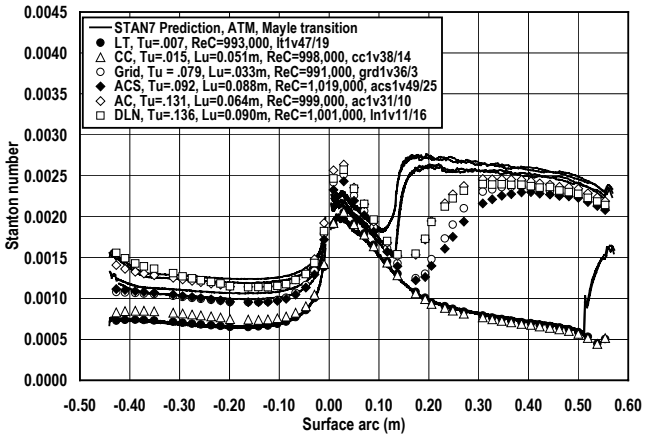

Figure 18. Prediction of turbulence effects on vane Stanton number distributions using STAN7 with ATM and Mayle (1991), Re_C = 1,000,000

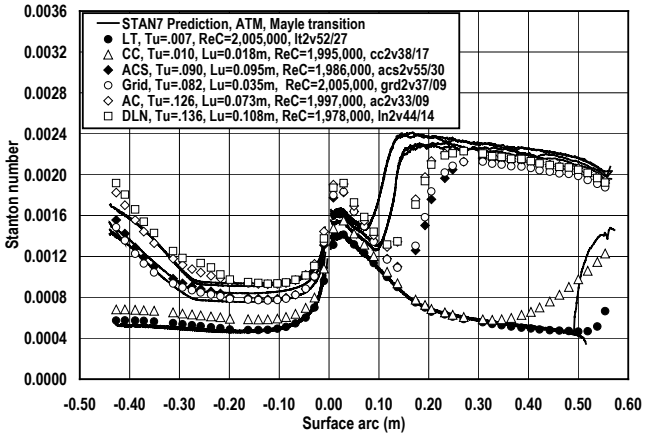

Figure 19. Prediction of turbulence effects on vane Stanton number distributions using STAN7 with ATM and Mayle (1991), Re_C = 2,000,000

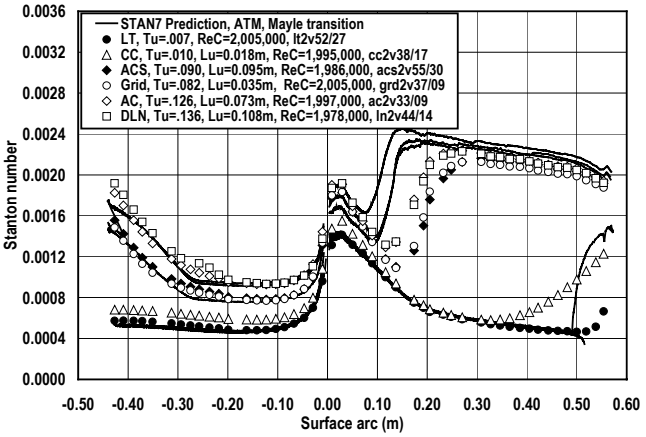

Figure 20. Prediction of turbulence effects on vane Stanton number distributions with stagnation region model, Re_C = 2,000,000

Proceedings of
ASME TURBO EXPO 2002
June 3-6, 2002, Amsterdam, The Netherlands

GT-2002-30525

EFFECTS OF AERODERIVATIVE COMBUSTOR TURBULENCE ON ENDWALL HEAT TRANSFER DISTRIBUTIONS ACQUIRED IN A LINEAR VANE CASCADE

Forrest E. Ames, Pierre A. Barbot, and Chao Wang
University of North Dakota
Mechanical Engineering Department
Grand Forks, ND, USA

ABSTRACT

Vane endwall heat transfer distributions are documented for a mock aeroderivative combustion system and for a low turbulence condition in a large-scale low speed linear cascade facility. Inlet turbulence levels range from below 0.7 percent for the low turbulence condition to 14 percent for the mock combustor system. Stanton number contours are presented at both turbulence conditions for Reynolds numbers based on true chord length and exit conditions ranging from 500,000 to 2,000,000. Low turbulence endwall heat transfer shows the influence of the complex three-dimensional flow field, while the effects of individual vortex systems are less evident for the high turbulence cases. Turbulent scale has been documented for the high turbulence case. Inlet boundary layers are relatively thin for the low turbulence case while inlet flow approximates a nonequilibrium or high turbulence channel flow for the mock combustor case. Inlet boundary layer parameters are presented across the inlet passage for the three Reynolds numbers and both the low turbulence and mock combustor inlet cases. Both midspan and 95 percent span pressure contours are included. This research provides a well-documented database taken across a range of Reynolds numbers and turbulence conditions for assessment of endwall heat transfer predictive capabilities.

NOMENCLATURE

C	vane true chord length, m
Cf/2	skin friction coefficient, $Cf/2 = \tau_w/\rho U_\infty^2$
Cp	specific heat at constant pressure, J/kg K
h	heat transfer coefficient, $W/m^2/K$, based on T_{green} and T_∞
H	Shape factor, $H = \delta_1/\delta_2$
Lu	energy scale, $Lu = 1.5\ |u'|^3/\varepsilon$
Lx	longitudinal integral scale of u' fluctuation
P	Pressure, Pa
q"	surface heat flux
Re_C	Reynolds number based on true chord and exit conditions
$Re_{\delta 2}$	momentum thickness Reynolds number, $Re_{\delta 2} = U_\infty \delta_2/\nu$
St	Stanton number, $St = h/(\rho Cp U_{exit,\infty})$
T	temperature, K
Tu	turbulence level, $Tu = \|u'\|/U_\infty$
U_∞	freestream velocity, m/s
U+	velocity nondimensionalized on inner variables, $U+ = U(y)/[U_\infty \bullet (Cf/2)^{1/2}]$
u', |u'|	streamwise component rms fluctuation velocity, m/s
Y	normal distance from test surface, m
Y+	wall normal distance nondimensionalized on inner variables, $Y+ = y \bullet [U_\infty \bullet (Cf/2)^{1/2}]/\nu$

Greek Letter Symbols

δ_1	displacement thickness, Eqn. (6.5) Kays and Crawford [1]
δ_2	momentum thickness, Eqn. (6.6) Kays and Crawford [1]
ε	emissivity
ε	turbulent dissipation rate, m^2/s^3
ν	kinematic viscosity, m^2/s
ρ	fluid density, mass per unit of volume, kg/m^3
σ	Stefan-Boltzman's constant
τ	shear stress, N/m^2

Subscripts

exit	refers to conditions at the nozzle exit plane
green	refers to peak in green intensity condition
rad	refers to radiative mode of heat transfer
s	refers to static condition
t	refers to total or stagnation condition
∞	evaluated in the free stream

INTRODUCTION

New low emission combustion systems are designed to have limited peak temperatures using lean combustion mixtures to produce low levels of NOx. A consequence of these lower peak temperatures is flatter temperature profiles leaving the combustion system. Another consequence of low NOx strategies is that any cooling air added after the combustion system reduces average rotor inlet temperature and the

resulting performance of the engine. Older systems often burned fuel/air mixtures at higher equivalence ratios for better operability ranges producing higher peak temperatures. Endwall surfaces were often insulated from higher peak gas temperatures by supplying plentiful supplies of colder air near these surfaces. Consequently, new combustion strategies have the effect of reducing midspan heat loads to vanes and significantly increasing endwall heat loads. Cooling engineers no longer have the option of adding more cooling air and compensating by increasing the combustion temperature. Designers must provide reliable component cooling using a minimum amount of air. As a result, they need better tools to predict endwall heat transfer.

The present research has been designed to develop of comprehensive database of endwall heat transfer measurements across a range of relevant turbulence conditions. This current paper presents results taken at a low level of turbulence and at a high level of turbulence generated with a mock aeroderivative combustor. These heat transfer measurements have been taken at true chord exit Reynolds numbers ranging from 500,000 to 2,000,000 and inlet turbulence characteristics and inlet boundary layer integral parameters have been comprehensively documented for all cases. Rolls Royce of Indianapolis is currently conducting an analytical effort with a goal of grounding and improving predictive methods for endwall heat transfer using the results of the current experimental study.

BACKGROUND

Secondary Flows. Sieverding [2] presented a noteworthy review of secondary flows in turbine blade passages collecting information from various sources and presenting models of secondary flows from Klein [3] and Langston [4]. Sieverding gives Klein credit for first recognizing the complex secondary flows developing on the endwall of a blade row. He indicates that the importance of work on secondary flows became evident as heat transfer and aerodynamic loss investigations began to show the impact of these secondary flows on heat transfer rates and secondary losses. Langston's model denotes the main vortex systems including the suction and pressure side leg of the horseshoe vortex as well as the passage vortex. Additionally, Langston indicates the existence of corner vortices in the stagnation region and along the pressure and suction surfaces of the blade. Marchal and Sieverding [5] suggest that secondary losses grow more rapidly in the region of the flow downstream from the maximum velocity. Unpublished work by Ames, Hylton, and York [6] at Allison Gas Turbine Division of General Motors showed that secondary losses increased with increasing thickness of the endwall inlet boundary layer and the position of the passage vortex core rose above the endwall in the exit region of the vane cascade. Recent vane cascade investigations show that leading edge fillets (Zess and Thole [7]) and inlet endwall contouring (Burd and Simon [8]) can reduce the impact of secondary flows.

Endwall Heat Transfer. Experimental studies on vane endwall heat transfer include studies by York et al. [9], Harasgama and Wedlake [10], Spencer et al. [11], Arts and Heider [12], and Radomsky and Thole [13]. Experimental studies on blade endwall heat transfer include studies by Goldstein and Spores [14] and Giel et al. [15]. Generally, similar results are achieved showing increased heat transfer in the stagnation region of the airfoil and downstream of or adjacent to the pressure surface of the airfoil. Location of the hotspot off the pressure surface seems to depend on cascade geometry, Reynolds number, and Mach number. Harasgama and Wedlake conducted heat transfer tests in a compressible annular cascade and found that heat transfer in the hub differed somewhat from heat transfer in the tip region. Spencer et al. added the influence of high turbulence with similar results. Radomsky and Thole compared the influence of high to low turbulence on endwall heat transfer in an incompressible linear cascade. They found the largest augmentation (~ 40%) in the low velocity inlet regions and a reduced level of augmentation (~ 10%) in the higher velocity regions. CFD computations can at times produce reasonable predictions of endwall heat transfer cases but can also produce inaccurate results. Boyle and Lucci [16] found that endwall heat transfer predictions are dependent on the turbulence model and agreement between predictions and experiment can vary from case to case for a given model. This suggests that endwall heat transfer data taken over a relevant range of parameters is needed to adequately test the relevancy of turbulence models for endwall heat transfer and secondary flow prediction.

EXPERIMENTAL APPROACH

This heat transfer research has been conducted in the University of North Dakota's large-scale low speed cascade facility. This facility is configured in a steady state blow down arrangement and is documented to a further extent in GT-2002-30524. The wind tunnel is powered by a 45 kW blower capable of providing 6.6 m^3/s of air at a static pressure rise of 5000 Pa. The blower outlet flow is directed through a two stage multivane diffuser section to distribute and diffuse the flow prior to entering a heat exchanger. The heat exchanger system, which uses a cooling water recirculation system, helps to provide a steady and controllable inlet air temperature. The flow is further conditioned downstream of the heat exchanger in a four section screen box. The low turbulence baseline configuration uses a 3.6:1 area ratio two-dimensional nozzle to further accelerate the air prior to entrance into the linear vane cascade test section.

The cascade test section used in this study is shown schematically in figure 1. The cascade is based on an eleven times scale mid span vane profile representative of a modern mid-sized industrial gas turbine. The vane profile was designed for incompressible flow and has a velocity distribution, which is consistent with current conventionally or fully loaded vanes in industrial engines. The test section is designed to produce accurate two-dimensional aerodynamics at the midspan of the cascade using a four-vane three-passage configuration. The cascade has inlet bleeds and exit tailboards to allow inlet flow uniformity and exit flow periodicity. The inlet bleed flows were designed along two-dimensional streamlines predicted by FLUENT [17] and the flexible exit tailboards can be shaped to account for streamline curvature. The cascade has a row of inlet static taps one-quarter axial chord upstream from the vane leading edge and a row of exit taps one-quarter axial chord downstream to monitor the cascade setup. Ten probe access ports are provided along the row of inlet static pressure taps to measure inlet temperature and total pressure and to survey inlet turbulence characteristics.

The vane has a true chord of 47.8 cm and an axial chord of 25.0 cm. The vanes have a 38.4 cm spacing and a height of 25.4 cm. The diameter of the leading edge is 5.59 cm and the diameter of the trailing edge is 0.98 cm. The stagger angle of the vane is 55.1 degrees and the calculated air exit angle is 73.4 degrees. The span to chord length aspect ratio of the present cascade geometry is 0.53, comparing reasonably well with the 0.68 aspect ratio of the engine vane geometry.

This study investigated endwall heat transfer at exit Reynolds numbers based on true chord length of 500,000, 1,000,000, and 2,000,000. This range of first vane chord exit Reynolds numbers is

consistent with a range of small to medium industrial or propulsion gas turbine engines.

Turbulence Generator. This study was designed to investigate turbulence characteristics representative of modern combustion systems and their influence on endwall heat transfer. A mock aeroderivative combustion system was developed to provide turbulence with characteristics, which are representative of many current engines and have been documented in the literature. The mock combustor configuration is shown schematically in figure 2. Looking at the cross-sectional view, flow enters from the right and is forced through the slots in the back panel and the two rows of holes in the side panels simulating a recirculation zone and a dilution zone. The flow then leaves the mock combustor through the 2 to 1 area ratio contraction nozzle on the left of the cross-sectional view and immediately enters the cascade. This mock combustor replaces the 3.6:1 area ratio nozzle for the high turbulence test case.

Vane Pressure Distribution. Heat transfer and pressure distributions were acquired on the third vane from the bottom. This "instrumented" vane can be inserted through a machined hole in the acrylic endwall where it is held in place using a flange. The pressure vane was cast from epoxy over a structure of 82 pressure tubes incrementally spaced along and adjacent to its surface. Static pressure taps were fabricated by drilling through the epoxy surface into the brass tube with a 0.8 mm diameter drill bit. The baseline pressure distribution for the low turbulence case is shown in figure 3 where it is compared to a 2-D prediction using FLUENT. On this figure negative surface distance is taken from the calculated stagnation point (0 cm) along the pressure surface toward the trailing edge and positive surface distance is determined along the suction surface. The viscous prediction calculates the data with precision. Overall, the comparison is excellent and gives confidence in the quality of the mid span aerodynamics produced by the cascade. Developing accurate aerodynamics is critical to producing a heat transfer database, which is valuable for understanding the impact of new combustion systems and for grounding predictive methods.

The 2-D FLUENT computations were made to support the design of the present facility and for comparison with the measured midline pressure distributions. The Spalart-Allmaras one-equation eddy viscosity transport model was selected since the model is computationally efficient and considered quite capable of producing accurate pressure distributions on the surface of a vane. For the computation, 220 grid points were placed along the surface of the vane with concentrations in the leading and trailing edges. A boundary layer mesh was applied to the vane to ensure an orthogonal grid was adjacent to the flow surface and to resolve the boundary layer into the laminar sublayer.

Endwall Heat Transfer Measurements. Endwall surface heat transfer measurements have been acquired using a constant heat flux boundary condition generated by a 0.001" Inconel foil and narrow band thermochromic liquid crystal thermometry. On the third vane from the bottom, a commercially fabricated foil was wrapped from the suction surface trailing edge around the leading edge to the pressure surface trailing edge to generate a constant surface heat flux. Two foils were applied to the endwall to develop a constant surface heat flux in that region. All three foils were incrementally heated at consistent heat flux levels to paint isotherms over the endwall at different Stanton number levels. Backup instrumentation for the vane heat transfer test was fabricated by casting fine wire thermocouples along the surface of an epoxy vane to determine the midline surface temperatures. These temperature measurements served to check the narrow band liquid crystal paint temperatures.

Application of narrow band microencapsulated thermochromic liquid crystal (TLC) paints have resulted in uncertainty bands for driving temperature difference of +/- 1 percent for a 25° C temperature difference (Hippensteele, Russell, and Torres, [18]; Hippensteele, Russell, and Torres, [19]; Hippensteele and Russell, [20]; Jones and Hippensteele, [21]. Camci et al. [22] report the ability to resolve surface temperature using narrow band liquid crystal paints to within +/- 0.1° C when using a single color such as green. Giel et al. [15] indicate microencapsulated liquid crystals are less sensitive to viewing and illumination angles. The liquid crystal paint selected for the present experiment has a 1° C bandwidth with a 37° C start. The microencapsulated liquid crystal paint was calibrated using an aluminum test surface, which was first heated then allowed to cool. Temperatures were recorded as a function of time during the cooling process while digital photos of the test surface were acquired periodically. The camera was set to a fully manual mode to allow the highest reproducibility of color and intensity. The results show a sensitivity of 229°/°C around 37° C. This sensitivity of hue angle to temperature for the highest green intensity is very high and accuracy of the 37° C color change was estimated to be within 0.2° C over the span of the tests.

A constant heat flux boundary condition was generated on one of the endwalls using a rectangular constant heat flux foil. The foil was adhered to a thin epoxy board, which in turn was secured to a one-inch layer of polyisocyanurate foam insulation. Under the footprint of the vane, an aluminum vane shaped heat exchanger was placed to conduct away the thermal energy generated in this region by the foil. In this way, both the endwall and the vane could be run at a constant heat flux that was matched. Many full surface vane and endwall heat transfer experiments do not have matched boundary conditions between at the vane and endwall interface. This condition produces an unheated starting length condition when flow approaches from an inactive surface.

The surface Stanton number data were acquired by first increasing the heat flux rate on all the plates until the first green color appeared on the surface. At that point, the surface heat flux was increased until the next incremental Stanton number was achieved based on exit conditions and surface to total temperature difference.

$$St = \frac{\left(q'' - q''_{rad}\right)}{\left(T_{green} - T_{T,IN}\right)\rho\, U_{\infty}\, Cp}$$

The radiative heat loss was estimated to be:

$$q''_{rad} = \varepsilon\, \sigma \left(T_{green}{}^{4} - T_{T,IN}{}^{4}\right)$$

The conduction loss was ignored because the radiative loss estimate was slightly over-estimated and the conduction loss was within the uncertainty band of that estimate. When the test surface had reached steady state, pictures were acquired using a digital camera in the manual mode for all endwall locations where color appeared. The heat flux rate of the foils surface was then adjusted to produce the next incremental iso-Stanton number. The procedure to change the heat flux, wait for steady state, and then acquire digital images was repeated until the last incremental iso-Stanton number was achieved. Uncertainties were highest for the lowest Stanton numbers at the

lowest Reynolds number where the overall uncertainty was estimated to be +/- 10 percent at 20 to 1 odds. At this condition the estimated radiative loss less the 1-D conduction loss was 21 percent of the net surface heat flux. At the highest Reynolds number the maximum uncertainty in Stanton number was estimated to be +/- 5 percent at 20 to 1 odds. The largest source of error was due to the uncertainty in the radiative loss.

Data Acquisition. Pressures were acquired using two Rosemount Smart Pressure Transmitters scaled to ranges of 250 and 5000 Pa full scale with 0.1 percent of scale accuracy. Voltage outputs for both the pressure transmitters and for the chromel-alumel thermocouples were scanned and read using an HP 3497A data acquisition system. The data acquisition unit has an integral voltmeter with 1 μV sensitivity. Thermocouples were all connected through a passive constant temperature junction and were referenced using an ice bath junction. Hot wires were powered, low pass filtered, bucked and gained using a two channel TSI ISA 300 hot wire anemometry bridge. Raw signals were read with a PC based high-speed data acquisition card with 12 bits of resolution. Mean velocities were acquired at a data acquisition rate equivalent to about three integral time scales. Velocity time records for spectral analysis were acquired in 40 sets of 8192 samples and post processed.

Data Uncertainties. Estimates for the uncertainty in heat transfer, pressure, velocity, and turbulence measurements were determined using the root sum square method described by Moffat [23]. Uncertainty in the local vane surface static pressure was estimated at a maximum of 2.5 percent. Exit velocity was determined at a precision of 2 percent. The uncertainty in turbulence level for the single wire was estimated to be 3 percent of the reported value. The experimental error in turbulent scale is estimated to be 11 percent. All uncertainty estimates are quoted for a 95 percent confidence interval.

Inlet Conditions and Turbulence Characteristics. Two turbulence conditions are reported in this endwall heat transfer paper. Heat transfer data, inlet velocity profiles, and turbulence measurements were taken for both turbulence conditions and all three Reynolds numbers. Span averaged turbulence data (Tu, Lx, Lu, and ε) are reported in the initial section of the tables while parameters for the inlet velocity profiles are reported for five circumferential positions in the remainder of the tables. These measurements were acquired 7 cm upstream from the leading edge plane of the vanes. Midspan or peak velocity (U_∞), integral thicknesses (δ_2 & δ_1), shape factor (H) skin friction coefficient (Cf/2), turbulence level (Tu), and momentum thickness Reynolds number ($Re_{\delta 2}$) were determined for each condition and are presented in Tables 1a and 1b.

EXPERIMENTAL RESULTS

The experimental results documented in this paper include comprehensive inlet boundary layer parameters and turbulence conditions, 95% span pressure distributions for the six conditions, and endwall heat transfer distributions for the six conditions. The inlet boundary layers have been documented using a single-wire probe for all six conditions at five inlet locations. These inlet locations are equally spaced at $1/5^{th}$ of the vane circumferential spacing. For the low turbulence inlet conditions the boundary layers are very thin and the lower Reynolds number inlet boundary layers show laminar behavior. The six 95% span pressure distributions provide an indication of the pressure gradients present on the endwall surface, which are drivers for secondary flows. A lampblack and oil flow visualization photo taken on a similar cascade provides an indication of the location of the separation saddle point and suction and pressure surface separation lines due to endwall pressure gradients. The six endwall surface heat transfer distributions provide a well resolved picture of influence of turbulence level and Reynolds number on the Stanton number distributions and are expected to useful for grounding computational models.

Inlet Boundary Layer Parameters and Turbulence Conditions. Inlet boundary layer measurements were taken at the inlet to the cascade at 5 circumferential positions and are documented in Table 1a and 1b for both turbulence conditions and all Reynolds numbers. The circumferential position (Y) is taken from the bottom most Y location of the suction surface of the instrumented vane as shown in figure 1. For the low turbulence condition at the low Reynolds number, the inlet boundary layers are all laminar as indicated by the skin friction coefficient, Cf/2, and the shape factor. The entering boundary layer is very thin due to the entrance contraction just upstream of the cascade test section. At the 1,000,000 chord Reynolds number, the boundary layers at the top three positions are turbulent, while the lower two stations show transitional flow. Inlet boundary layers for the low turbulence, high Reynolds number condition, are all turbulent. Determining the skin friction coefficients for the laminar and transitional boundary layers was quite uncertain, perhaps as much as 20 percent or more due to the lack of near wall velocity measurements.

Inlet boundary layer measurements for the aero-combustor simulator are presented in Table 1b for three Reynolds numbers. Generally, peak velocities occurred at the midspan of the channel so perhaps the term nonequilibrium channel flow would be a better term. These profiles are nonequilibrium in the sense they are strongly influenced by the freestream turbulence, which is convected downstream from the turbulence generator. The profiles exhibit no wake due to the turbulence interaction but are affected by the pressure gradients at the inlet plane of the cascade. Momentum thickness at a given position scales inversely with the local peak velocity. Velocity profiles suggest that the large-scale high intensity turbulence is very effective at redistributing low momentum flow. Figure 4 shows the measured velocity distribution at the highest measuring station for the highest Reynolds number compared with a fully developed nonequilibrium channel flow calculation assuming a linear shear stress distribution [$\tau/\tau_w = 1-(2y)/H$] and the ATM model of Ames, Kwon and Moffat [24]. This calculated profile is strongly influence by the nonequilibrium turbulence generated in the mock combustor and is substantially different than a typical equilibrium channel flow. However, the calculated profile has significant similarities to the measured inlet velocity profile and may be of utility as a baseline inlet profile for a combustor.

Ninety-Five Percent Span Pressure Distributions. Ninety-five percent span pressure profiles for the low and aero-combustor turbulence cases are shown in figures 5 through 7 compared with midspan profiles. The profiles are plotted in terms of Ps/Pt versus surface arc for the low through high Reynolds numbers respectively. The 95% span profiles show a reduction in minimum pressure on the near suction surface (positive surface distance) due to the secondary flows, which first move away from the suction surface and then are pushed toward and up onto the surface. The high turbulence case with the largest momentum thickness shows the biggest variation between the midspan and 95% span distributions. However, the difference between the midchord and 95% pressure distributions is not large indicating that the secondary flows have only a modest effect. Generally similar trends appear at the three Reynolds

numbers but influence of the secondary flows on the highest Reynolds number is the most significant.

Endwall Flow Visualization. A lampblack and oil endwall flow visualization is presented in figure 8 taken from Ames, Hylton, and York [6]. This figure shows the separation saddle point upstream from the vane along with the pressure surface and suction surface separation lines. The pressure side of the horseshoe vortex and the passage vortex form above the separation saddle point and are sweep upward toward the adjacent vane suction surface. The suction side of the horseshoe vortex moves downward around the suction surface and is swept up onto the surface. These flow visualization measurements were taken in a five-vane cascade at an exit Reynolds number based on chord length of 2,000,000 and an exit Mach number of 0.6. The inlet momentum thickness was about 3800, comparable to the present high turbulence case, and the inlet turbulence level was 6.5%. The geometry of the cascade used by Ames, Hylton, and York has similarities to the present cascade and the flow visualization provides some insight for the heat transfer patterns seen on the present endwall.

Endwall Stanton Number Distributions. Endwall Stanton number contours are shown in figures 9 through 14 for Reynolds numbers ranging from 500,000 to 2,000,000 with low and high turbulence levels. All Stanton numbers are based on exit conditions. Comparisons between the low freestream Stanton numbers and the mock aerocombustor Stanton number distributions have been shown on one page at a single Reynolds number. In the first comparison, Stanton number contours are shown for an exit chord Reynolds number of 500,000 for the low turbulence condition in figure 9 and for the aerocombustor in figure 10. In these figures, the middle vane has a consistent heat flux boundary condition with the black endwall surface, while the upper and lower vanes have no heating. Around the leading edge of the middle vane, Stanton number levels decrease as the thermal boundary layer thickens and then increase as the stagnation region is approached. The high heat transfer rates in this region are consistent with the horseshoe vortex with forms in this region and Stanton number levels in this regions are as high as any shown on the surface. The favorable static pressure gradient, which moves away from the stagnation region and the pressure surface tends to drive the separation line for the inlet boundary layer toward the suction surface of the adjacent vane. The results of this separation line can be seen in the jagged contour lines for the 0.0013 Stanton number and the low heat transfer island shown for the 0.0011 Stanton number. This lowest heat transfer region is consistent with the convergence of the separation streamline from the suction surface leg of the horseshoe vortex and the separation streamline due to the roll up of the pressure surface leg of the horseshoe vortex by the passage vortex. The influence of the convergence of these vortices and their lift off onto the suction surface can be seen in the Stanton number contours along the suction surfaces of the upper and middle vanes. Heat transfer levels are generally highest downstream from the trailing edge region of the vanes due to the intense generation of turbulence, which occurs in the wakes due to the velocity deficit. The trajectory of this high heat transfer island curves toward the circumferential direction. This path is consistent with the characteristic over turning near the endwall, which is typically present due the combination of endwall pressure gradients and an accumulation of low momentum fluid in the endwall region. Additionally, the presence of corner vortices along the suction surface appears to affect heat transfer in the aft region of the surface. The combination of high convective velocity and pressure gradient off the pressure surface produces a relatively high Stanton number (0.0015) in the region downstream from that surface. However, this Stanton number is significantly lower than levels in the same region for the highest Reynolds number flow. For the 500,000 Reynolds number this level of Stanton number is more consistent with laminar or transitional flow than turbulent flow for this high velocity region. The presence of the heated vane does not appear to have a strong influence for this condition. However, some significant differences are apparent down stream from the trailing edges of the vane.

The Stanton number patterns on figure 10 for the high turbulence case appear to be less affected by the secondary flows than the lower turbulence case. Other than outside of the stagnation region and downstream from the trailing edge, few patterns can be correlated with the expected secondary flow structures. This difference is likely due to the large-scale turbulence. Large-scale turbulence is very effective at mixing away gradients in the flow. Mixing is not only enhanced in the wall normal direction, but the large scale motions present in the streamwise and lateral components of turbulence are effective at both moving around flow structures and to a lesser extent mixing them away. Generally, the heat transfer appears to be about 10 to 20 percent higher in most locations for the higher turbulence case and the isotherm area seem to have a pattern which is smoother and more aligned with the geometry of the passage. This augmentation level is lower than the level found by Radomsky and Thole and is due in part to the difference in the inlet boundary layers between low and high turbulence cases. High heat transfer rates are still present in the stagnation region and downstream from the trailing edge of the vane but the effect of the separation streamline is not apparent. In this high turbulence case the heated middle vane appears to affect the level of heat transfer in the middle of the passage. This is evident by the appearance of a 0.0012 iso-Stanton number in the upper passage with no similar feature in the lower passage. Additionally, the heat transfer level in the heated vane wake is lower than the unheated vane wake.

Figure 11 presents the Stanton number patterns for the 1,000,000 exit chord Reynolds number for the low free-stream turbulence case. The patterns show many similarities to the 500,000 Reynolds number case for the low turbulence condition. However, for this higher Reynolds number the effect of the leading edge corner vortex appears to be much more evident. A low heat transfer region adjacent to mid arc on the pressure surface (St = 0.001) appears to be due to the downwash of laminar flow from the pressure surface. Again the convergence and lift off of the suction leg of the horseshoe vortex with the passage/pressure leg of the horseshoe vortex shows a noticeable influence on heat transfer at mid arc along the suction surface. Downstream from the trailing edge of the vanes, the influence of the wake is apparent on the endwall heat transfer. In addition, the highest velocities occur just downstream from the trailing edge and cause a high heat transfer location in between the lower wake and upper suction surface.

Figure 12 shows a psuedo picture of iso-Stanton numbers for the high turbulence, 1,000,000 Reynolds number case. The overall level of heat transfer is similar to that for the low turbulence case. This augmentation level is lower than the level found by Radomsky and Thole and is due in part to the relatively thin inlet boundary layers of the low turbulence case. However, similar to the lower Reynolds number comparison the iso-Stanton numbers have a pattern, which is smoother and has a weaker connection to typical secondary flow patterns. Again, the leading edge and wake footprint are regions of high heat transfer. The footprint of the wake is much wider than compared to the low turbulence case. This spreading is consistent with effects of turbulence on wake development documented by Ames and Plesniak [25]. However, this widening of the wake footprint may

also be associated with the high heat transfer area seen for the low turbulence case.

Figure 13 shows the endwall Stanton number contours for the 2,000,000 exit chord Reynolds number with the low turbulence condition. Patterns for this condition show the influence of the vortex system in the leading edge region, downstream from the trailing edge and off the suction surface where the two vortex systems merge and are swept off the endwall. The high heat transfer, which was evident off the trailing edge of the pressure surface and between the wakes, has now expanded. The endwall region just off the pressure surface shows a region of low heat transfer likely due to laminar fluid sweeping down off the surface due the cross passage pressure gradient. Downstream of this region, steep Stanton number contours correspond to significant changes in velocity occurring on the endwall in a region where the boundary layer is expected to be thin, leading to the high heat transfer region between the wake of the lower airfoil and the suction surface of the upper one. Heat transfer off the heated vane pressure surface is noticeably lower in this figure suggesting that the consistent thermal boundary condition in this case has a significant effect.

Figure 14 presents the Stanton number contours for the higher turbulence condition at a chord exit Reynolds number of 2,000,000. The patterns are much smoother than the low turbulence condition at a 2,000,000 Reynolds number but the overall level does not appear to be significantly higher. Stanton number contours through the passage seem to be tied to the local convective velocity indicating turbulent flow on the surface. The high heat transfer footprint downstream from the pressure surface trailing edge has expanded. However, unlike the low turbulence case, which shows two distinct regions, one wake generated, and one likely generated by high velocities and thin boundary layers, the high turbulence condition shows only one high heat transfer region.

Conclusions

The present endwall heat transfer data document surface heat transfer for a low inlet turbulence with relatively thin boundary layers and for a turbulence condition generated using a mock combustor, which produces peak velocities at mid channel. The data were taken at exit chord Reynolds numbers of 500,000, 1,000,000, and 2,000,000. The data have well documented inlet boundary layers and turbulence conditions and are expected to have significant merit for use in grounding predictive methods for endwall heat transfer.

The low turbulence heat transfer contours show strong evidence of the impact of secondary flows on heat transfer patterns. Not only do the leading edge horseshoe vortex and trailing edge wake show the impact of these secondary flows on raising surface heat transfer but the impact of the passage vortex and suction surface leg of the horseshoe vortex can be seen as well.

The inlet laminar boundary layers, which occurred at the lowest Reynolds number and turbulence condition, generally produced a lower average passage Stanton number by 10 to 20 percent. The overall influence of turbulence on endwall heat transfer was less dramatic for the higher Reynolds number cases. This small difference is likely due to the thin inlet boundary layers developed for the low turbulence case compared to the relatively large inlet momentum deficit of the higher turbulence case.

The high turbulence heat transfer contours show weaker evidence of the impact of secondary flows on heat transfer patterns due to the enhanced turbulent mixing and because the larger scales tend to push around the flow structures. High heat transfer rates in the leading edge and wake regions are still present due to the influence of the horseshoe vortex and wake.

The heated constant heat flux boundary condition on the vane generally had a noticeable influence on the heat transfer level in the passage and downstream in the wake region. However, the influence of the active vane surface was not shown to be dramatic.

Acknowledgements

The authors gratefully acknowledge the support from DOE's Advanced Gas Turbine System Research Program, which funded this research and to Rolls Royce of Indianapolis for providing the vane geometry used in this study. Additionally, the authors would like to acknowledge the seed grant from the North Dakota EPSCoR program, which supported the development of the large-scale low speed cascade facility used in this study. In addition, the authors are indebted to the University of North Dakota for providing additional support and laboratory space and to Jay Evenstad for machine shop support. Finally, the authors would like to acknowledge the work of Dan Pelarski, Robert Stengel, Scott Ciocetto, Jeremy Stocke, and Bobby Shimpa who helped design and fabricate the original test section as a senior design project and to Troy Lassle, Mark Hettwer, Brad Wall, and Scott Lindfors who worked as summer research assistants on this project.

References

1. Kays, W.M., and Crawford, M.E., 1993, *Convective Heat and Mass Transfer,* 3rd Edition, McGraw-Hill, New York.

2. Sieverding, C.H., 1985, "Recent progress in the understanding of basic aspects of secondary flow in turbine blade passages," ASME Journal of Engineering for Gas Turbines and Power, Vol. 107, pp. 248-257.

3. Klein, A., 1966, "Investigation of the entry boundary layer on the secondary flows in the blading of axial turbines, BHRA T 1004.

4. Langston, L.S., Nice, M.L., and Hooper, R.M., 1977, "Three-dimensional flow within a turbine cascade passage," ASME Journal of Engineering for Power, January, 1977, pp. 21-28.

5. Marchal, P., and Sieverding, C.H., 1977, "Secondary flows within turbomachinery bladings," Secondary Flows in Turbomachines, AGARD CP 214.

6. Ames, F.E., Hylton, L.D. and York, R.E., 1986, Unpublished work on the impact of the inlet endwall boundary layer on secondary losses and velocity vectors in a compressible turbine cascade, Allison Gas Turbine Division of General Motors.

7. Zess, G.A. and Thole, K.A., 2001, "Computational design and experimental evaluation of using an inlet fillet on a gas turbine vane," ASME Paper No. 2001-GT-404.

8. Burd, S.W., and Simon, T.W., "Flow measurements in a nozzle guide vane passage with a low aspect ratio and endwall contouring," ASME Journal of Turbomachinery, Vol. 122, pp. 659-666.

9. York, R.E., Hylton, L.D, and Milelc, M.S, 1984, "An experimental investigation of endwall heat transfer and aerodynamics in a linear vane cascade," ASME Journal of Engineering for Gas Turbines and Power, Vol 106., p. 159.

10. Harasgama, S.P., and Wedlake, E.T., 1989, "Heat transfer and aerodynamics of a high rim speed turbine nozzle guide vane tested in the RAE isentropic light piston cascade," Journal of Turbomachinery, Vol. 113, pp. 384-391.

11. Spencer, M. C., Jones, T. V., Lock, G. D., 1996, "Endwall Heat Transfer Measurements in an Annular Cascade of Nozzle Guide Vanes at Engine Representative Reynolds and Mach Numbers," *International*

Journal of Heat Fluid Flow, vol. 17, pp. 139-147.
12. Arts, T. and Heider, R., 1994, "Aerodynamic and thermal performance of a three dimensional annular transonic nozzle guide vane, Part-I experimental investigation," Paper No. 1994-31, 30th AIAA/ASME/SAE/ASEE Joint propulsion conference.
13. Radomsky, R., and Thole, K. A., 2000, "High Freestream Turbulence Effects in the Endwall Leading Edge Region," *Journal of Turbomachinery*, vol. 122, pp. 699-708.
14. Goldstein, R.J., and Spores, R.A., 1988, "Turbulent transport on the endwall in the region between adjacent turbine blades," Journal of Heat Transfer, Vol. 110, pp. 862-869.
15. Giel, P.W., Thurman, D.R., Van Fossen, G.J., Hippensteele, A.A., and Boyle, R.J., 1996, "Endwall heat transfer measurements in a transonic turbine cascade," ASME Paper No. 96-GT-180.
16. Boyle, R. J., and Lucci, B.L., 1996, "Predicted turbine heat transfer for a range of test conditions," ASME Paper No. 96-GT-304.
17. FLUENT 5.5, 2000, FLUENT 5.5 User's Guide, Fluent, Inc., Lebanon, N.H.
18. Hippensteele, S.A., Russell, L.M., and Torres, F.J., 1985, "Local heat-transfer measurements on a large, scale-model turbine blade airfoil using a composite of a heater element and liquid crystals," MASA Technical Memo. 86900.
19. Hippensteele, S.A., Russell, L.M., and Torres, F.J., 1986, "Use of a liquid-crystal, heater-element composite for quantitative, high-resolution heat transfer coefficients on a turbine airfoil, including turbulence and surface roughness effects, NASA Technical Memo. 87355.
20. Hippensteele, and S.A., Russell, 1988, High-resolution liquid-crystal heat-transfer measurements on the end wall of a turbine passage with variations in Reynolds number," NASA Technical Memo. 100827.
21. Jones, T.V., and Hippensteele, S.A., 1988, "High-resolution heat-transfer-coefficient maps applicable to compound-curve surface using liquid crystals in a transient wind tunnel," NASA Technical Memo. 89855.
22. Camci, C., Glezer, B., Owen, J.M., Pilbrow, and R.G., Syson, B.J., 1998, "Application of thermochromic liquid crystal to rotating surfaces," ASME Journal of Turbomachinery, Vol. 120, pp. 100-103.
23. Moffat, R.J., 1988, "Describing the uncertainties in experimental results," Experimental Thermal and Fluid Science, Vol. 1., pp. 3-17.
24. Ames, F.E., Kwon, O., and Moffat, R.J., 1999, "An algebraic model for high intensity large scale turbulence," ASME Paper No. 99-GT-160.
25. Ames, F.E. and Plesniak, M.W., "The Influence of Large Scale, High Intensity Turbulence on Vane Aerodynamic Losses, Wake Growth, and Exit Turbulence Parameters," ASME J. Turbomachinery, Vol. 119, pp. 182.

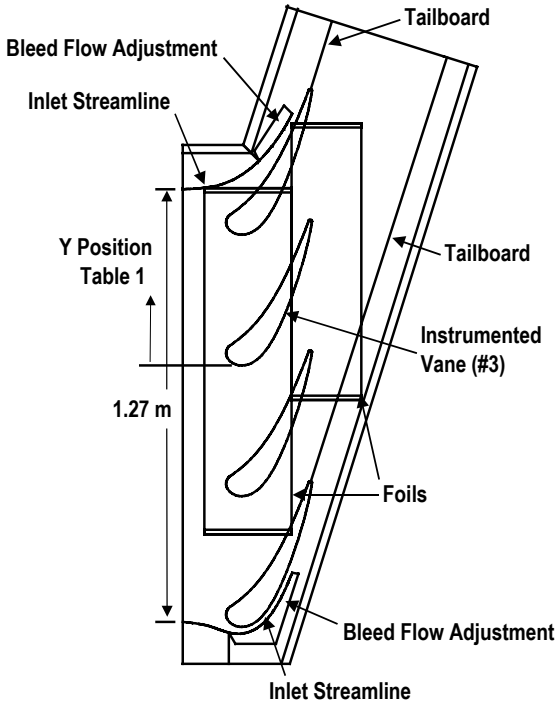

Figure 1. Schematic of UND linear cascade facility

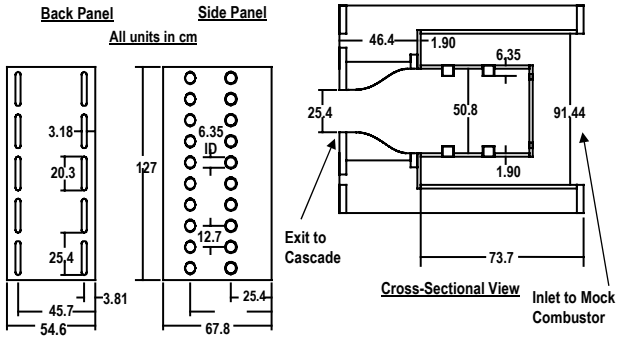

Figure 2. Schematic of mock aeroderivative combustor turbulence generator

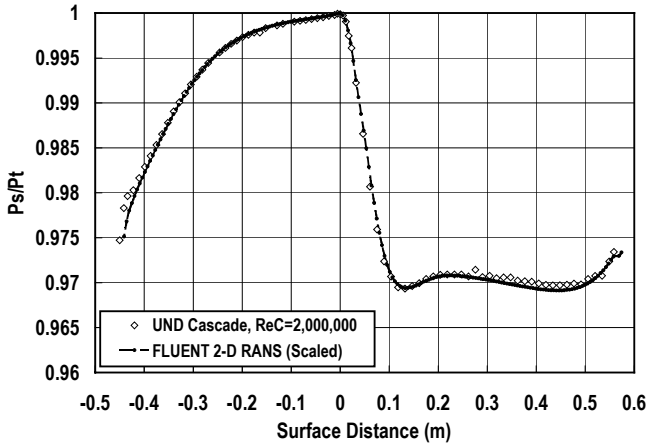

Figure 3. Comparison between measured and predicted vane midspan pressure distribution.

Low Turbulence

Reynolds	Tu	U (m/s)	Lx (cm)	Lu (cm)	ε (m^2/s^3)
500,000	0.0069	4.96	8.12	127.0	0.00005
1,000,000	0.0076	10.43	5.02	154.5	0.00035
2,000,000	0.0060	18.71	3.58	15.5	0.0144

Low Turbulence (LT) Re_C = 500,000

Y (cm)	U_∞ (m/s)	δ_2 (cm)	δ_1 (cm)	H	Cf/2	Tu_∞	$Re_{\delta 2}$
16.90	4.55	0.076	0.195	2.560	0.00099	0.0081	222
9.22	4.09	0.094	0.223	2.370	0.00097	0.0086	247
1.54	4.63	0.102	0.243	2.390	0.00087	0.0070	301
-6.14	5.82	0.098	0.228	2.320	0.00080	0.0067	362
-13.82	5.26	0.091	0.235	2.580	0.00075	0.0076	300

Low Turbulence (LT) Re_C = 1,000,000

Y (cm)	U_∞ (m/s)	δ_2 (cm)	δ_1 (cm)	H	Cf/2	Tu_∞	$Re_{\delta 2}$
16.90	8.63	0.054	0.095	1.770	0.00270	0.0079	297
9.22	7.59	0.062	0.105	1.700	0.00280	0.0087	302
1.54	9.80	0.058	0.093	1.590	0.00297	0.0043	370
-6.14	11.83	0.064	0.122	1.930	0.00165	0.0036	486
-13.82	10.65	0.070	0.148	2.110	0.00130	0.0050	484

Low Turbulence (LT) Re_C = 2,000,000

Y (cm)	U_∞ (m/s)	δ_2 (cm)	δ_1 (cm)	H	Cf/2	Tu_∞	$Re_{\delta 2}$
16.90	16.03	0.063	0.095	1.520	0.00245	0.0080	647
9.22	15.70	0.074	0.127	1.530	0.00230	0.0087	743
1.54	19.52	0.071	0.102	1.440	0.00243	0.0057	874
-6.14	22.92	0.057	0.081	1.430	0.00253	0.0046	821
-13.82	19.94	0.053	0.082	1.530	0.00234	0.0050	671

Table 1a. Endwall inlet boundary layer parameters, low turbulence condition

Aero-Combustor

Reynolds	Tu	U (m/s)	Lx (cm)	Lu (cm)	ε (m^2/s^3)
500,000	0.1313	5.24	3.68	7.24	6.67
1,000,000	0.1402	9.32	3.52	6.36	51.5
2,000,000	0.1339	18.39	3.58	7.35	302.0

Aero-Combustor (AC) Re_C = 500,000

Y (cm)	U_∞ (m/s)	δ_2 (cm)	δ_1 (cm)	H	Cf/2	Tu_∞	$Re_{\delta 2}$
16.90	4.83	0.726	0.889	1.226	0.00250	0.1567	2238
9.22	4.41	0.786	0.988	1.261	0.00220	0.1732	2184
1.54	5.40	0.411	0.500	1.217	0.00275	0.1321	1409
-6.14	6.09	0.360	0.428	1.189	0.00298	0.1097	1408
-13.82	5.48	0.456	0.544	1.195	0.00280	0.1270	1599

Aero-Combustor (AC) Re_C = 1,000,000

Y (cm)	U_∞ (m/s)	δ_2 (cm)	δ_1 (cm)	H	Cf/2	Tu_∞	$Re_{\delta 2}$
16.90	8.43	0.706	0.860	1.217	0.00225	0.1625	3774
9.22	7.88	0.806	0.997	1.245	0.00191	0.1720	3890
1.54	9.51	0.382	0.456	1.201	0.00248	0.1350	2235
-6.14	11.10	0.278	0.322	1.160	0.00295	0.1073	1928
-13.82	9.90	0.311	0.368	1.181	0.00278	0.1255	1953

Aero-Combustor (AC) Re_C = 2,000,000

Y (cm)	U_∞ (m/s)	δ_2 (cm)	δ_1 (cm)	H	Cf/2	Tu_∞	$Re_{\delta 2}$
16.90	16.96	0.575	0.860	1.193	0.00190	0.1557	6217
9.22	15.33	0.627	0.767	1.223	0.00151	0.1741	6121
1.54	18.60	0.306	0.359	1.178	0.00221	0.1287	3557
-6.14	21.47	0.237	0.269	1.136	0.00265	0.1034	3247
-13.82	19.37	0.268	0.312	1.165	0.00232	0.1197	3311

Table 1b. Endwall inlet boundary layer parameters, aero-combustor condition

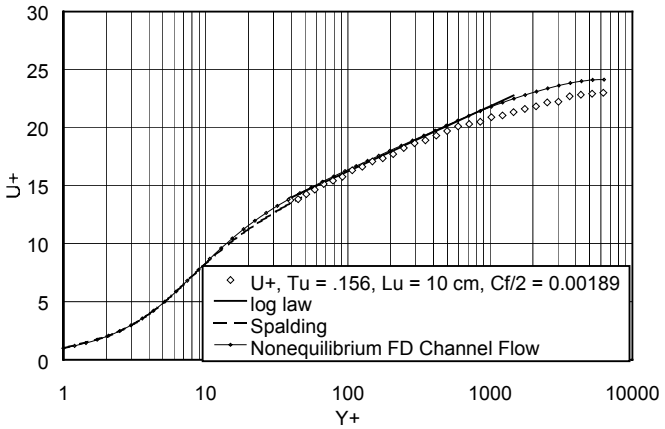

Figure 4. Cascade Inlet Velocity Profile Compared with Nonequilibrium FD Channel Flow, ATM, top position, Re_C = 2,000,000.

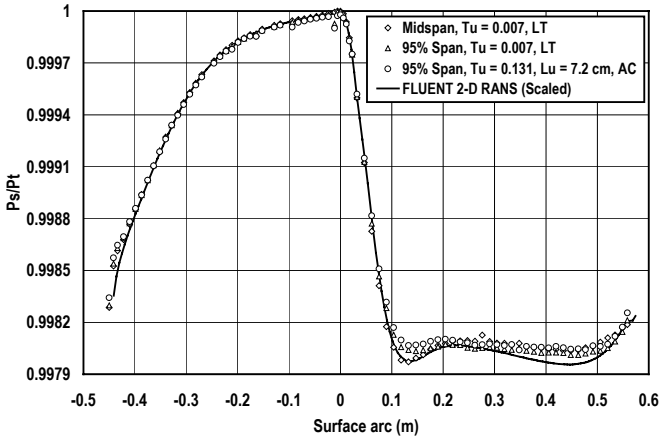

Figure 5. Comparison of 95% span pressure distributions with midspan values, $Re_C = 500{,}000$

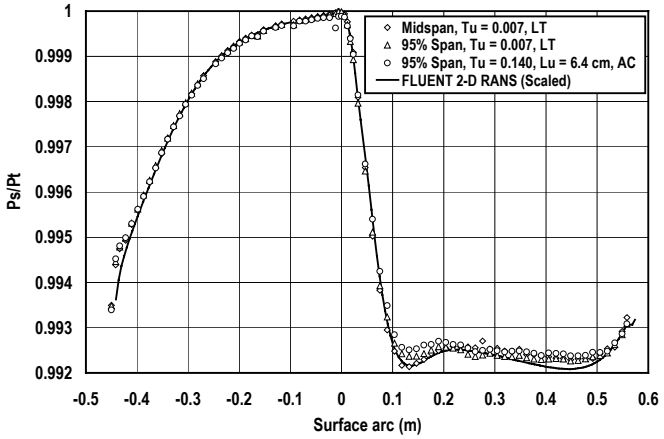

Figure 6. Comparison of 95% span pressure distributions with midspan values, $Re_C = 1{,}000{,}000$

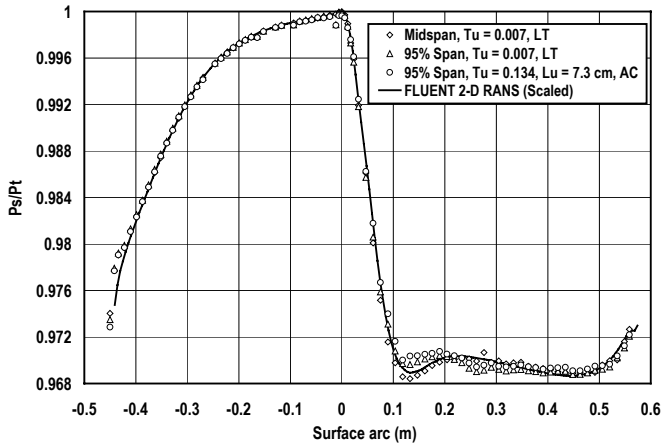

Figure 7. Comparison of 95% span pressure distributions with midspan values, $Re_C = 2{,}000{,}000$

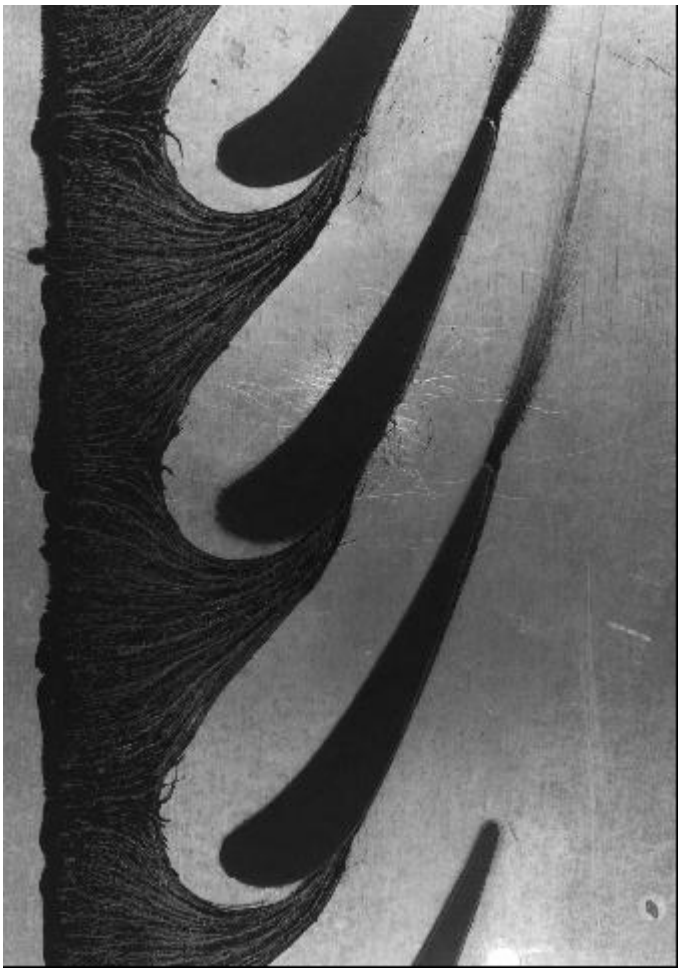

Figure 8. Endwall flow visualization using lampblack and oil showing the separation saddle point and pressure and suction surface separation lines. (Ames, Hylton, and York

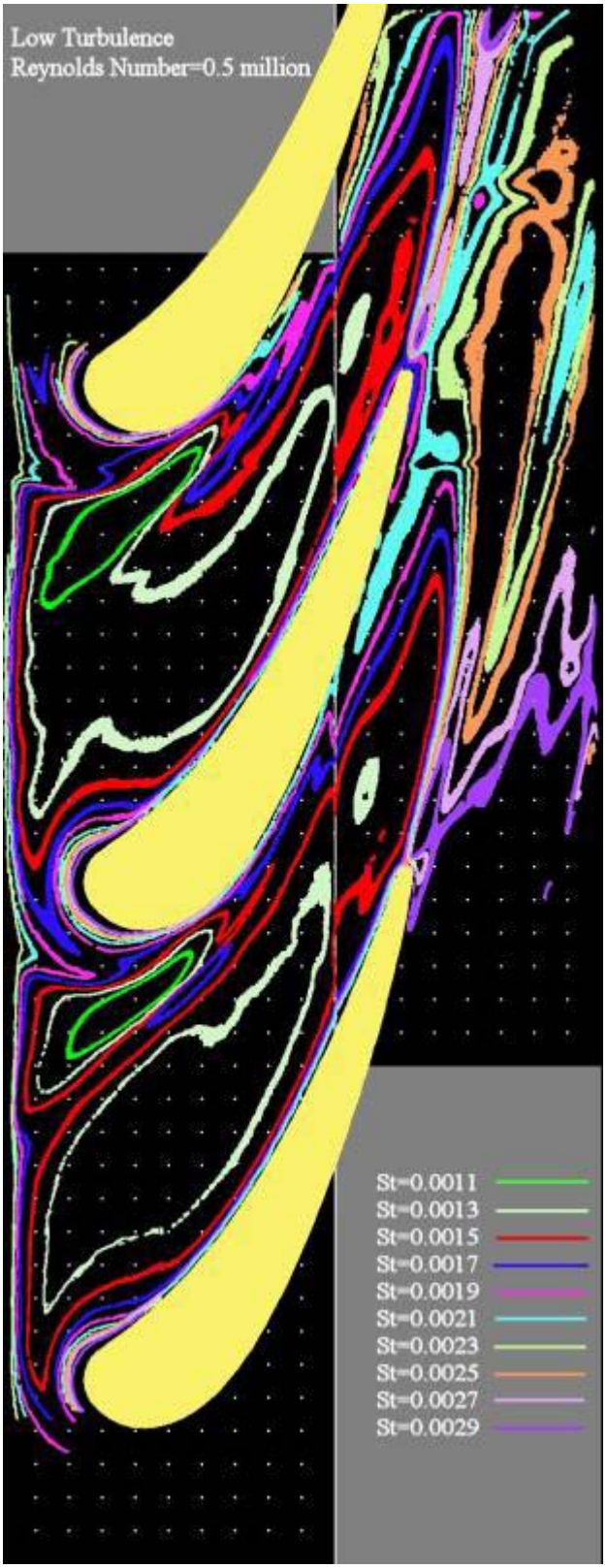

Figure 9. Endwall Stanton number contours, LT, Tu = 0.007, Re_C = 500,000.

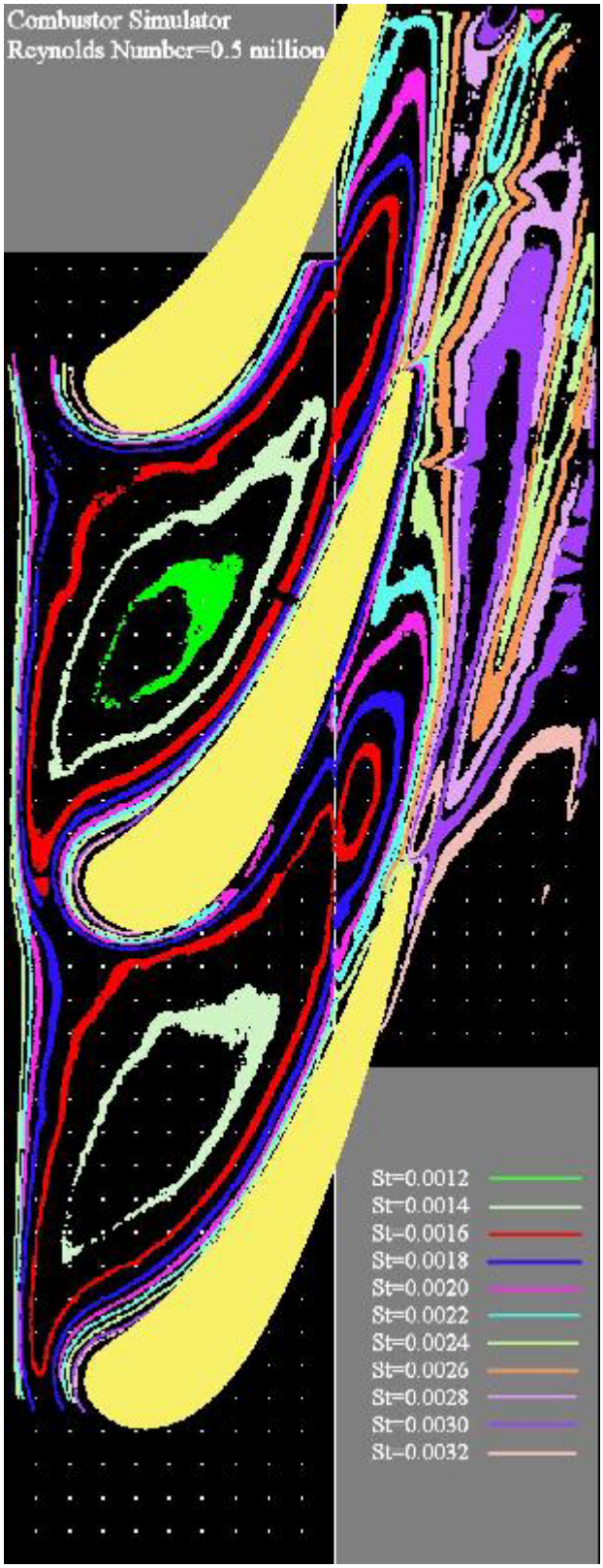

Figure 10. Endwall Stanton number contours, AC, Tu = 0.131, Lu = 7.2 cm, Re_C = 500,000.

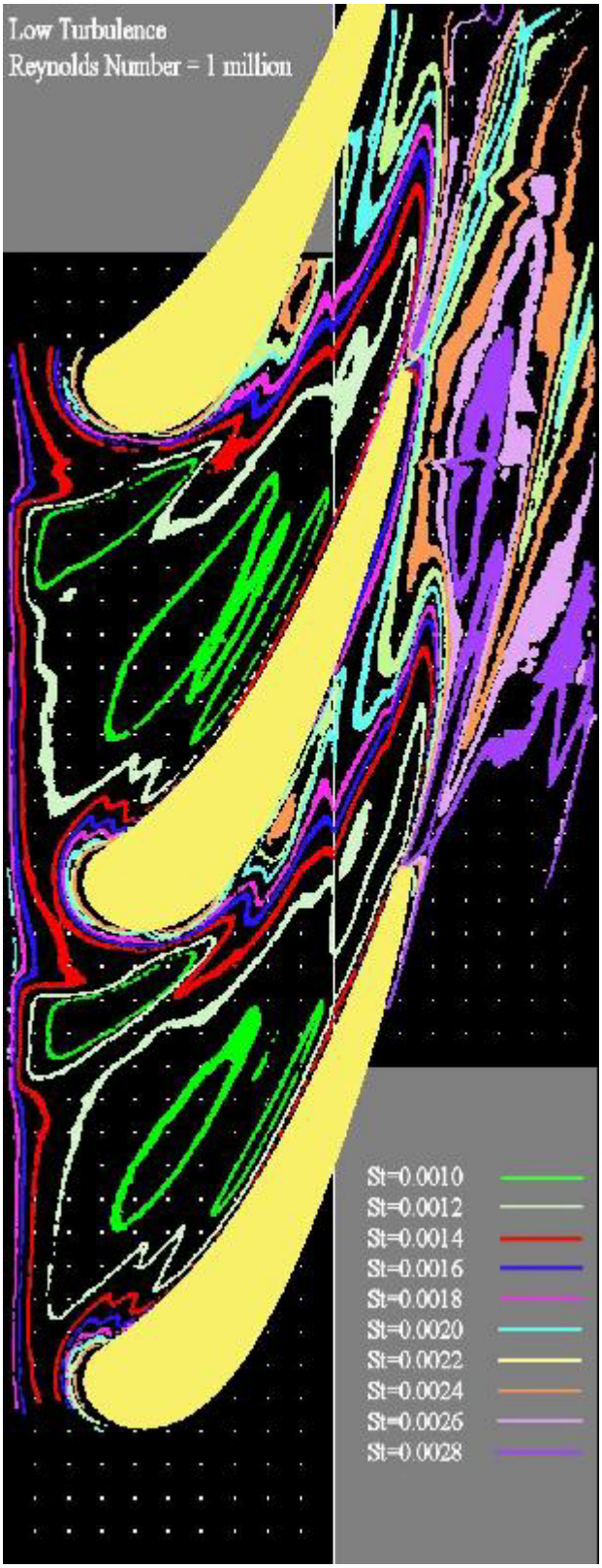

Figure 11. Endwall Stanton number contours, LT, Tu = 0.007, Re_C = 1,000,000

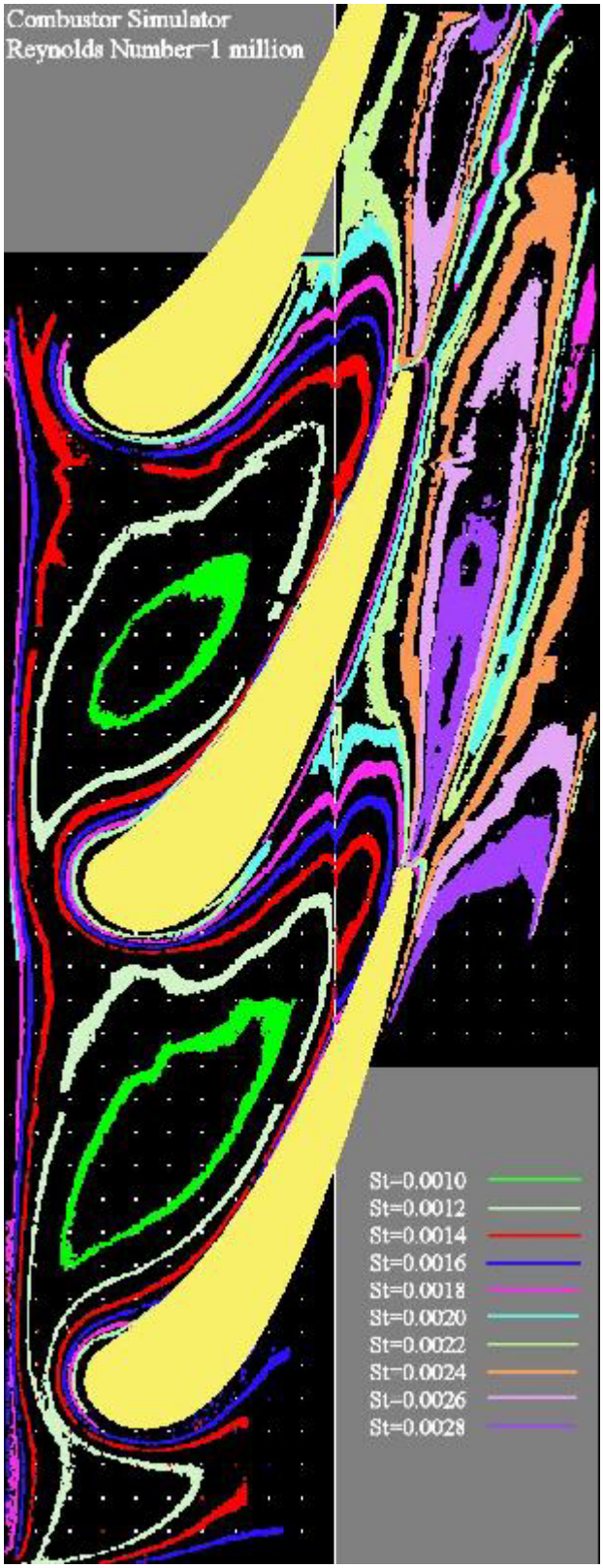

Figure 12. Endwall Stanton number contours, AC, Tu = 0.140, Lu = 6.4 cm, Re_C = 1,000,000

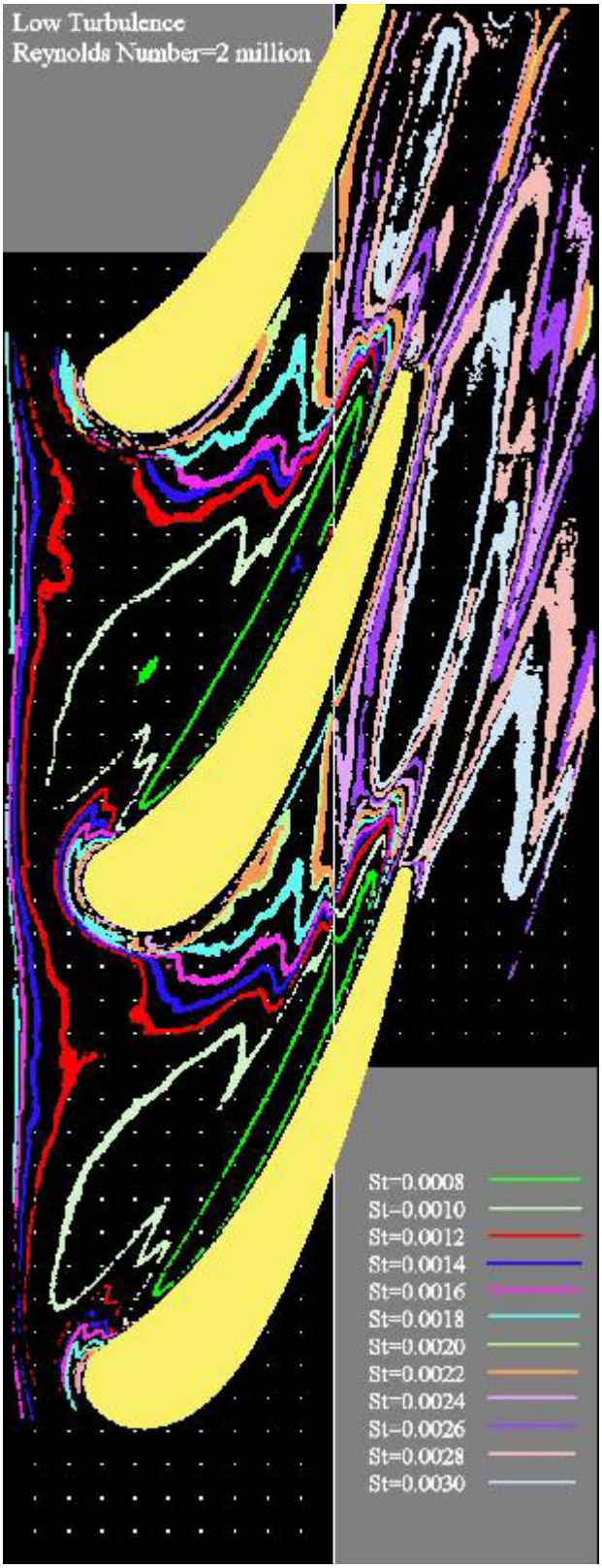

Figure 13. Endwall Stanton number contours, LT, Tu = 0.007, Re_C = 2,000,000

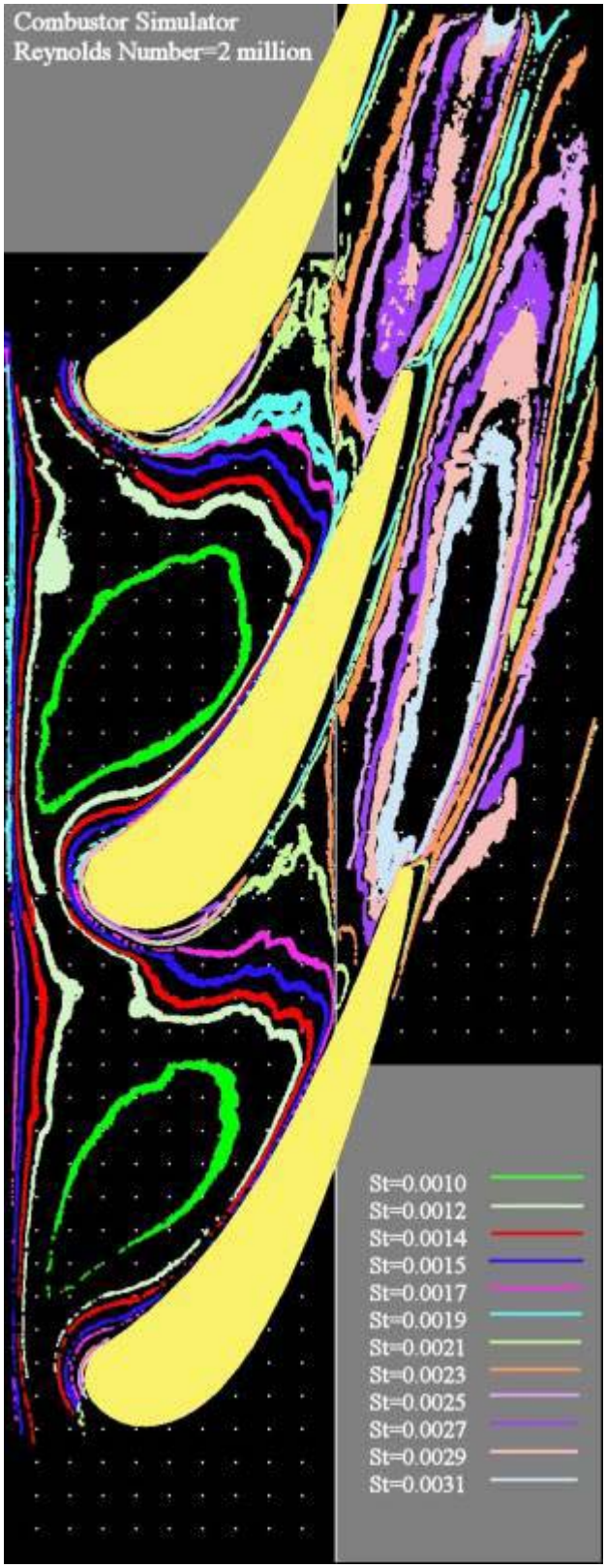

Figure 14. Endwall Stanton number contours, AC, Tu = 0.134, Lu = 7.3 cm, Re_C = 2,000,000

Annual Report for:

AGTSR Project No. SR-094

Rotating Heat Transfer in High Aspect Ratio Rectangular Cooling Passages with Shaped Turbulators

J.C. Han

(Principal Investigator)

Department of Mechanical Engineering, Texas A&M University

Ph: (979) 845-3738 **Fax: (979) 862-2418 **E-mail: JCHan@mengr.tamu.edu

and

H.C. Chen

(Co-Principal Investigator)

Department of Civil Engineering, Texas A&M University

August 31, 2002

TABLE OF CONTENTS

PROJECT SUMMARY

The objective of this two-part investigation is to provide the designers with new internal cooling data for improving the cooling performance and thermal efficiency of power generation and industrial gas turbine engines. More specifically, this investigation ventures into the heat transfer phenomenon of internal cooling channels with shaped turbulators. The research is divided into two parts: Part I - Rotating Heat Transfer and Part II - Numerical Prediction. This investigation is a collaboration between Dr. J.C. Han and Dr. H.C. Chen of Texas A&M University. This report details the first stage of this investigation, namely the rectangular channel with V-shaped rib turbulators. A more detailed breakdown of the investigation of each of the two parts follows.

Part I: Rotating Heat Transfer

The objectives of part I are to obtain experimental data from rectangular, two-pass internal cooling passages with higher aspect ratios of 2:1 and 4:1. The following parameters will be altered: (1) Surface geometry, (2) Reynolds numbers, (3) rotation number, (4) rotation angle, and (5) channel aspect ratio. Angled ribs, V-shaped ribs, and delta-shaped turbulators will be installed on the leading and trailing sides of a rectangular internal cooling passage with rotation. The ratio of inlet coolant temperature to surface temperature (TR) will be around 0.8 - 0.9. The experiments will be designed so that (a) regionally averaged heat transfer coefficients will be measured at different locations along the cooling passages with enhanced surfaces, and (b) pressure drops will be measured along the cooling passages under rotating conditions. The new heat transfer and pressure drop data will be correlated and compared with numerical predictions

in part II. The existing rotating facility and instrumentation available in the Turbine Heat Transfer Laboratory of Texas A&M University will be employed for the proposed study.

Part II: Computational Study

The objectives of part II are to predict flow and heat transfer behaviors from rectangular, two-pass internal cooling passages with higher aspect ratios of 2:1 and 4:1. An ongoing Chimera Reynolds-Averaged Navier-Stokes (RANS) code together with an advanced state of the art second-order Reynolds stress (second moment) turbulence model will be used for the prediction of rotating rectangular cooling channels with angled ribs, V-shaped ribs, and delta-shaped turbulators. The present numerical model has been tested to provide much better flow and heat transfer predictions than the standard k-ε turbulence model for rotating multi-pass square channels with angled ribs. The numerical predictions will be calibrated/compared with the part I-rotation heat transfer data. The ultimate goal is to predict and optimize flow and heat transfer in rotating rectangular channels with various shaped turbulators at very high Reynolds number and buoyancy parameter conditions.

PART I: ROTATING HEAT TRANSFER

Part 1 is conducted at Texas A&M University under the direction of Dr. J.C. Han

HEAT TRANSFER IN TWO-PASS ROTATING RECTANGULAR CHANNELS (AR=2) WITH FIVE DIFFERENT ORIENTATIONS OF 45° V-SHAPED RIB TURBULATORS

ABSTRACT

An experimental study was made to obtain heat transfer data for a two-pass rectangular channel (aspect ratio=2:1) with smooth and ribbed surfaces for two channel orientations (90º and 135º with respect to the plane of rotation). The V-shaped ribs are placed on the leading and trailing surfaces. Five different arrangements of 45° V-shaped ribs are studied. The Reynolds number and rotation number ranges are 5000-40000, and 0.0-0.21, respectively. The rib height to hydraulic diameter ratio (e/D) is 0.094; the rib pitch-to-height ratio (P/e) is 10; and the inlet coolant-to-wall density ratio ($\Delta\rho/\rho$) is maintained around 0.115 for every test. The results show that the rotation-induced secondary flow enhances the heat transfer of the first pass trailing surface and second pass leading surface. However, the first pass leading and the second pass trailing surfaces show a decrease in heat transfer with rotation. The results also show that parallel 45º V-shaped rib arrangements produce better heat transfer augmentation than inverted 45° V-shaped ribs and crossed 45º V-shaped ribs, and a 90º channel orientation produces greater rotating effect on heat transfer than a 135º orientation.

INTRODUCTION

To achieve high thermal efficiency in a gas turbine engine, the turbine inlet gas temperature should be increased. However, the penalty is a high thermal load, which

affects the durability of the turbine components. Therefore, improved cooling techniques such as film cooling and internal cooling are applied to turbine blades. Internal cooling is achieved by circulating low enthalpy air in multi-pass flow channels inside the blade structure. To increase the heat transfer of the internal cooling, the internal surfaces usually are roughened by angled ribs to trip the boundary layer and increase turbulence. As the turbine blade rotates, Coriolis and buoyancy forces cause different heat transfer behavior between the leading and trailing surfaces.

Over the past few decades numerous studies have been made experimentally on the flow field and heat transfer in the internal coolant passages of gas turbine rotor blades. Metzger et al. [1] studied forced convection in a non-rotating two-pass smooth rectangular channel by varying the divider location and the gap at the 180^{o} turn. Fan et al. [2] extended the Metzger et al. [1] work by varying the channel width and concluded that increasing the channel aspect ratio resulted in smaller azimuthal heat transfer variations and increased overall channel heat transfer. Han and Park [3] performed experimental studies on heat transfer characteristics in a non-rotating rib-roughened rectangular channel. Han et al. [4] studied the effect of the rib angle orientation on heat transfer distributions and pressure drop in a non-rotating square channel with two opposite in-line ribbed walls. They found that the 60^{o} and 45^{o} V-shaped ribs performed better than the 60^{o} and 45^{o} parallel ribs and, subsequently, better than the 60^{o} and 45^{o} crossed ribs and the 90^{o} rib. The V-shaped ribs produced the highest heat transfer augmentation, while the crossed ribs had the lowest heat transfer enhancement. Taslim et al. [5] measured heat transfer and friction in channels roughened with angled V-shaped and discrete ribs on two opposite walls. Ekkad and Han [6] performed a detailed study on

heat transfer distributions in a non-rotating square ribbed channel using a liquid crystal technique. The results show that the 60°, V-shaped ribbed channel produced more heat transfer enhancement than 60° and 90° angled ribbed channels. Kiml et al. [7] investigated heat transfer enhancement mechanisms in a rectangular channel with V- and Λ- shaped ribs. They used a flow visualization technique to examine the secondary flow behaviors created by the V-shaped ribs.

Recently, experiments with rotation have been conducted to closely model turbine blade cooling environments. Wagner et al. [8, 9] conducted a detailed experimental study to determine the effects of rotation (buoyancy and Coriolis forces) on the local heat transfer of a multi-pass square channel with smooth walls. They concluded that in the first pass with radially outward flow, rotation created a thinner boundary layer with higher heat transfer on the trailing surface and a thicker boundary layer with lower heat transfer on the leading surface. In the second pass with radially inward flow, opposite heat transfer results were obtained. Johnson et al. [10, 11] performed a systematic investigation of the effects of buoyancy and Coriolis forces on the heat transfer coefficient distribution of a four-pass square channel with 45° ribs angled to the flow. They concluded that both the rotation and channel orientation with respect to the axis of rotation could change the leading and trailing surface heat transfer coefficients of the ribbed channel. Han et al. [12] investigated an uneven wall temperature effect on local heat transfer in a rotating two-pass square channel with smooth walls. Zhang et al. [13] analyzed the heating condition effects in a two pass square channel with 60° angled rib turbulators with rotation. They suggested that an uneven wall temperature had a significant impact on the local heat transfer coefficients. Parsons et al. [14, 15] studied

the effects of channel orientation and wall heating condition on the local heat transfer coefficient in a rotating two-pass square channel with ribbed walls. They found that the effects of the Coriolis force were reduced as the channel orientation changed from a normal (β=90°) to an angled orientation (β=135°). Dutta and Han [16] also investigated the local heat transfer coefficients in rotating smooth and ribbed two-pass square channels with three channel orientations. Dutta et al. [17] presented experimental heat transfer results for turbulent flows through a rotating two-pass rib-roughened triangular channel, with two channel orientations with respect to the direction of rotation. Taslim et al. [18, 19] studied the heat transfer characteristics in rib-roughened square and rectangular orthogonal rotating channels. They used a liquid crystal technique to study the effect of rotation on heat transfer distributions on the walls. They found that rotational effects were more pronounced in rib-roughened channels, with a higher channel aspect ratio and a lower rib blockage ratio. Prabhu and Vedula [20] investigated the pressure drop distribution in a rotating rectangular channel with transverse ribs on one wall. They found that a rib array with a pitch-to-height ratio of 5 caused the largest pressure drop. In addition, Park et al. [21] conducted experimental work using Naphthalene sublimation to study the effects of the Coriolis force, 180° turn, channel orientation, and the different rib arrangements on local heat/mass transfer distributions on the leading and trailing walls of a two-pass square channel. Azad et al. [22] experimentally investigated the heat transfer distribution in two-pass rotating rectangular channels (AR=2:1) connected by a 180° turn. The results showed that parallel 45° angled ribs produced higher heat transfer distribution than crossed 45° angled ribs. For a more comprehensive compilation of turbine blade cooling research, please see the book by Han et al. [23].

Following the above-mentioned research, few papers can be found in the open literature studied the rectangular cross section channel with rotation condition. Hence, the first aim was to study two pass rectangular channels (AR=2:1) that are connected by a sharp 180° turn. The second motivation was to find different rib configurations that trip the boundary layer and promote more heat transfer inside the two-pass rectangular channels. However, it was found from a previous study by Han et al. [4] that the 45° V-shaped ribs show higher heat transfer performance in a one-pass non-rotating square duct compared to other rib configurations (45° angled ribs or transverse 90° ribs). Thus, we have chosen 45° V-shaped ribs to be placed on the leading and trailing surfaces of the two-pass rotating rectangular channels since they have shown a potential for higher heat transfer enhancement. A comprehensive study was conducted to cover five different arrangements of 45° V-shaped ribs and a comparison with 45° V-shaped crossed rib case. In addition, the effect of the channel orientation with respect to the axis of rotation was investigated for two positions β =90° and β =135°. Such experimental data is not available in the open literature. Our research shows the combined effect of the 45° V-shaped rib induced secondary flow and rotation induced secondary flow on the heat transfer distribution in the two-pass rectangular cross-sectional channels.

DESCRIPTION OF THE EXPERIMENT

The experimental test rig used by Azad et al. [22] is employed in this study. Figure 1 shows the schematic of the experimental test rig. Compressed air goes through a filter and an orifice meter, then passes through a rotary seal and a hollow-rotating shaft to feed the test section. The test section is mounted in a horizontal plane. Air travels outward in the first pass and inward in the second pass, and then exhausts into the atmosphere. Slip

rings transfer thermocouple outputs to the data logger and power input from transformers to strip heaters, which are fixed under the copper plates. An electric motor with an adjustable frequency controller rotates the test section. A digital photo tachometer measures the rotational speed of the rotating shaft.

Figure 2 shows a cross sectional view of the test section. The test section has two passes. Each pass is 12.7 mm by 25.4 mm in cross section. The first pass starts with an unheated nylon entrance channel to establish a fully developed flow at the entrance to the heated channel. It has twelve (12) hydraulic diameter lengths to achieve the task. The heated channel length-to-hydraulic diameter (*L/D)* ratio is 18, while each pass length-to-hydraulic diameter (*L/D*) ratio is 9, connected by a sharp 180^{o} turn. The ratio of the mean rotating arm radius to the channel hydraulic diameter (*R/D*) is 30. The flow in the first pass is radially outward and the flow in the second pass is radially inward. The heated section is divided into twelve longitudinal sections, six sections in the first pass and six in the second pass, to obtain regionally average heat transfer coefficients. Each longitudinal section has four copper plates on four walls (one per wall) of the channel. Each copper plate is surrounded circumferencially by a thin nylon strip that has a 1.59 mm thickness for insulation from neighboring plates. The copper plates are mounted in a nylon substrate, which comprises the bulk of the test section. Pre-fabricated flexible heaters are installed beneath the leading and trailing surfaces. The side walls are each heated by a wire-wound resistance heater, which is also installed beneath the copper plates. All heaters supply steady, uniform heat flux to the copper plates. Sufficient power is supplied in order to maintain a maximum wall temperature of nearly 65°C for the corresponding section. This corresponds to an inlet coolant-to-wall density (temperature)

ratio ($\Delta\rho/\rho$) of 0.115 for every test. Each 1/8 in. (0.318 cm) thick copper plate has a 1/16 in. (0.159 cm) deep blind hole drilled into its backside in which a copper-constantan thermocouple is installed 1/16 in. (0.159 cm) from the plate surface with thermal conducting glue. The inlet and exit bulk temperatures are measured by thermocouples. The 45° V-shaped ribs with a square cross section are made of brass and are glued on the wider walls (leading and trailing surfaces) of the rotating channel. A thin layer of conductive glue is used so that it creates a negligible thermal insulation effect between the brass ribs and the copper plates. The rib-increased surface area is 25% with respect to the smooth wall. The entire test duct is surrounded by insulating nylon material and fits in a hollow cylindrical arm for structural rigidity.

DATA REDUCTION

The local heat transfer coefficient is calculated from

$$h = q_{net}/[A(T_w - T_{bx})] \qquad (1)$$

Local net heat transfer rate is the electrical power generated from the heater ($q=VI$) minus losses. Losses were determined by supplying electrical power to the test section until a steady state condition is achieved for a no flow (without any airflow) condition. This is done for several power inputs to obtain a relation between the total heat loss from each surface and the corresponding surface temperature. To place the results on a common basis, the heat transfer area used in equation (1) was always that of a smooth wall. The local wall temperature is obtained from thermocouples that impeded in each copper plate. The bulk mean air temperatures entering and leaving the test section are measured by thermocouples. The local bulk mean temperature (T_{bx}) used in equation (1) is calculated from the linear interpolation between the measured inlet and exit air bulk

temperatures. The bulk mean temperature rise at the lowest Reynolds number is around 20°C. Another way to find the local bulk mean air temperature is determined by marching along the test section and calculating the temperature rise from the local net heat input through each set of four heated surfaces. The difference between the calculated and measured outlet bulk mean temperature is between 1-2 °C in all of the cases.

Local Nusselt number is normalized by the Nusselt number for the fully developed turbulent flow in a smooth stationary circular pipe to reduce the influence of the flow Reynolds number on the heat transfer coefficient. Local Nusselt number normalized by the Dittus-Boelter/McAdams correlation is:

$$Nu/Nuo=(hD/K)/[0.023*Re^{0.8}*Pr^{0.4}] \qquad (2)$$

The Prandtl number (Pr) for air is 0.71. Air properties are taken based on the mean bulk air temperature.

The uncertainty of the local heat transfer coefficient depends on the uncertainties in the local wall and bulk air temperature difference and the net heat input for each test run. The uncertainty increases with the decrease of both the local wall to bulk air temperature difference and the net heat input. The temperature uncertainty is around 0.5°C. The flowrate uncertainty is less than 4%. Based on the method described by Kline and McClintock [24], the typical uncertainty in the Nusselt number is estimated to be less than 9% for Reynolds number larger than 10000. The maximum uncertainty, however, could be up to 23% for the lowest heat transfer coefficient at the lowest Reynolds number tested (Re=5000).

RESULTS AND DISCUSSION

Figure 3 shows the 45° angled rib that was divided at the centerline to make the 45° V-shaped rib. There are two different orientations of the V-shaped rib. The first orientation is called the 45° V-shaped rib and the second orientation is called the inverted 45° V-shaped rib. Figure 3 also shows the conceptual view of secondary flow induced by the 45° angled rib, the 45° V-shaped rib, and the inverted V-shaped rib. The 45° angled rib induces a secondary flow that moves parallel to the rib from the left side to the right side and returns back to the left side making a counter rotating vortex. The conjectured counter rotating vortex induced by the 45° angled ribs has been confirmed from numerical calculations by Al-Qahtaini et al. [25].

It is further conjectured that the 45° V-shaped rib creates two counter rotating vortices. As the fluid approaches the V-shaped rib, it splits into two streams. Each one moves parallel to the rib from the centerline to either the left side or the right side and returns back to the centerline making a counter-rotating vortex. Another observation can be drawn that as the 45° V-shaped rib is half the 45° angled rib, the boundary layer thickness for the fluid that moves parallel to one side of the 45° V-shaped rib is thinner than produced by the 45° angled rib. Therefore, since the 45° V-shaped rib produces two counter rotating vortices that promote more mixing in the bulk main stream and at the same time produce a thinner boundary layer near the heated surface, a higher heat transfer rate is expected when compared to the 45° angled rib. However, a different situation can be observed in the inverted 45° V-shaped rib. As the fluid approaches the near surface of the inverted 45° V-shaped rib, it starts moving simultaneously from the left side and right side to the centerline, interacting with each other, and then returns back

to the starting positions creating two counter rotating vortices. The vortices' interaction may weaken the two counter rotating vortices. Thus, the 45° V-shaped rib is expected to perform better than the inverted 45° V-shaped rib in the non-rotating condition.

Figure 4 shows conceptual views for the secondary flow patterns of a smooth and ribbed rotating two-pass rectangular channel. Figure 4-a shows the smooth channel that rotates at β=90° with respect to the direction of rotation. Two symmetrical cells of counter rotating secondary flow (dotted line) appear due to the Coriolis force. In the first pass of the channel, the fluid moves in a radially outward direction, and the effect of the Coriolis force directs the coolant from the core toward the trailing surface. This causes an increase of the heat transfer from the trailing surface and a decrease in the heat transfer from leading surface. However, in the second pass, the opposite situation can be seen: the fluid moves in a radially inward direction, and the Coriolis force directs the coolant toward the leading surface, causing an increase of heat transfer from the leading surface and a decrease in the heat transfer from trailing surface. When the channel is positioned at the β=135° orientation, the secondary flow vortices are asymmetric and migrate diagonally away from the corner region of the inner-leading surface toward the center in the first passage, and from the corner region of the inner-trailing surface toward the center in the second passage.

Figures 4-b through 4-e show four different arrangements of the parallel 45° V-shaped ribs. These parallel arrangements are attached to leading and trailing surfaces in a parallel fashion so that they are directly opposite to each other. Figure 4-b shows that the 45° V-shaped ribs are attached to the leading and trailing surfaces in both passes. Also, it shows the secondary flow (dotted line) induced by rotational forces and the secondary

flow (solid line) induced by the 45° V-shaped ribs. As the channel angle changes to β=135°, the rib secondary flow is unchanged, but the rotational secondary flows are shared between the principle surfaces (trailing, and leading) and side surfaces. Figure 4-c shows the same channel except that the first pass rib orientation is reversed to become inverted 45° V-shaped ribs to the mean stream flow. Consequently, all secondary flows that are induced by rotational forces or ribs are the same as case (b) except the rib secondary flow in the first pass is reversed due to the changing in the rib orientation in the first pass. For case (d), as seen in Figure 4-d, the first pass has 45° V-shaped rib, and the second pass has inverted 45° V-shaped rib. Figure 4-e shows the first pass and second pass to have inverted 45° V-shaped.

Figure 4-f shows the crossed rib case (the ribs on the leading and trailing surfaces of the cooling channels are in crossed orientation). The crossed orientation of the 45° V-shaped ribs coalesces the two pairs of counter rotating vortices into one pair of counter rotating vortices. This reduction in number of rib-induced secondary flow vortices limits the mixing between the near wall flow (hot fluid) and the core flow (cold fluid), which causes less heat transfer. In case of rotation, a pair of rotating-induced secondary flow vortices appears and moves in the opposite direction the vortices generated by crossed ribs. This negative interaction minimizes the rotation effect by suppressing flow impingement on the first pass trailing and second pass leading surfaces and restricts mixing with the core for both leading and trailing surfaces in both passes, which causes low heat transfer enhancement.

Figures 5-10 show the regionally average Nusselt number ratios (Nu/Nuo) from leading and trailing surfaces for four Reynolds number (5000, 10000, 25000, 40000), rotating and non-rotating, and two channel orientations (β=90°, 135°).

Smooth Case Results

Figure 5 shows the results of Nusselt number ratios from leading and trailing surfaces for the smooth case. For the stationary case, the Nusselt number ratio decreases monotonically for both leading and trailing surfaces in the first pass. This continuous decrease is due to the developing thermal boundary layer. As the flow approaches the 180° turn, the Nusselt number increases due to secondary flows induced by the 180° turn. The Nusselt number reaches the peak value at the entrance of the second pass and then decreases as the flow moves to the exit of the second pass. This is due to the diminishing of the 180° turn-induced secondary flows. However, in the rotation case, the Nusselt number ratios from the first pass trailing and second pass leading surfaces are higher than in the non-rotating case, while those from the first pass leading and second pass trailing surfaces are lower. This is due to the rotation-induced secondary flow vortices as shown in Fig. 4-a. At channel orientation β=90°, rotational secondary flow vortices produced by the Coriolis forces are impinging normally on the trailing surface of the first pass and the leading surface of the second pass. However, at channel orientation β=135°, the rotation secondary flow vortices are impinging on the first pass trailing-side corner and the second pass leading-side corner, as shown in Fig. 4-a. Thus, the Nusselt number ratio for the trailing surface of the first pass and the leading surface of the second pass for channel orientation β=135° are lower than the ratios for channel orientation β=90°. The opposite situation is observed in the leading surface of the first pass and the trailing surface of the

second pass. The results also show that the effect of rotation decreases with increasing Reynolds number (or decreasing rotation number). The above-mentioned results are consistent with the previous study (see Azad et al. [22]).

Parallel 45° V-shaped Rib Cases

Figure 6 shows the Nusselt number distribution for case (b). The stationary case results show that the peak Nusselt number ratio occurs at the downstream location of the inlet rather than at the entrance region of the first pass as in the smooth case. This is due to the two pairs of counter rotating secondary flow vortices that are generated by the parallel 45° V-shaped ribs, as shown in Fig. 4-b. But, the Nusselt number ratio decreases as the vortices are suppressed by the 180° turn. Then, the Nusselt number ratio increases again downstream of the second pass inlet as the secondary flow vortices induced by the parallel 45° V-shaped ribs start to develop.

The results show that rotation significantly increases the Nusselt number ratio on the first pass trailing surface and the second pass leading surface, but significantly decreases the Nusselt number ratio on the first pass leading and second pass trailing surfaces. This is because of the combined effect of the rib-induced secondary flow and the rotation-induced secondary flow vortices, as explained in Fig. 4-b. The results of the 135° channel also show that rotation enhances the heat transfer in the first pass trailing and second pass leading surfaces, whereas the heat transfer decreases in the first pass leading and second pass trailing surfaces. However, the differences in Nusselt number ratios between leading and trailing surfaces are not as significant for the 135° orientation as they are for the 90° orientation as explained in Fig 4-b. The results also show that the

rotational effect decreases with an increasing Reynolds number (or decreasing rotation number).

Figure 7 shows the Nusselt number ratio for case (c). Case (c) is generated from case (b) by changing the parallel 45° V-shaped ribs in the first pass of case (b) to inverted 45° V-shaped ribs. The stationary results show that the first pass Nusselt number ratio behaves differently from that in case (b) at lower Reynolds numbers. This is because, as shown in Fig. 4-c, the inverted 45° V-shaped rib vortices tend to interact with each other and reduce the surface heat transfer enhancement. However, the effect diminishes at higher Reynolds numbers. The second pass behavior is similar to case (b) due to the same V-shaped orientation. The results also show that the rotation effect decreases with an increasing Reynolds number (or decreasing rotation number).

Figure 8 shows the Nusselt Number ratio for case (d). In case (d), as explained in Figure 4-d, the Nusselt number ratio distribution in the first pass case (d) is similar to the case (b) first pass because they both have parallel 45° V-shaped ribs. In the second pass of case (d), inverted 45° V-shaped ribs were placed. The Nusselt number distribution shows lower values compared to the case (b) or case (c) second passes, which have parallel 45° V-shaped ribs.

Figure 9 shows the Nusselt number distribution for case (e). Both passes have inverted 45° V-shaped ribs as explained in Figure 4-e. The Nusselt number distribution in the first pass is similar to the Nusselt number distribution in the first pass of case (c) and the Nusselt number distribution in the second pass is similar to the Nusselt number distribution in the second pass of case (d).

Crossed 45° V-shaped Rib Case

Figure 10 shows the Nusselt number distribution for the crossed rib case as can be seen in Figure 4-f. The results show that the non-rotating Nusselt number ratios are unlike the parallel rib case results. Both leading and trailing surfaces show different Nusselt number ratio distributions in each pass. This variation is due to the different orientations of the 45° V-shaped ribs that are placed on the leading and trailing surfaces Their Nusselt number ratios are lower than those of all previous parallel and inverted 45° V-shaped rib cases, as explained in Fig. 4-f.

Channel-Averaged Nusselt Number Ratio

Figure 11 presents the averaged Nusselt number ratio distribution for smooth and five different arrangements of the 45° V-shaped ribs in the two pass rectangular channels for the stationary case. The Nusselt number ratios in Figure 11 are the average values of the leading and trailing surfaces for all cases. The results show that the ribbed surfaces provide higher Nusselt number ratios in both passes compared to the smooth surfaces. In the first pass, case (b) and case (d) show higher averaged Nusselt number ratios compared to case (c) and case (e). This is because the 45° V-shaped rib induces a stronger secondary flow than the inverted 45° V-shaped rib. In the second pass, case (b) and case (c) show better averaged Nusselt number ratios compared to other cases due to the same reason. The crossed V-shaped rib case (f) results show lower averaged Nusselt number ratios compared to the parallel V-shaped rib cases. The crossed V-shaped ribs induce a pair of counter rotating vortices, while the parallel V-shaped ribs induce two pairs of counter rotating vortices, which promote more mixing with the core flow.

Figure 12 shows the channel averaged Nusselt number ratio with respect to Reynolds number for ω=550 rpm on each pass leading and trailing surfaces for β=90°. All Nusselt number ratio results exhibit a decreasing trend with increasing Reynolds number. Ribbed cases provide better Nusselt number ratio enhancement compared to the smooth case. In general, Nusselt number ratios in the first pass leading surfaces are about the same for all V-shaped cases. However, Nusselt number ratios for the V-shaped rib cases (b) and (d) are higher than other cases in the first pass trailing surfaces. A noticeable variation can be seen in the second pass due to the 180° turn effect. Cases (b) and (c) of the V-shaped rib show greater values of Nusselt number ratios than cases (d), (e), and (f) (the inverted V-shaped rib and crossed rib).

Fig. 13 shows the channel averaged Nusselt number ratio on the leading and trailing surfaces for β=135°. The results are similar to β=90° in trend except that the Nusselt number ratios on the first pass trailing and the second pass leading are lower because of the oblique angle of the flow impinging on the surfaces.

CONCLUSIONS

The influences of 45° V-shaped rib arrangements and channel orientation on the leading and trailing Nusselt number ratios in a two-pass rectangular channel have been reported for rotation numbers from 0 to 0.21 and Reynolds numbers from 5000 to 40000. The findings are:

1. The general trend of the rotation effect shows an increase in the Nusselt number ratio in the first pass trailing surface and second pass leading surface, while the opposite situation can be observed in the first pass leading surface and second pass trailing surface. This is due to the Coriolis and buoyancy forces, which are generated by rotation.

However, the differences between the Nusselt number distributions on the second pass leading and trailing surfaces are smaller than that of the first pass due to the opposite effects of the Coriolis and buoyancy forces.

2. The effects of the Coriolis force and cross-stream flow are reduced as the channel orientation changes from $\beta=90°$ to $\beta=135°$. Thus, the Nusselt number ratios for the $\beta=135°$ first pass trailing and second pass leading surfaces decrease when compared to their corresponding Nusselt number ratios for the $\beta=90°$ orientation. The Nusselt number ratios for $\beta=135°$ first pass leading and second pass trailing surfaces increase when compared to their corresponding Nusselt number for $\beta=90°$.

3. Both orientations of the 45° V-shaped rib induce two pairs of counter rotating vortices, but the inverted 45° V-shaped rib vortices tend to interact with each other. Therefore, the 45° V-shaped rib results in better heat transfer enhancement than the inverted 45° V-shaped rib for both non-rotating and rotating conditions.

4. The parallel 45° V-shaped rib arrangements provide a higher heat transfer enhancement compared to the crossed 45° V-shaped rib arrangement for both rotating and non-rotating conditions. The crossed rib arrangement shows less rotational effect compared to the parallel rib cases. This is because the parallel 45° V-shaped rib develops two pair of counter rotating vortices of secondary flows, while the crossed 45° V-shaped rib develops only one single pair of counter rotating vortices.

5. For all cases studied here, results show relatively low heat transfer enhancement in the 180° turn region. This is because the vortices induced by the V-

shaped rib are suppressed by the 180° turn and there is no 45° V-shaped rib placed at the middle of the 180° turn.

6. For all cases studied here, results show that the heat transfer enhancement decreases with increasing Reynolds number.

ACKNOWLEDGMENTS

The leading author, Luai AL-Hadhrami, received a fellowship from King Fahd University of Petroleum and Minerals, Saudi Arabia, for his Ph.D. study at Texas A&M University. This work was supported by the DOE Advanced Gas Turbine Systems Research (AGTSR) program through project number SR-094. The support of the above institutions is greatly appreciated.

NOMENCLATURE

D	hydraulic diameter (m)
e	rib height (m)
h	heat transfer coefficient (W/m^2K)
k	thermal conductivity of coolant (W/mK)
Nu	local Nusselt number, hD/k
Nu_o	Nusselt number in fully-developed turbulent non-rotating tube flow with smooth wall
P	rib pitch (m)
Pr	Prandtl number
q_{net}	net heat at wall (W)
A	surface area of the copper plate (m^2)

R	radial distance from axis of rotation to heated test section's mean radius
Re	Reynolds number, $\rho VD/\mu$
R_o	rotation number, $\Omega D/V$
T_{bx}	local coolant temperature (^oC)
T_{bi}	coolant temperature at inlet (^oC)
T_w	wall temperature (^oC)
V	bulk velocity in streamwise direction (m/s)
β	angle of channel orientation with respect to the axis of rotation
Ω	rotational speed (rad/s)
ω	rotational speed (rpm)
α	rib angle
μ	dynamic viscosity of coolant (Pa-s)
ρ	density of coolant (kg/m^3)
$\Delta\rho / \rho$	inlet coolant-to-wall density ratio, $(T_w - T_{bi})/T_w$

REFERENCES

[1] Metzger, D. E. and Sahm, M. K., 1986, "Heat Transfer around Sharp 180° Turns in Smooth Rectangular Channels," *ASME Journal of heat transfer*, vol. 113, pp. 500-506.

[2] Fan, C.S. and Metzger, D. E., 1987, "Effects of Channel Aspect Ratio on Heat Transfer in Rectangular Passage Sharp 180° Turn," ASME Paper No. 87-GT-113.

[3] Han, J.C., and Park, J.S., 1988, "Developing Heat Transfer in Rectangular Channels With Rib Turbulators," *International Journal of Heat and Mass Transfer*, Vol. 31, No. 1, pp. 183-195.

[4] Han, J.C., Zhang, Y. M. and Lee, C.P., 1991, "Augmented Heat Transfer in Square Channels With Parallel, Crossed, and V-Shaped Angled Ribs," *ASME Journal of Heat Transfer*, Vol. 113, pp. 590-596.

[5] Taslim, M.E., Li, T., and Kercher, D.M., 1994, "Experimental Heat Transfer and Friction in Channels Roughened with Angled V Shaped and Discrete Ribs on Two Opposite Walls," ASME Paper 94-GT-163.

[6] Ekkad, S.V., and Han, J.C., 1997, "Detailed Heat Transfer Distribution in Two-Pass Square Channels With Rib Turbulators," *International Journal of Heat and Mass Transfer*, Vol. 40, No. 11, pp. 2525-2537.

[7] Kiml, R., Mochizuki, ,S., and Murata, A., 2001, "Heat Transfer Enhancment Mechanism in a Rectangular Passage with V- and Λ-Shaped Ribs," *Journal of Flow Visualization and Image Processing*, Vol. 8, pp. 51-68.

[8] Wagner, J.H., Johnson, B.V., and Hajek, T.J., 1991a, " Heat Transfer in Rotating Passage With Smooth Walls and Radial Outward Flow," *Journal of Turbomachinery*, Vol. 113, pp. 42-51.

[9] Wagner, J.H., Johnson, B.V., and Kooper, F.C., 1991b, " Heat Transfer in Rotating Serpentine Passage With Smooth Walls," *Journal of Turbomachinery*, Vol. 113, No. 3, pp. 321-330.

[10] Johnson, B.V., Wagner, J.H., Steuber, G.D., and Yeh, F.C., 1994a, " Heat Transfer in Rotating Serpentine Passage With Trips Skewed to the Flow," *Journal of Turbomachinery*, Vol. 116, pp. 113-123.

[11] Johnson, B.V., Wagner, J.H., Steuber, G.D., and Yeh, F.C., 1994b, " Heat Transfer in Rotating Serpentine Passage With Selected Model Orientations for Smooth or Skewed Trip Walls," *ASME Journal of Turbomachinery*, Vol. 116, pp. 738-744.

[12] Han, J.C., Zhang, Y.M., and Kalkuehler, K., 1993, "Uneven Wall Temperature Effect on Local Heat Transfer in a Rotating Two-Pass Square Channel With Smooth Walls," *ASME Journal of Heat Transfer*, Vol. 115, No. 4, pp. 912-920.

[13] Zhang, Y.M., Han, J.C., Parsons, J.A., and Lee, C.P., 1995, " Surface Heating Effect on Local Heat Transfer in a Rotating Two- Pass Square Channel With 60° Angled Rib Turbulators," *ASME Journal of Turbomachinery*, Vol. 117, pp. 272-280.

[14] Parsons, J.A., Han, J.C., and Zhang, Y.M., 1994, " Wall Heating Effect on Local Heat Transfer in a Rotating Two-Pass Square Channel With 90° Rib Turbulators," *International Journal of Heat and Mass Transfer*, Vol. 37, No. 9, pp. 1411-1420.

[15] Parsons, J.A., Han, J.C., and Zhang, Y.M., 1995, "Effects of Model Orientation and Wall Heating Condition on Local Heat Transfer in a Rotating Two-Pass Square Channel With 90° Rib Turbulators," *International Journal of Heat and Mass Transfer*, Vol. 38, No. 7, pp. 1151-1159.

[16] Dutta, S., and Han, J.C., 1996, "Local Heat Transfer in Rotating Smooth and Ribbed Two-Pass Square Channels With Three Channel Orientations," *ASME Journal of Heat Transfer*, Vol. 118, pp. 578-584.

[17] Dutta, S., and Han, J.C., and Lee, C.P., 1996, "Local Heat Transfer in a Rotating Two-Pass Ribbed Triangular Duct With Two Model Orientations," *International Journal of Heat and Mass Transfer*, Vol. 39, pp. 707-715.

[18] Taslim, M.E., Rahman, A. and Spring, S.D., 1991a, "An Experimental Investigation of Heat Transfer Coefficients in a Spanwise Rotating Channel With Two Opposite Rib-Roughened Walls," *ASME Journal of Turbomachinery*, Vol. 113, pp. 75-82.

[19] Taslim, M.E., Bondi, L.A., and Kercher, D.M., 1991b, "An Experimental Investigation of Heat Transfer in an Orthogonally Rotating Channel Roughened With 45º Criss-Cross Ribs on Two Opposite Walls," *ASME Journal of Turbomachinery*, Vol. 113, pp. 346-353.

[20] Prabhu, S.V., and Vedula, R.P., 1997, "Pressure Drop Distribution in a Rotating Rectangular Channel With One Ribbed Surface," *ASME Paper No. 97-AA-118*.

[21] Park, C.W., Yoon, C., and Lau, S.C., 2002, "Heat (Mass) Transfer in a Diagonally Oriented Rotating Two-Pass Channel with Rib-Roughened Walls," *ASME Journal of Heat Transfer*, Vol. 122, pp. 208-211.

[22] Azad, GM S., Uddin, M. J., Han, J. C., Moon, H. K., and Glezer, B., 2001, "Heat Transfer in Two-Pass Rectangular Rotating Channels with 45° Parallel and Crossed rib Turbulators" *ASME Journal of Turbomachinery*, Vol. 124, pp. 251-259.

[23] Han, J. C., Dutta, S., and Ekkad, S. V., 2000, "*Gas Turbine Heat Transfer and Cooling Technology*," Taylor & Francis, Inc., New York.

[24] Kline, S.J., and McClintock, F.A., 1953, "Describing Uncertainties in Single-Sample Experiments," *Mechanical Engineering*, Vol. 75, pp. 3-8.

[25] Al-Qahtani, M., Jang, Y., Chen, H., and Han, J.C., 2001, “Prediction of Flow and Heat Transfer in Rotating Two-Pass Rectangular Channels with 45° Rib Turbulators,” *ASME Journal of Turbomachinery*, Vol. 124, pp. 242-250.

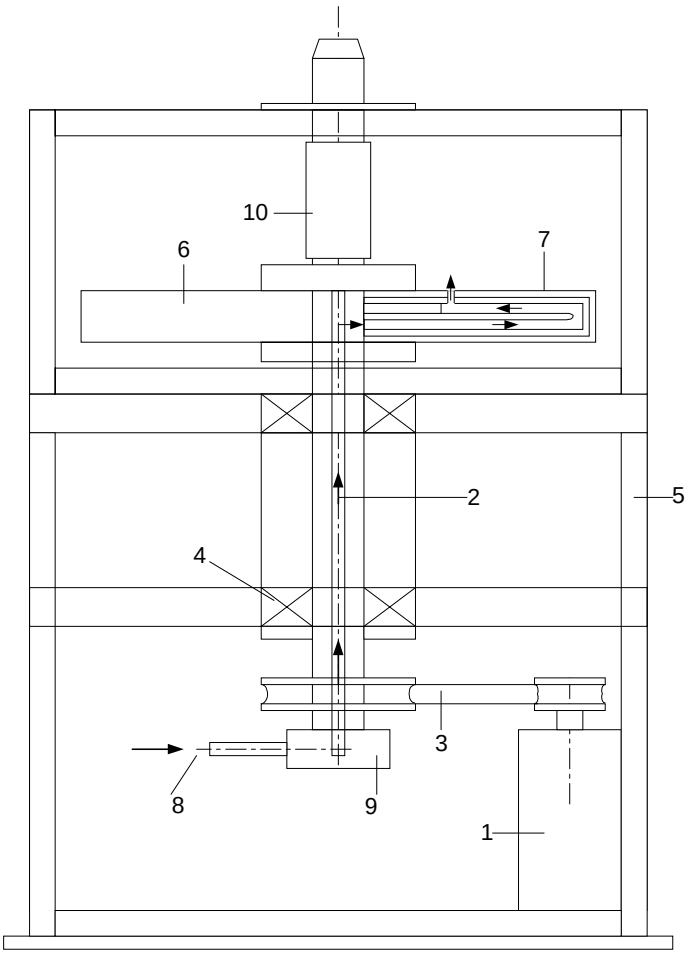

1. Electircal Motor with Controller
2. Rotating Shaft
3. Belt Drive Pulley System
4. Bearing Support System
5. Steel Table
6. Rotating Arm
7. Test Section
8. Compressor Air
9. Rotary Seal
10. Slip Ring

Fig. 1 Schematic of the Rotating Test Rig

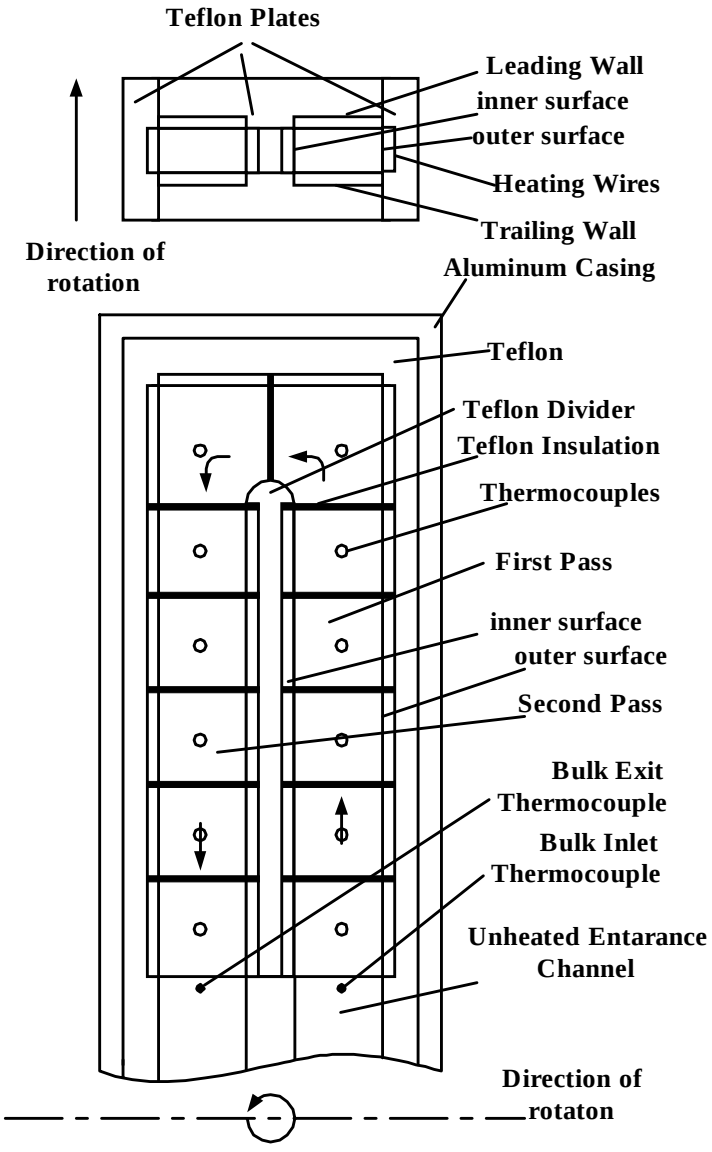

Fig. 2 Cross sectional view of the two-pass rectangular test section.

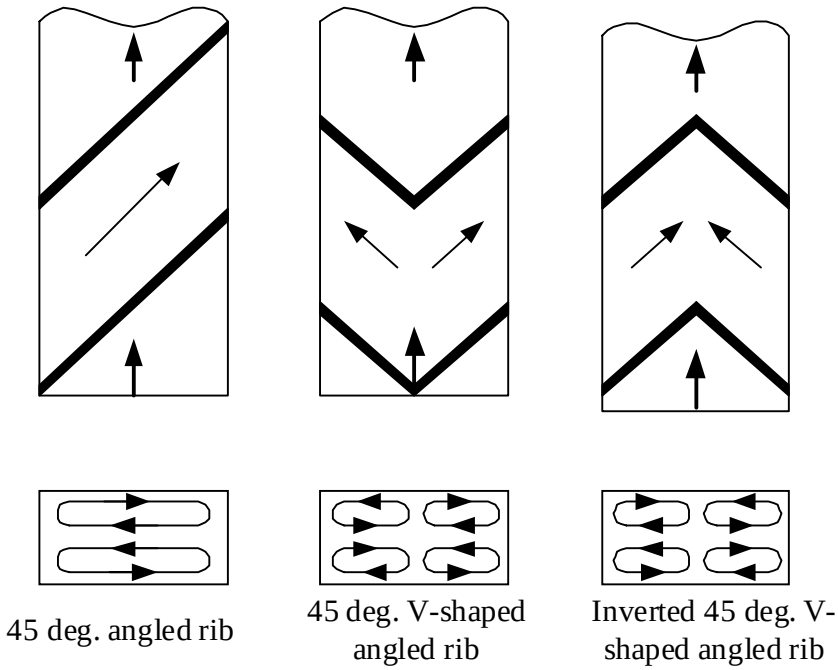

Fig. 3 Conceptual view of secondary flow vortices induced by 45° angled ribs and 45° V-shaped ribs.

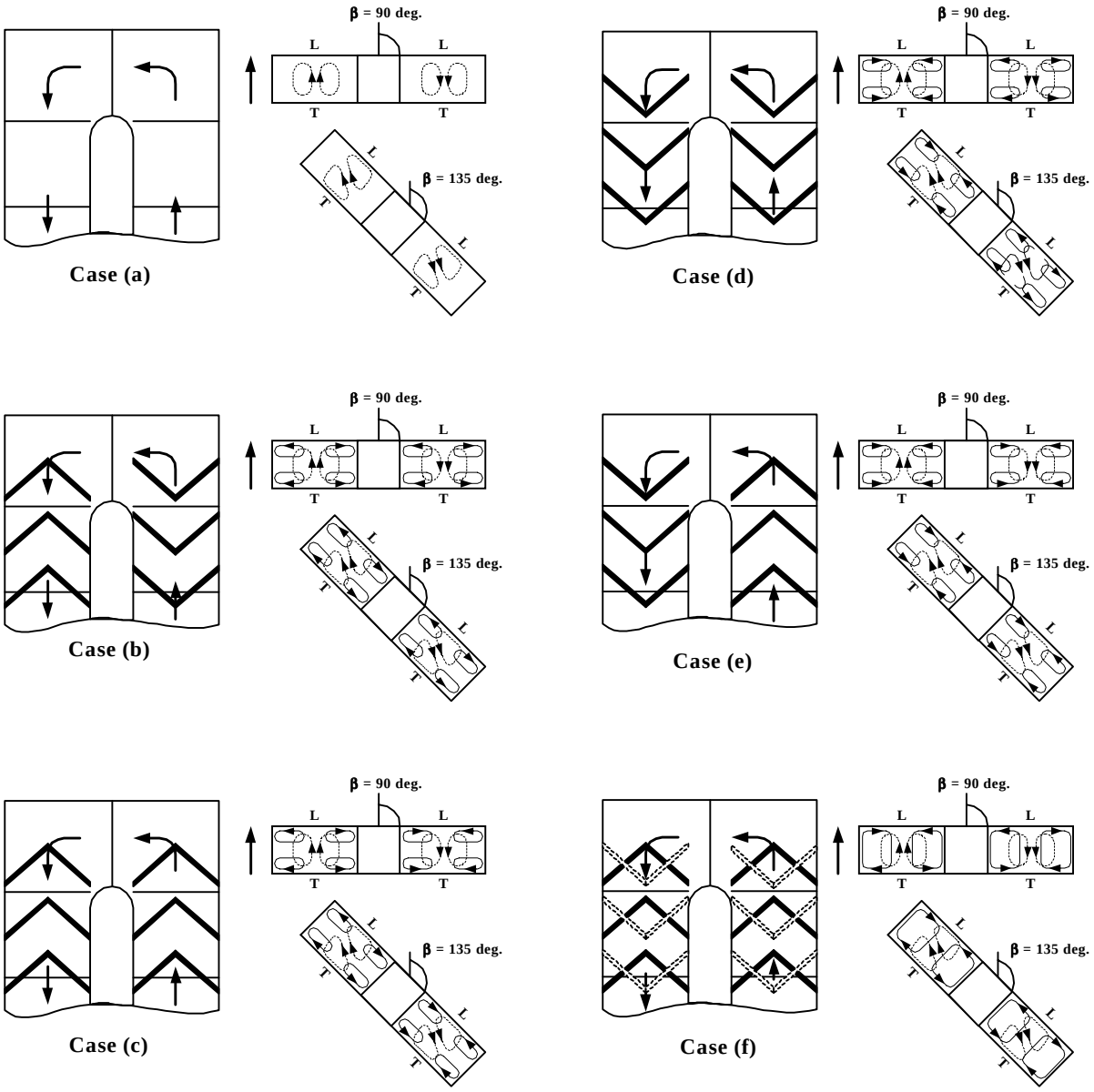

Fig. 4 Conceptual view of the secondary flow vortices induced by rotation, ribs, and channel orientation (dash line: rotation-induced vortices, solid line: rib-induced vortices).

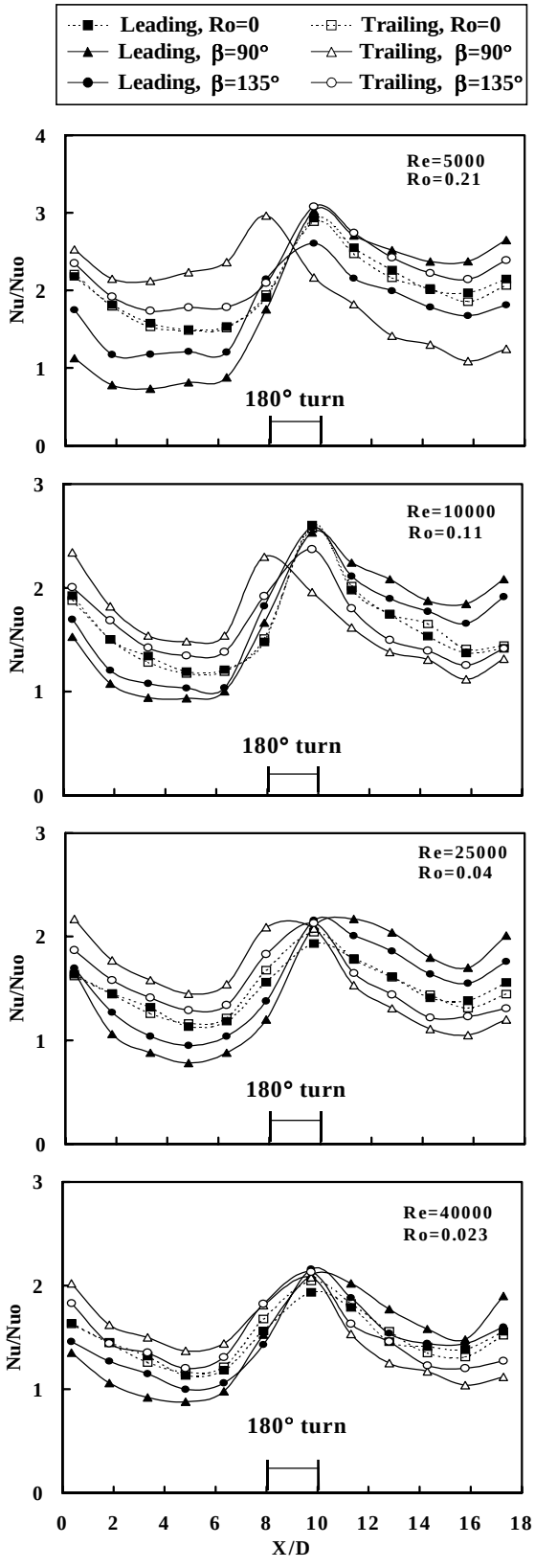

Fig. 5 Nusselt number ratio distribution for case (a)

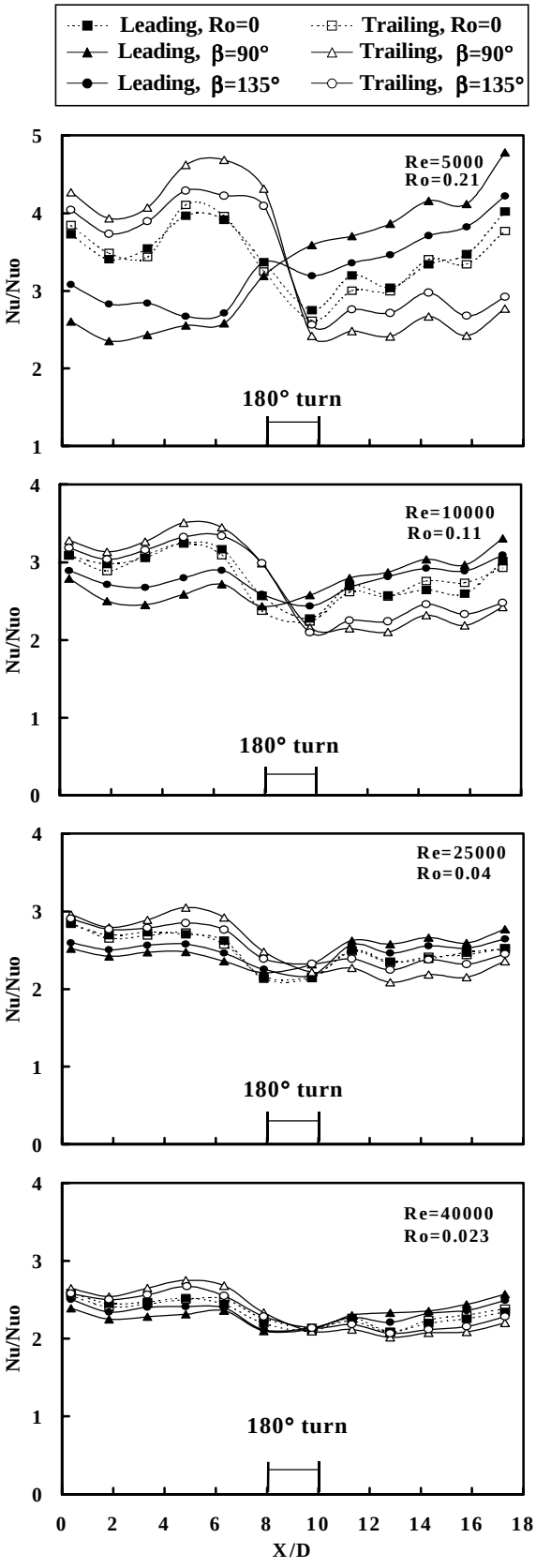

Fig. 6 Nusselt number ratio distribution for case (b)

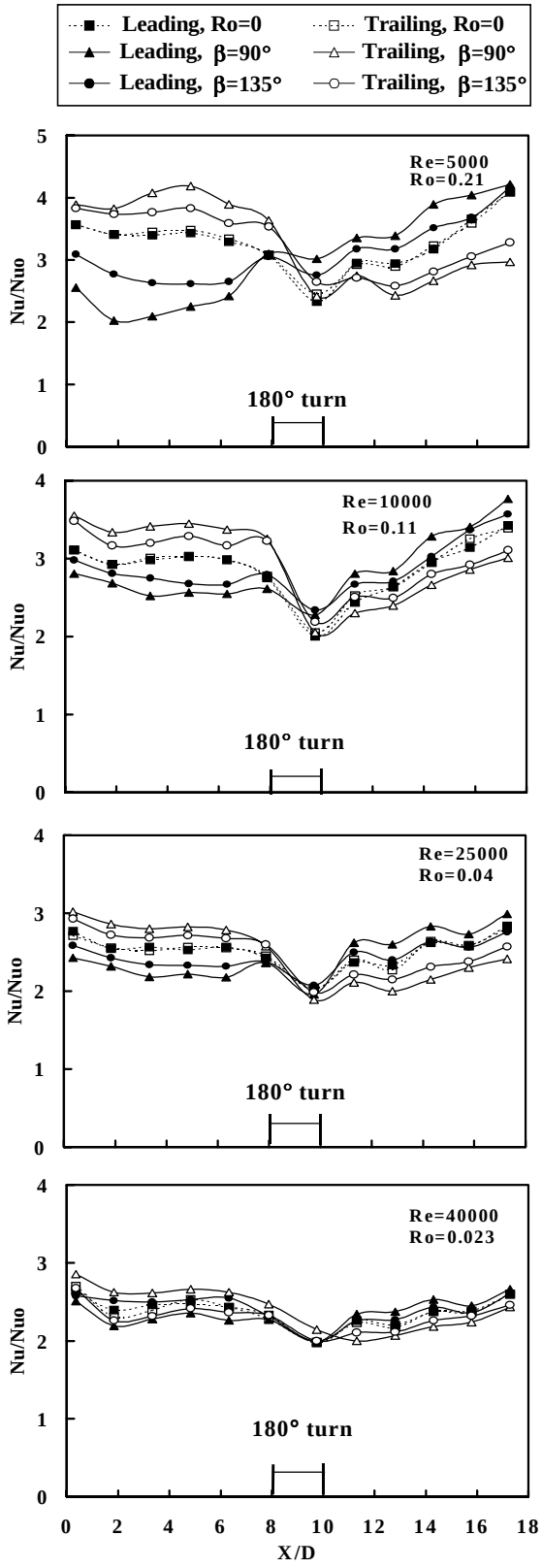

Fig. 7 Nusselt number distribution for case (c)

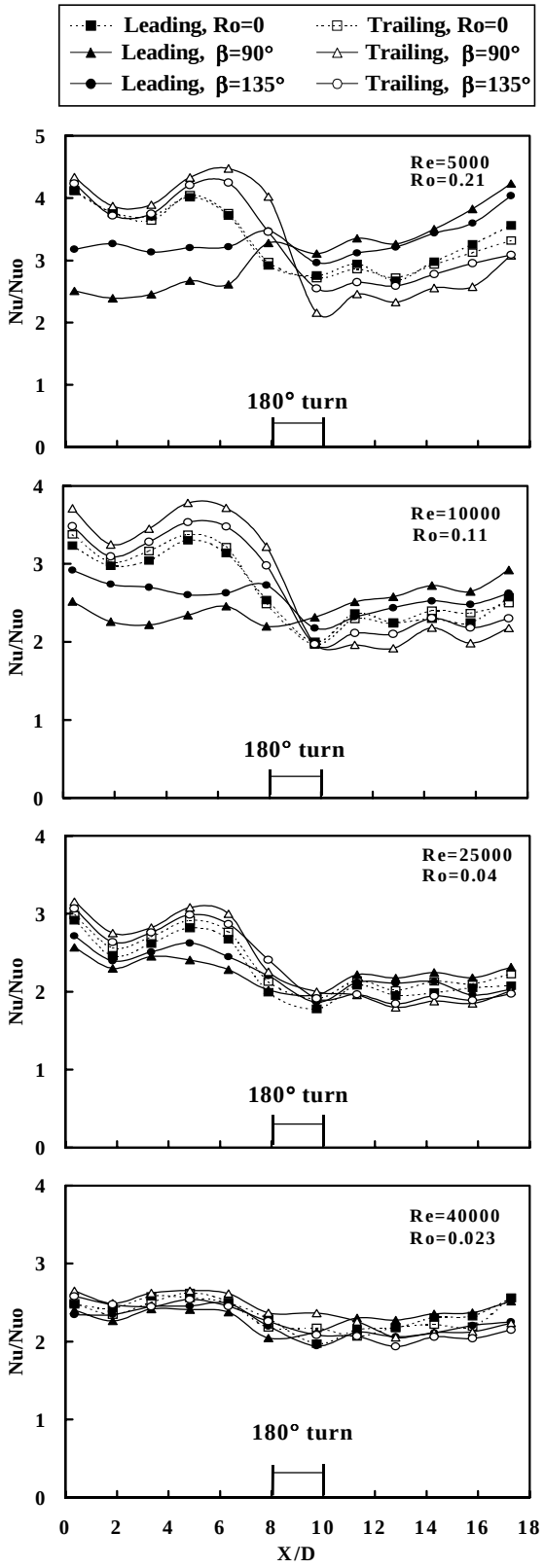

Fig. 8 Nusselt number distribution for case (d)

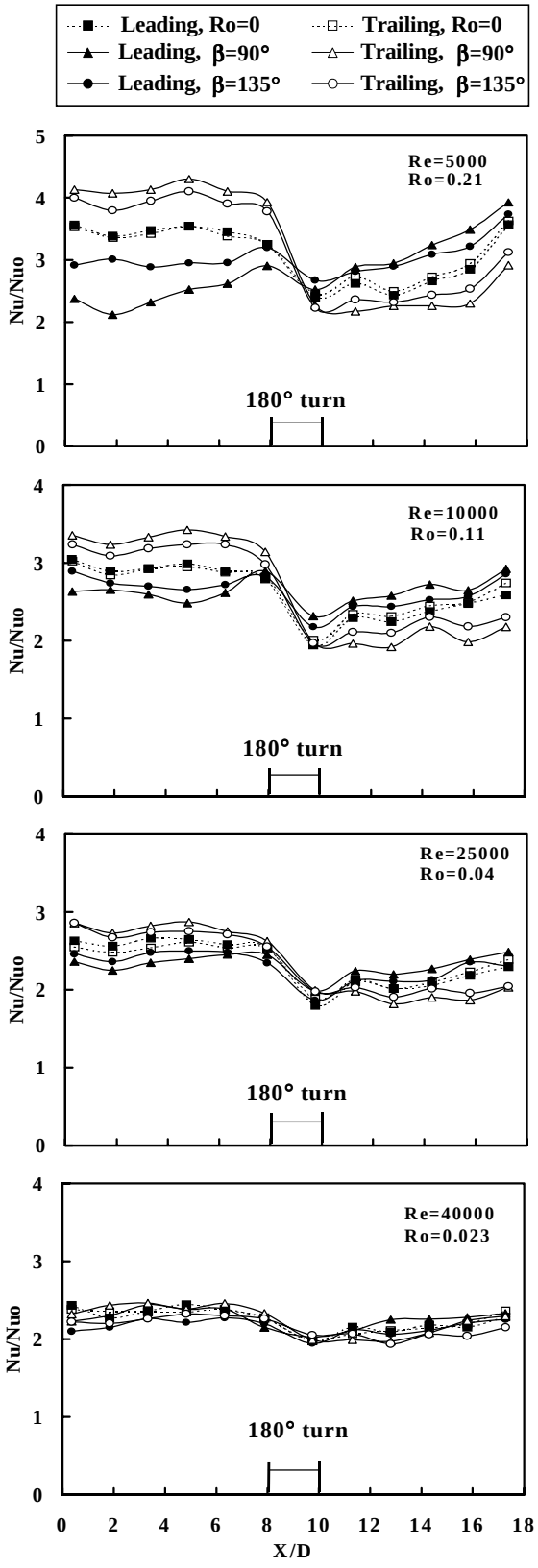

Fig. 9 Nusselt number distribution for case (e)

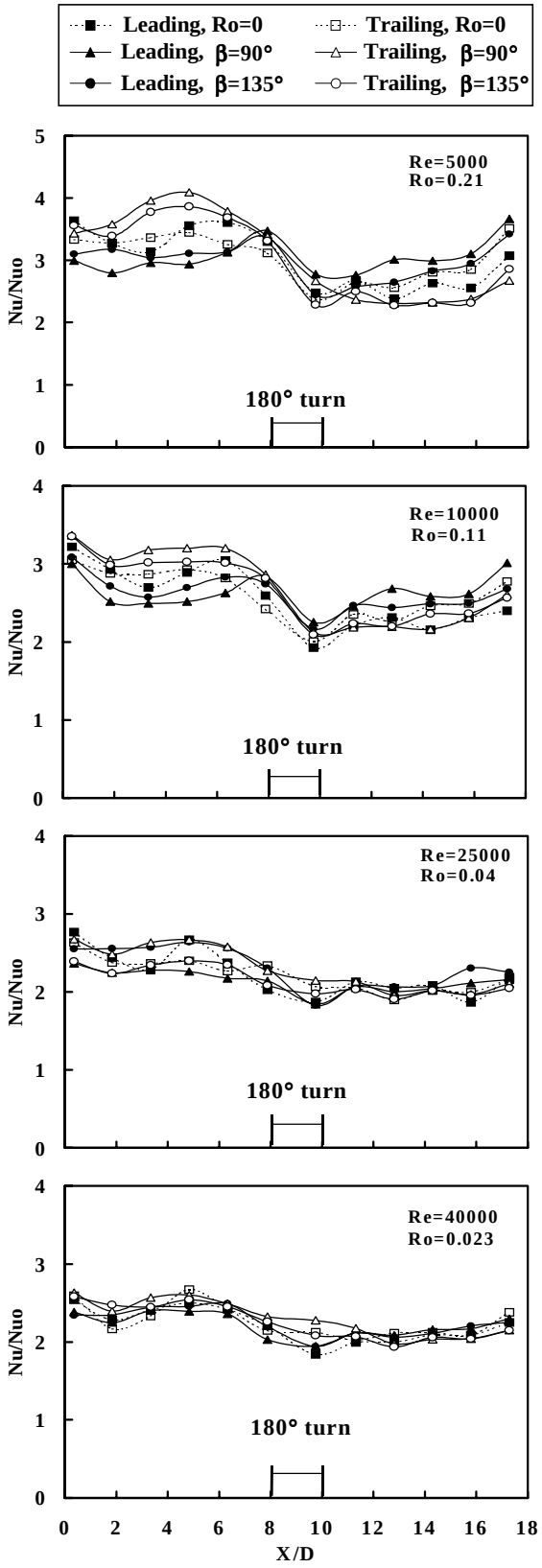

Fig. 10 Nusselt number distribution for case (f)

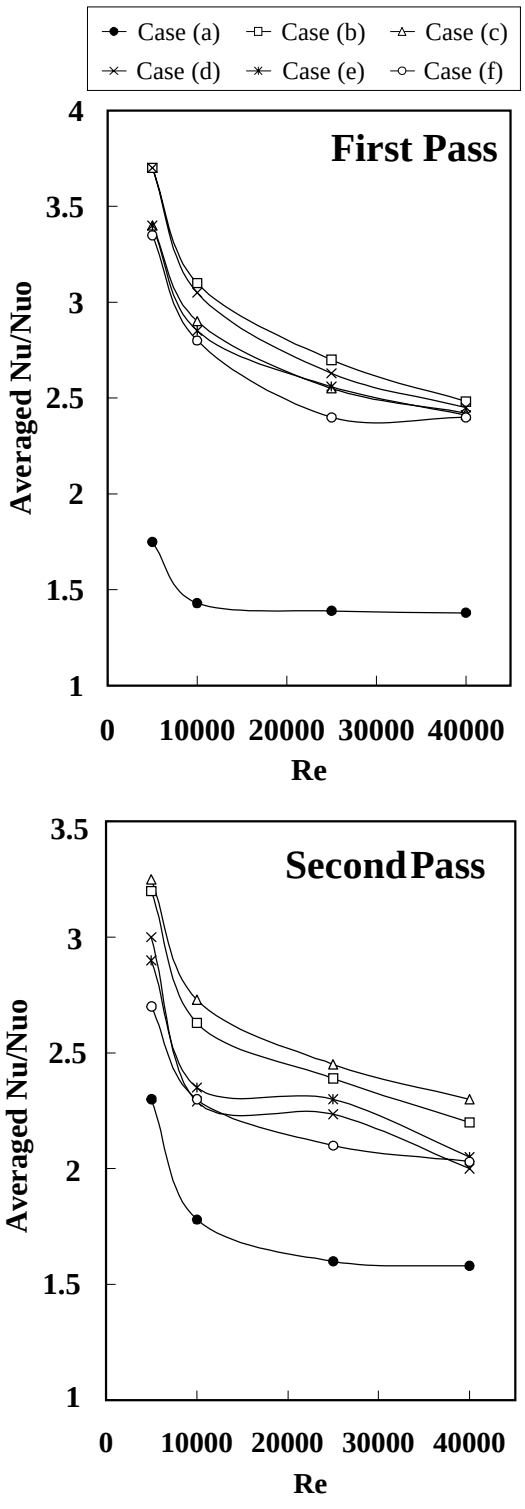

Fig. 11 averaged Nusselt number distribution for non-rotating (ω=0) cases.

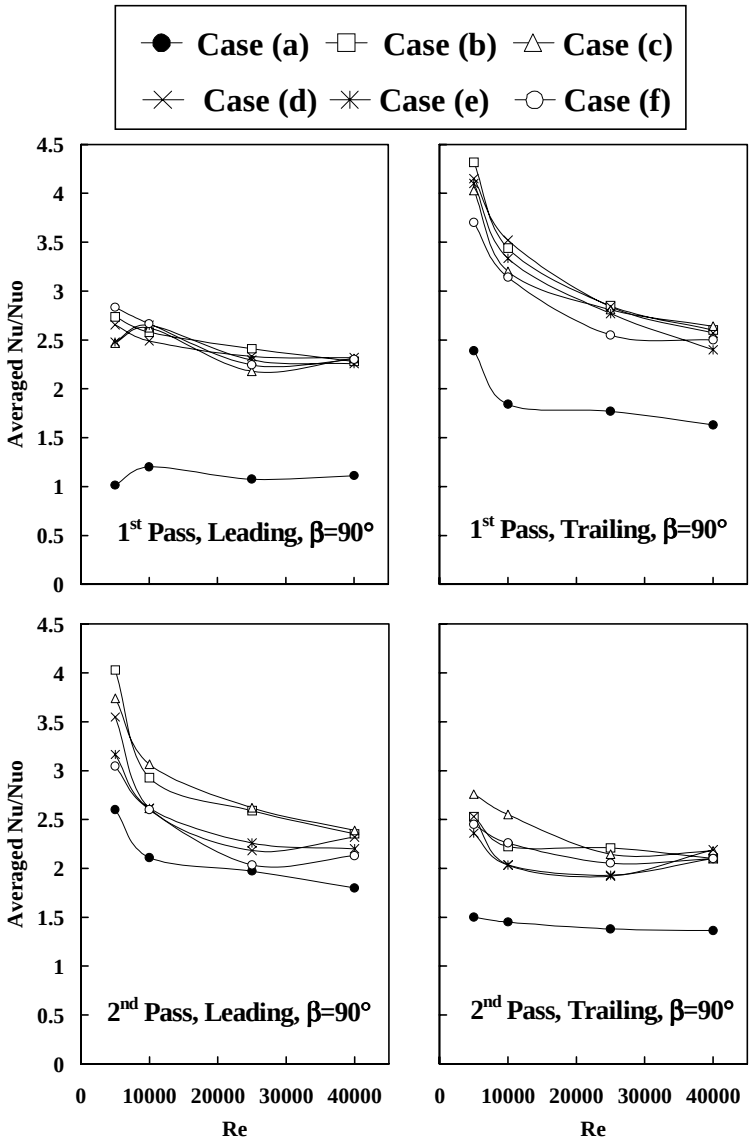

Fig. 12 averaged Nusselt number distribution for leading and trailing surfaces with rotation (ω=550 rpm) for β=90°

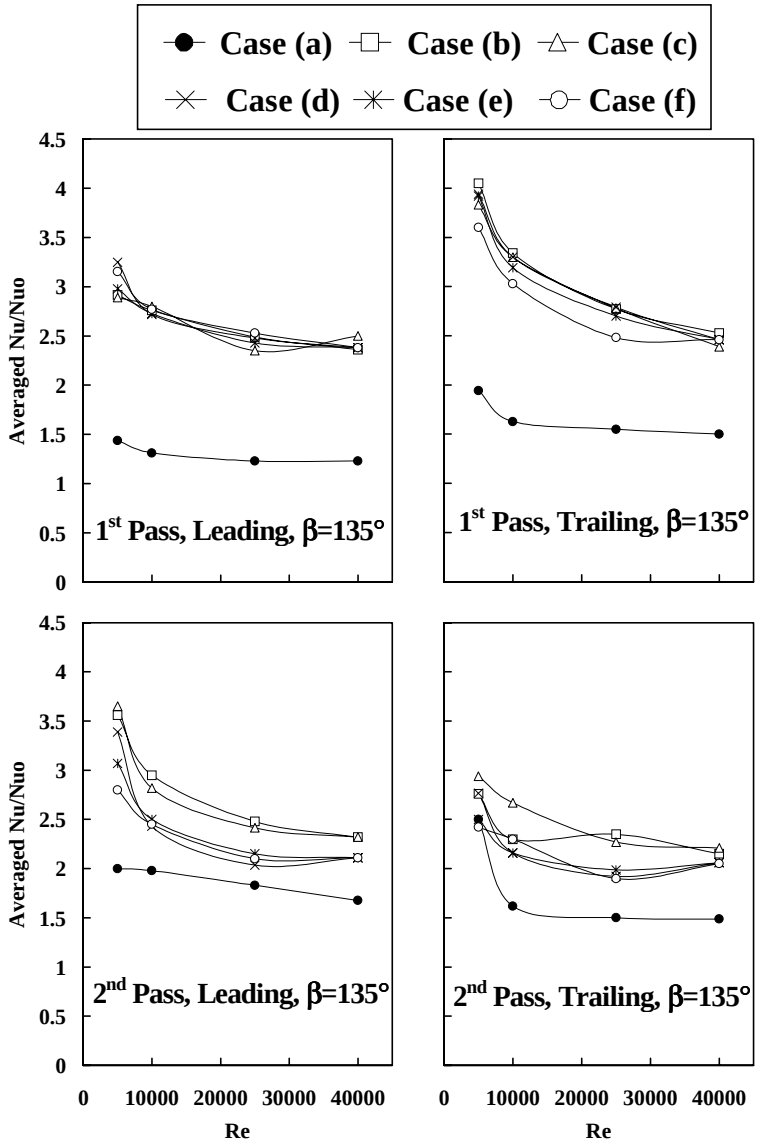

Fig. 13 averaged Nusselt number distribution for leading and trailing surfaces with rotation (ω=550 rpm) for β=135°.

PART I-B:

HEAT TRANSFER IN TWO-PASS ROTATING RECTANGULAR CHANNELS (AR=2) WITH THREE DIFFERENT ORIENTATIONS OF BROKEN 45° V-SHAPED RIB TURBULATORS

Abstract

An experimental study was made to obtain heat transfer data for a two-pass rectangular channel (aspect ratio=2:1) with smooth and ribbed surfaces for two channel orientations (90º and 135º with respect to the plane of rotation). The broken V-shaped ribs are placed on the leading and trailing surfaces. Three different arrangements of broken 45° V-shaped ribs are studied. The Reynolds number and rotation number ranges are 5000-40000, and 0.0-0.21, respectively. The rib height to hydraulic diameter ratio (e/D) is 0.094; the rib pitch-to-height ratio (P/e) is 10; and the inlet coolant-to-wall density ratio ($\Delta\rho/\rho$) is maintained at 0.115 for all surfaces in the channel. The results show that the rotation- induced secondary flow enhances the heat transfer of the trailing surface first pass and leading surface second pass. However, the first pass leading and the second pass trailing surfaces show a decrease in heat transfer with rotation. The results show that the broken 45º V-shaped rib arrangements produce better heat transfer augmentation than 45° V-shaped ribs, and a 90º channel orientation produces greater rotating effect on heat transfer than a 135º orientation.

Introduction

To achieve high thermal efficiency and a low cost gas turbine engine, the turbine inlet gas temperature should be increased. However, the penalty is a high thermal load, which exceeds the durability of the turbine components. Therefore, improved cooling techniques such as film cooling and internal cooling are applied to turbine blade. Internal cooling is achieved by circulating low enthalpy air in multi-pass flow channels inside the blade structure. To increase the effectiveness of the internal cooling, the internal surfaces usually are roughened by angled ribs to trip the boundary layer and increase the turbulence, which enhances the heat transfer. As the turbine blade rotates, Coriolis and buoyancy forces appear and cause different heat transfer behavior from the leading and trailing surfaces. The Coriolis force produces secondary flow in planes perpendicular to the main flow direction, which encourages the migration of core region flow toward the trailing surface in the first pass and the leading surface in the second pass.

Over the past few decades numerous studies have been made experimentally on the flow field and heat transfer in the internal coolant passage of a gas turbine rotor blade. Metzger et al. [1] studied forced convection in a two-pass smooth rectangular channel by varying the divider location and the gap at the 180^{o} turn. Fan et al. [2] extended the Metzger et al. [1] work by varying the channel width and concluded that increasing the channel aspect ratio resulted in smaller azimuthal heat transfer variations and increased overall channel heat transfer. Han and Park [3] performed experimental studies on heat transfer characteristics in a non-rotating rib-roughened rectangular channel. Han et al. [4] studied the effect of the rib angle orientation on heat transfer distributions and pressure drop in a non-rotating square channel with two opposite in-line ribbed walls. They found

that the 60º and 45º V-shaped ribs performed better than the 60º and 45º parallel ribs and, subsequently, better than the 60º and 45º crossed ribs and the 90º rib. The V-shaped ribs produced the highest heat transfer augmentation, while the crossed rib had the lowest heat transfer enhancement. Ekkad and Han [5] performed a detailed study on heat transfer distributions in a non-rotating square ribbed channel using a liquid crystal technique. The results show that the 60°, V-shaped ribbed channel produced more heat transfer enhancement than 60° and 90° angled ribbed channels. Wagner et al. [6, 7] conducted a detailed experimental study to determine the effects of rotation (buoyancy and Coriolis forces) on the local heat transfer of a multi-pass square channel with smooth walls. They concluded that in the first pass of the coolant passage, rotation created a thinner boundary layer on the trailing surface and a thicker boundary layer on the leading surface; but in the second pass, the performance was opposite the first pass. The leading surface Nusselt number ratios in the second pass were higher than the trailing surface Nusselt number ratios because of the reversal of the Coriolis force direction. Johnson et al. [8] performed a systematic investigation of the effects of buoyancy and Coriolis forces on the heat transfer coefficient distribution of a four-pass square channel with 45° ribs angled to the flow. Han et al. [9] investigated an uneven wall temperature effect on local heat transfer in a rotating two-pass square channel with smooth walls. Zhang et al. [10] analyzed the heating condition effects in a two pass square channel with 60° angled rib turbulators with rotation. They suggested that an uneven wall temperature had a significant impact on the local heat transfer coefficients. Parsons et al. [11] presented the wall-heating effect on local heat transfer in a rotating two-pass square channel with orthogonal ribs. Johnson et al. [12] and Parsons et al. [13] studied the effects of channel orientation and wall

heating condition on the local heat transfer coefficient in a rotating two-pass square channel with ribbed walls. They found that the effects of the Coriolis force and cross-stream flow were reduced as the channel orientation changed from a normal (β=90°) to an angled orientation (β=135°). Dutta and Han [14] also investigated the local heat transfer coefficients in rotating smooth and ribbed two-pass square channels with three channel orientations. Dutta et al. [15] presented experimental heat transfer results for turbulent flows through a rotating two-pass rib-roughened triangular channel, with two channel orientations with respect to the direction of rotation. Taslim et al. [16, 17] studied the heat transfer characteristics in rib-roughened square and rectangular orthogonal rotating channels. They used a liquid crystal technique to study the effect of rotation on heat transfer distributions on the walls. The first part of their study set the leading and trailing walls of the test channel as roughened with staggered transverse ribs, while the second part set the opposite as rib-roughened at 45º with respect to the main flow in a criss-cross arrangement. They found that rotational effects were more pronounced in rib-roughened channels, with a higher channel aspect ratio and a lower rib blockage ratio. They investigated heat transfer effects in an orthogonally rotating single pass channel. However, they did not consider a two-pass channel and the effect of channel orientation. Prabhu and Vedula [18] investigated the pressure drop distribution in a rotating rectangular channel with transverse ribs on one wall. They conducted experiments for a rotation number up to 0.21, pitch-to-height ratios of 3, 5, 7.5, and 10, and a rib height-to-hydraulic diameter ratio of 0.15. They found that a rib array with a pitch-to-height ratio of 5 caused the largest pressure drop. Azad et al. [19] experimentally investgated the heat transfer distribution in two-pass rectangular channels (AR=2:1) connected with a 180°

turn. The results showed that the roughened surfaces exhibit better heat transfer distribution than the smooth surfaces. Also, the results showed that parallel 45° angled ribs produced higher heat transfer distribution than the crossed 45° angle rib case. Dutta and Han [20] and Han et al. [21] provided a detailed review on flow and heat transfer characteristics in rotating channels for turbine blade internal cooling applications.

Following the above-mentioned research, few papers can be found in the open literature studied the rectangular cross section channel especially with rotation condition. Hence, the first aim was to study two pass rectangular channels (AR=2:1) that are connected with a sharp 180° turn. The second motivation was to find different rib configurations that trip the boundary layer and promote more turbulence inside the two-pass rectangular channels. However, it was found from a previous study by Dutta et al. [14] that the 45° broken V-shaped ribs show higher heat transfer performance in two-pass square rotating channel compared to other rib configurations (45° angled ribs or transverse 90° ribs). Thus, we have chosen 45° broken V-shaped ribs to be placed on the principle surfaces in the two-pass rotating rectangular channels since they have shown a potential for higher heat transfer performance. A comprehensive study was conducted to cover three different arrangements of 45° broken V-shaped ribs and a comparison with 45° V-shaped ribs and inverted 45° V-shaped ribs cases. Moreover, the effect of the channel orientation with respect to plane of rotation was investigated for two positions β =90° and β =135°. Such experimental data is not available in the open literature. Our research shows the combined effect of the 45° broken V-shaped rib induced secondary flow and rotation induced secondary flow on the heat transfer distribution in the two-pass rectangular cross-sectional channels.

Experimental set up

Figure 1 shows the schematic of the experimental test rig. Compressed air goes through a filter and an orifice meter, and then passes through a rotary seal and a hollow-rotating shaft to feed the test section. The test section is mounted in a horizontal plane. Air travels outward in the first pass and inward in the second pass, and then exhausts into the atmosphere. Slip rings transfer thermocouple outputs to the data logger and power input from transformers to strip heaters, which are fixed under the copper plates. An electric motor with an adjustable frequency controller rotates the test section. A digital photo tachometer measures the rotational speed of the rotating shaft.

Figure 2 shows a cross sectional view of the test section. The test section has two passes. Each pass is 12.7 mm by 25.4 mm in cross section. The first pass starts with an unheated teflon entrance channel to establish a hydro-dynamically fully developed flow at the entrance to the heated channel. It has twelve (12) hydraulic diameter lengths to achieve the task. The heated channel length-to-hydraulic diameter (*L/D)* ratio is 18, while each pass length-to-hydraulic diameter (*L/D*) ratio is 9, connected by a sharp 180^{o} turn. The flow in the first pass is radially outward and the flow in the second pass in radially inward. The heated section is divided into twelve longitudinal sections, six sections in first pass and six in second pass, to obtain local heat transfer coefficients. Each longitudinal section has four copper plates on four walls (one per wall) of the channel. Each copper plate is surrounded circumferencially by a thin teflon strip that has a 1.59 mm thickness for insulation from neighboring plates. Each copper plate has a single thermocouple that gives the regional surface temperature. The inlet and exit bulk

temperatures are measured by thermocouples. Each surface receives uniform heat flux from an individual transformer to maintain the peak surface temperature around 65^{o} C.

Data reduction

The local heat transfer coefficient is calculated from the local net heat transfer rate per unit surface area to the cooling air, the local wall temperature on each copper plate, and the local bulk mean air temperature as

$$h = q_{net}/[A(T_w - T_{bx})] \qquad (1)$$

Local net heat transfer rate is the electrical power generated from the heater ($q=VI$) minus the heat loss outside the test duct. The heat loss is determined experimentally by supplying electrical power to the test section until a steady state condition is achieved for a no flow (without any airflow) condition. This is done for several different power inputs to obtain a relation between the total heat loss from each surface and the corresponding surface temperature. To place the results on a common basis, the heat transfer area used in equation (1) was always that of a smooth wall. The local wall temperature is obtained from thermocouples that impeded in each copper plate. The bulk mean air temperatures entering and leaving the test section are measured by thermocouples. The local bulk mean temperature (T_{bx}) used in equation (1) is calculated from the linear interpolation between the measured inlet and exit air bulk temperatures. Another way to find the local bulk mean air temperature is determined by marching along the test section and calculating the temperature rise from the local net heat input through each set of four heated surfaces. The difference between the calculated and measured outlet bulk mean temperature is between 1-2 °C in all of the cases.

Local Nusselt number is normalized by the Nusselt number for the fully developed turbulent flow in a smooth stationary circular pipe to reduce the influence of the flow Reynolds number on the heat transfer coefficient. Local Nusselt number normalized by the Dittus-Boelter/McAdams correlation (Rohsenow and Choi 1961) is:

$$Nu/Nuo=(hD/K)/[0.023*Re^{0.8}*Pr^{0.4}] \qquad (2)$$

The Prandtl number(Pr) for air is 0.71. Air properties are taken based on the mean bulk air temperature.

The uncertainty of the local heat transfer coefficient depends on the uncertainties in the local wall and bulk air temperature difference and the net heat input for each test run. The uncertainty increases with the decrease of both the local wall to bulk air temperature difference and the net heat input. Based on the method described by Kline and McClintock [22], the typical uncertainty in the Nusselt number is estimated to be less than 9% for Reynolds number larger than 10000. The maximum uncertainty, however, could be up to 23% for the lowest heat transfer coefficient at the lowest Reynolds number tested (Re=5000).

Result and discussion

Figure 3 shows the 45° angled rib that was divided at the centerline to make the 45° V-shaped rib and the 45° broken V-shaped rib. Figure 3 also shows the conceptual view of secondary flow induced by the 45° angled rib, the 45° V-shaped rib, and the 45° broken V-shaped rib. The 45° angled rib induces a secondary flow that moves parallel to the rib from the left side to the right side and returns back to the left side making a counter rotating vortex (see Al-Qahtaini [23]).

It is conjectured that the 45° V-shaped rib creates two counter rotating vortices. As the fluid approaches the V-shaped rib, it splits into two streams. Each one moves parallel to the rib from the centerline to either the left side or the right side and returns back to the centerline making a counter-rotating vortex. Another observation can be drawn that as the 45° V-shaped rib is half the 45° angled rib , the boundary layer thickness for the fluid that moves parallel to one side of the 45° V-shaped rib is thinner than produced by the 45° angled rib. Therefore, since the 45° V-shaped rib produces two counter rotating vortices that promote more mixing in the bulk main stream and at the same time produce a thinner boundary layer near the heated surface, a higher heat transfer rate is expected when compared to the 45° angled rib. Similar situation can be observed in the 45° broken V-shaped rib except that the two vortices are generated in two different planes. Thus, the 45° broken V-shaped rib is expected to promote more mixing, which leads to better heat transfer compared to the 45° V-shaped rib.

Figures 4 to 7 show conceptual views for the secondary flow patterns of a smooth and ribbed rotating two-pass rectangular channel. Figure 4 shows the smooth channel that rotates at $\beta=90°$ with respect to the direction of rotation. Two symmetrical cells of counter rotating secondary flow (dotted line) appear due to the Coriolis force. In the first pass of the channel, the fluid moves in a radially outward direction, and the effect of the Coriolis force directs the coolant from the core toward the trailing surface. This causes increase of the heat transfer from the trailing surface and a decrease in the heat transfer from leading surface. However, in the second pass, the opposite situation can be seen: the fluid moves in a radially inward direction, and the Coriolis force directs the coolant toward the leading surface, causing an increase of heat transfer from the leading surface

and a decrease in the heat transfer from trailing surface. When the channel is twisted to β=135° orientation, the secondary flow vortices are asymmetric and migrate diagonally away from the corner region of the inner-leading surface toward the center in the first passage, and from the corner region of the inner-trailing surface toward the center in the second passage. Figures 5 to 7 show three different arrangements of the 45° broken V-shaped ribs. These arrangements are attached to leading and trailing surfaces in a parallel fashion so that they are directly opposite to each other. Figure 5 shows that the 45° broken V-shaped ribs are attached to the leading and trailing surfaces in both passes. Also, it shows the secondary flow (dotted line) induced by rotational forces and the secondary flow (solid line) induced by the 45° V-shaped ribs. As the channel angle changes to β=135°, the rib secondary flow is unchanged, but the rotational secondary flows are shared between the principle surfaces (trailing, and leading) and side surfaces. Figure 6 shows the same channel except that the first pass rib orientation is reversed to become inverted 45° broken V-shaped ribs to the mean stream flow. Consequently, all secondary flows that are induced by rotational forces or ribs are the same as case (b) except the rib secondary flow in the first pass is reversed due to the changing in the rib orientation in the first pass. For case (d), as seen in Figure 7, the first pass and the second pass have broken 45° angled ribs.

Figures 8-23 show the regionally average Nusselt number ratios (Nu/Nuo) from leading and trailing surfaces for four Reynolds number (5000, 10000, 25000, 40000), rotating and non-rotating, and two channel orientations (β=90°, 135°).

Smooth Case Results

Figures 8 to 11 shows the results of Nusselt number ratios from leading and trailing surfaces for the smooth case. For the stationary case, the Nusselt number ratio decreases monotonically for both leading and trailing surfaces in the first pass. This continuous decrease is due to the developing thermal boundary layer. As the flow approaches the 180° turn, the Nusselt number increases due to secondary flows induced by the 180° turn. The Nusselt number reaches the peak value at the entrance of the second pass and then decreases as the flow moves to the exit of the second pass. This is due to the diminishing of the 180° turn-induced secondary flows. The non-rotating results agree with the previous study (see Azad et al. [19]). However, in the rotation case, rotation-induced Coriolis forces produce cross- stream flow patterns, which push the main stream flow from the core towards the trailing surface in the first pass and the leading surface in the second pass. It is also noticed that the rotation effect on Nusselt number ratios for second channel leading and trailing surfaces is not as strong as in the first pass. This is because the Coriolis and buoyancy forces move in the same direction in the first pass, while in the second pass they move against each other (see Han et al [9]). At channel orientation β=90°, rotational secondary flow vortices produced by the Coriolis forces are impinging normally on the trailing surface of the first pass and the leading surface of the second pass. In contrast, at channel orientation β=135°, the secondary flow vortices migrate diagonally away from the corner region toward the center of the passage. In the first pass, it migrates diagonally away from the corner of inner-leading surfaces toward the center of the passage, and in second pass from the corner of the inner-trailing surfaces toward the center of the passage (as explained in Fig.4-a). Thus, the Nusselt number ratio for the

trailing surface of the first pass and the leading surface of the second pass for channel orientation β=90° are higher than the ratio for channel orientation β=135°. The opposite situation is observed in the leading surface of the first pass and the trailing surface of the second pass: the β=135° case has a higher Nusselt number ratio when compared to the β=90° channel orientation. The results also show that the effect of rotation decreases with increasing Reynolds number (or decreasing rotation number).

Broken 45˚ V-shaped Rib Cases

Figures 12 to 15 show the Nusselt number distribution for case (b). The stationary case results show that the peak Nusselt number ratio occurs at the downstream location of the inlet rather than at the entrance region of the first pass as in the smooth case. This is due counter rotating secondary flow vortices that are generated by the broken 45° V-shaped ribs. Then, the Nusselt number ratio decreases as the secondary flow is influenced by the 180° turn. As the flow approaches the exit of the first pass, the Nusselt number ratio continuously decreases due to the 180° turn induced secondary flow. The inlet of the second pass starts from the sharp 180° turn and the Nusselt number profiles differ from the first pass. At the inlet of the second pass, the Nusselt number ratio reaches a minimum value. This drop is due to the decay of the turbulence produced by the sharp 180° turn. Besides the 180° turn, the rib orientation may also be responsible for this drop. Then, the Nusselt number ratio increases downstream of the second pass inlet as the secondary flow induced by the 45° broken V-shaped ribs start to develop after the influence of the 180° turn are diminished.

The results show that rotation significantly increases the Nusselt number ratio on the first pass trailing surface and the second pass leading surface. The rotating Nusselt number ratios on the first pass trailing and second pass leading surfaces are higher than in the non-rotating case, while the first pass leading and second pass trailing surfaces are lower. This is because of the combined effect of the rib-induced secondary flow and the rotation-induced secondary flow vortices, as explained in Fig. 5. The Nusselt number ratio has the same trend as the stationary case, except the first pass leading surface shows slightly decreasing behavior and then increases at the 180° turn. After the 180° turn, the leading surface Nusselt number ratio shows higher values compared to the trailing surface.

The results of the 135° channel also show that rotation enhances the heat transfer in the first pass trailing and second pass leading surfaces, whereas the heat transfer decreases in the first pass leading and second pass trailing surfaces. The heat transfer surfaces are not orthogonal to the plane of rotation in the 135° orientation, and the rotational effects are less significant when compared with the 90° orientation, as explained in Fig. 5. The effect of Coriolis forces on the first pass trailing and second pass leading surfaces for 90° rotation is greater since the pair of rotating vortices are normally incident on the first pass trailing surface and second pass leading surface. Thus greater differences between the leading and trailing Nusselt number ratios in each pass are observed in the 90° orientation. Hence, the differences in Nusselt number ratios between leading and trailing surfaces are not as significant for the 135° orientation as they are for the 90° orientation. In the 180° turn, the leading surface shows a slightly better Nusselt

number ratio than the trailing surface. The results also show that the rotational effect decreases with an increasing Reynolds number (or decreasing rotation number).

Figures 16 to 19 show the Nusselt number ratio for case (c). Case (c) is generated from case (b) by changing the 45° broken V-shaped ribs in the first pass of case (b) to inverted broken 45° V-shaped ribs. The stationary results show that the first pass and the second pass Nusselt number ratios behave similar to case (b). For rotating case, Nusselt number shows continuous increasing until it reaches the maximum value at the exit of the first pass. At the inlet of the second pass, Nusselt number ratio shows the minimum value at the 180 turn. This is because the complicated interaction between the ribs secondary flows, 180 turn, and the Coriolis force. After that the Nusselt number ratio continuously increases.

Figures 20 to 23 show the Nusselt Number ratio for case (d). In case (d), the stationary results show that the first pass Nusselt number ratio behaves differently than in case (b) and (c). The stationary case results show that the highest Nusselt number ratio in the first pass occurs at the entrance region. This peak value is due to the fact that the flow is thermally developing and to the influence of the two pairs of counter rotating secondary flow vortices that are generated by the 45° broken rib. Then the Nusselt number ratio decreases slightly as the flow becomes thermally fully developed. Immediately the Nusselt number ratio increases as the induced secondary flow (two pairs of counter rotating vortices) develop through the first pass. The second pass Nusselt number ratio increases then decreases and increases again as the 180° turn induced secondary flow diminishing. Rotation results show similar behavior as case (b). The

results also show that the rotation effect decreases with an increasing Reynolds number (or decreasing rotation number).

Channel-Averaged Nusselt Number Ratio

Figure 24 presents the averaged Nusselt number ratio distribution for smooth, three different arrangements of the broken 45° V-shaped ribs, the 45° V-shaped ribs, and the inverted 45° V-shaped ribs in the two pass rectangular channels for the stationary case. The Nusselt number ratios in Figure 24 are the average values of the leading and trailing surfaces for all cases. The results show that the ribbed surfaces provide higher Nusselt number ratios in both passes compared to the smooth surfaces. This is because ribs trip the boundary layer and induce secondary flows that promote mixing. In the first pass, case (b) and case (c) show higher averaged Nusselt number ratios compared to other cases. This is because the broken 45° V-shaped rib induces more mixing than other ribs configurations. In the second pass, case (b) and case (c) show better averaged Nusselt number ratios compared to other cases due to the same reason.

It is also noticed that the difference between the Nusselt number ratios in the smooth and ribbed cases in the first pass is greater than in the second pass. On the other hand, the second pass smooth case exhibits better Nusselt number ratios than in the first pass due to the sharp 180° turn effect. It can be concluded that the interaction between the 180° turn-induced secondary flow and rib-induced secondary flow has a major effect on the Nusselt number distribution on the second pass.

Figure 25 and 26 show the channel averaged Nusselt number ratio with respect to Reynolds number for ω=550 rpm on each pass leading and trailing surfaces for β=90° and β=135° respectively. All Nusselt number ratio results exhibit a decreasing trend with

increasing Reynolds number. Ribbed cases provide better Nusselt number ratios enhancement compared to smooth case. This is because, as mentioned above, broken V-shaped ribs trip the boundary layer and promote more mixing with the core region.

The results in Figure 25 show that the Nusselt number ratios in the first pass trailing surface are greater than the Nusselt number ratios in the same pass leading surface. This is due to the rotational force, which distorts the core region toward the trailing surface and thinning the boundary layer. In the second pass, Nusselt number ratios for the leading surface show greater values than the trailing surface due to the opposite effect of rotational force.

In general, Nusselt number ratios in the first pass leading surfaces are about the same for all broken V-shaped cases. However, Nusselt number ratios for the broken V-shaped rib cases (b) and (c) are higher than other cases in the first pass trailing surfaces.

Figure 26 shows the channel averaged Nusselt number ratio on the leading and trailing surfaces for $\beta=135°$. The results are similar to $\beta=90°$ in trend except that the Nusselt number ratios on the first pass trailing and the second pass leading are lower because of the oblique angle of the flow impinging on the surfaces.

Conclusion

The influences of 45° V-shaped rib arrangements and channel orientation on the leading and trailing Nusselt number ratios in a two-pass rectangular channel have been reported for rotation numbers from 0 to 0.21 and Reynolds numbers from 5000 to 40000. The findings are:

1. The general trend of the rotation effect shows an increase in the Nusselt number ratio in the first pass trailing surface and second pass leading surface, while the opposite (decreasing) situation can be observed in the first pass leading surface and second pass trailing surface. This is due to the Coriolis and buoyancy forces, which are generated by rotation. However, the differences between the Nusselt number distributions on the second pass leading and trailing surfaces are smaller than that of the first pass due to the opposite effects of the Coriolis and buoyancy forces.

2. The effects of the Coriolis force and cross-stream flow are reduced as the channel orientation changes from $\beta=90°$ to $\beta=135°$. Thus, the Nusselt number ratios for the $\beta=135°$ first pass trailing and second pass leading surfaces decrease when compared to their corresponding Nusselt number ratios for the $\beta=90°$ orientation. The Nusselt number ratios for $\beta=135°$ first pass leading and second pass trailing surfaces are also enhanced when compared to their corresponding Nusselt number for $\beta=90°$.

3. The broken 45-deg V-Shaped ribs provide better heat transfer enhancement than the V-Shaped ribs and the broken 45-deg angled ribs.

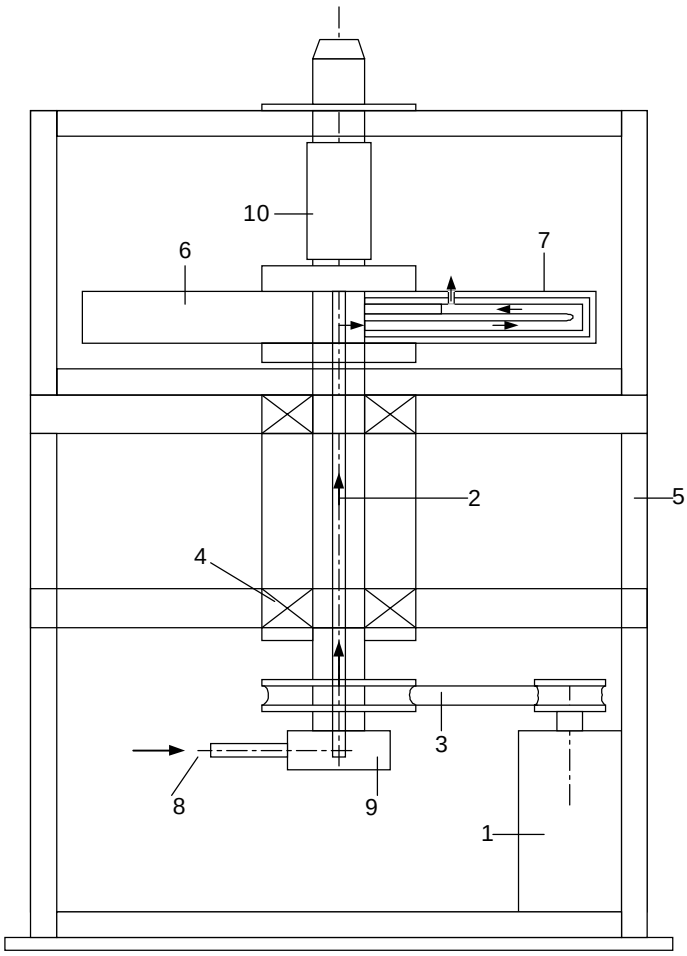

1. Electircal Motor with Controller
2. Rotating Shaft
3. Belt Drive Pulley System
4. Bearing Support System
5. Steel Table
6. Rotating Arm
7. Test Section
8. Compressor Air
9. Rotary Seal
10. Slip Ring

Figure 1. Cross sectional view of the test rig.

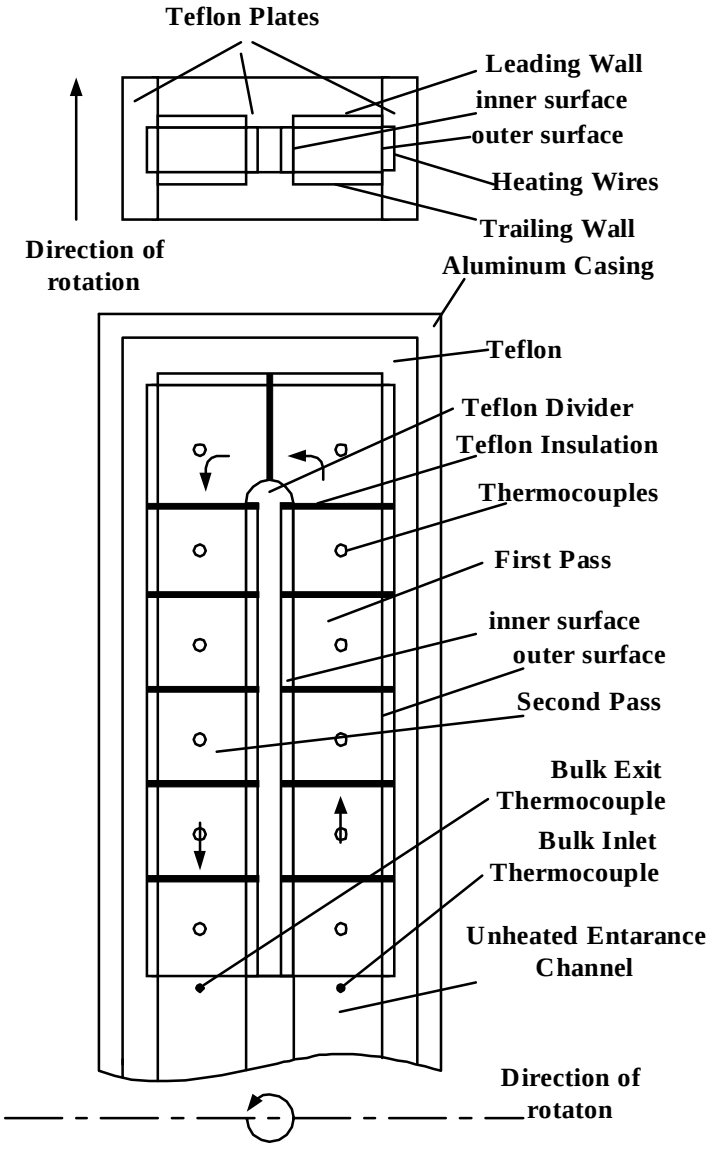

Figure 2. Cross sectional view of the two-pass rectangular test section.

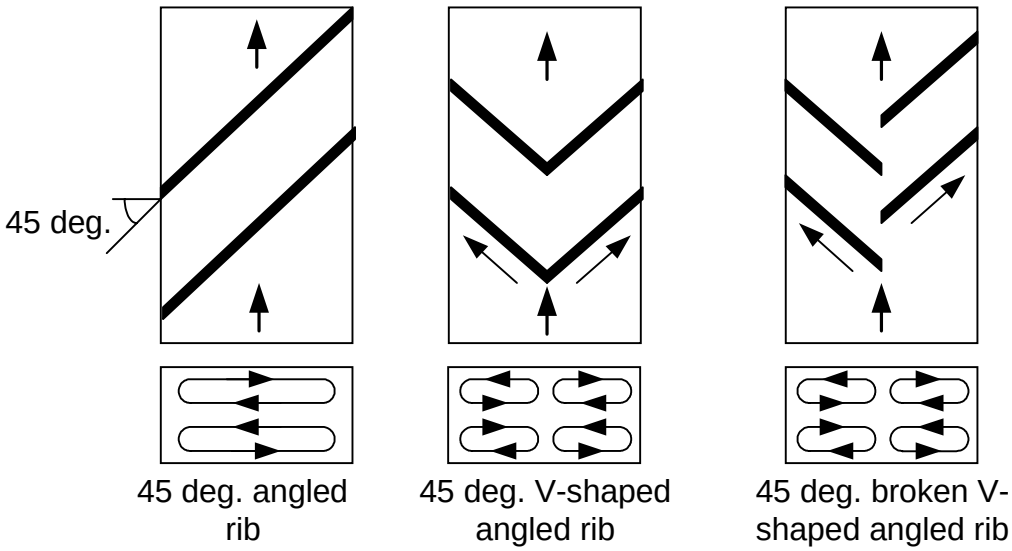

Figure 3. Conceptual view of secondary flow vortices induced by 45° angled ribs, 45° V-shaped ribs and 45° broken V-shaped ribs.

.

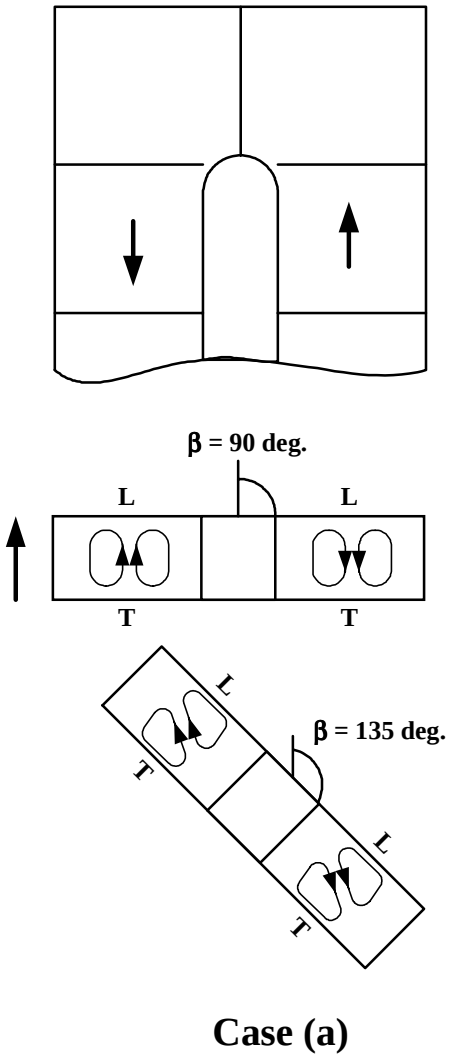

Case (a)

Figure 4. Conceptual view of the secondary flow vortices induced by rotation, and channel orientation (solid line: rotation-induced vortices) for case (a).

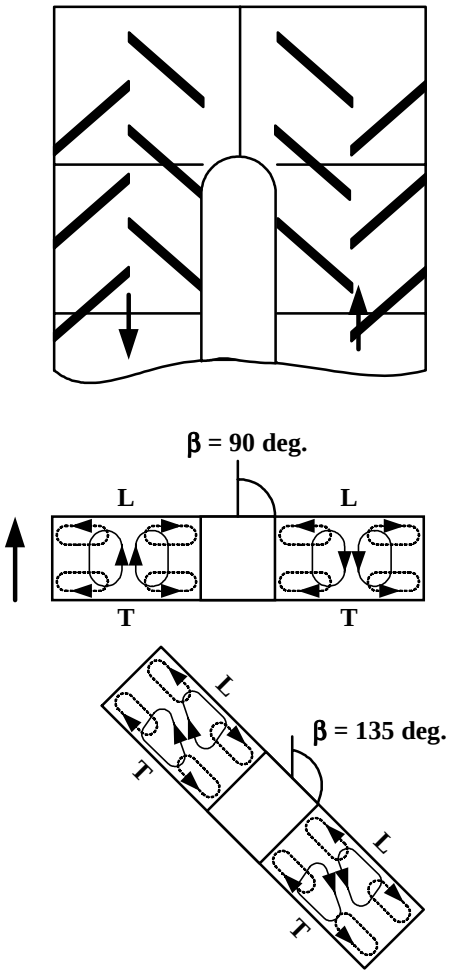

Case (b)

Figure 5. Conceptual view of the secondary flow vortices induced by rotation, ribs, and channel orientation (solid line: rotation-induced vortices, dash line: rib-induced vortices) for case (b).

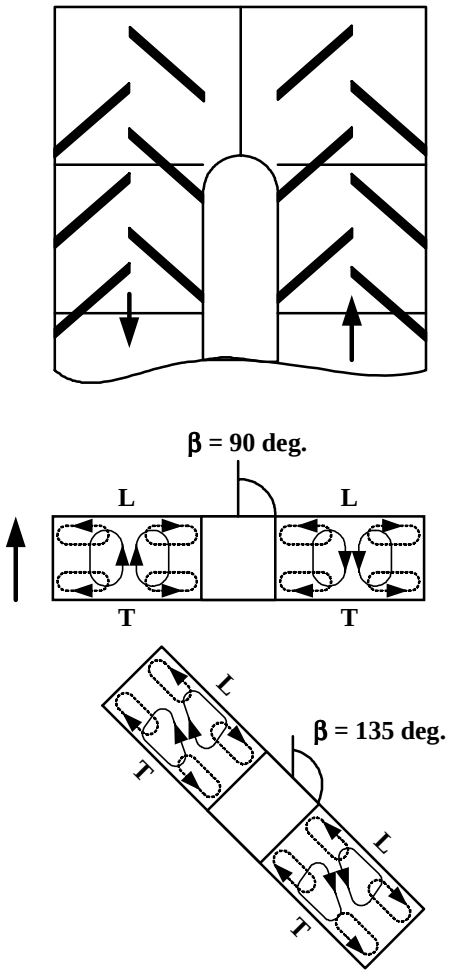

Case (c)

Figure 6. Conceptual view of the secondary flow vortices induced by rotation, ribs, and channel orientation (solid line: rotation-induced vortices, dash line: rib-induced vortices) for case (c).

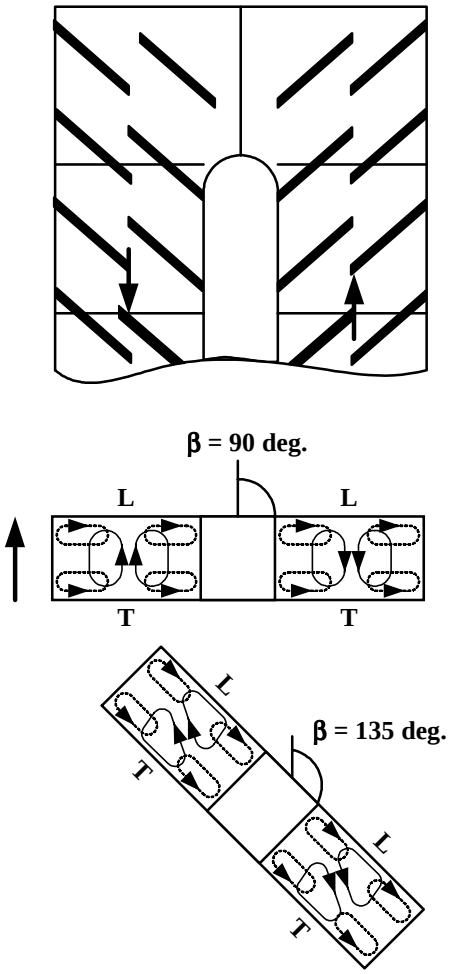

Case (d)

Figure 7. Conceptual view of the secondary flow vortices induced by rotation, ribs, and channel orientation (solid line: rotation-induced vortices, dash line: rib-induced vortices) for case (d).

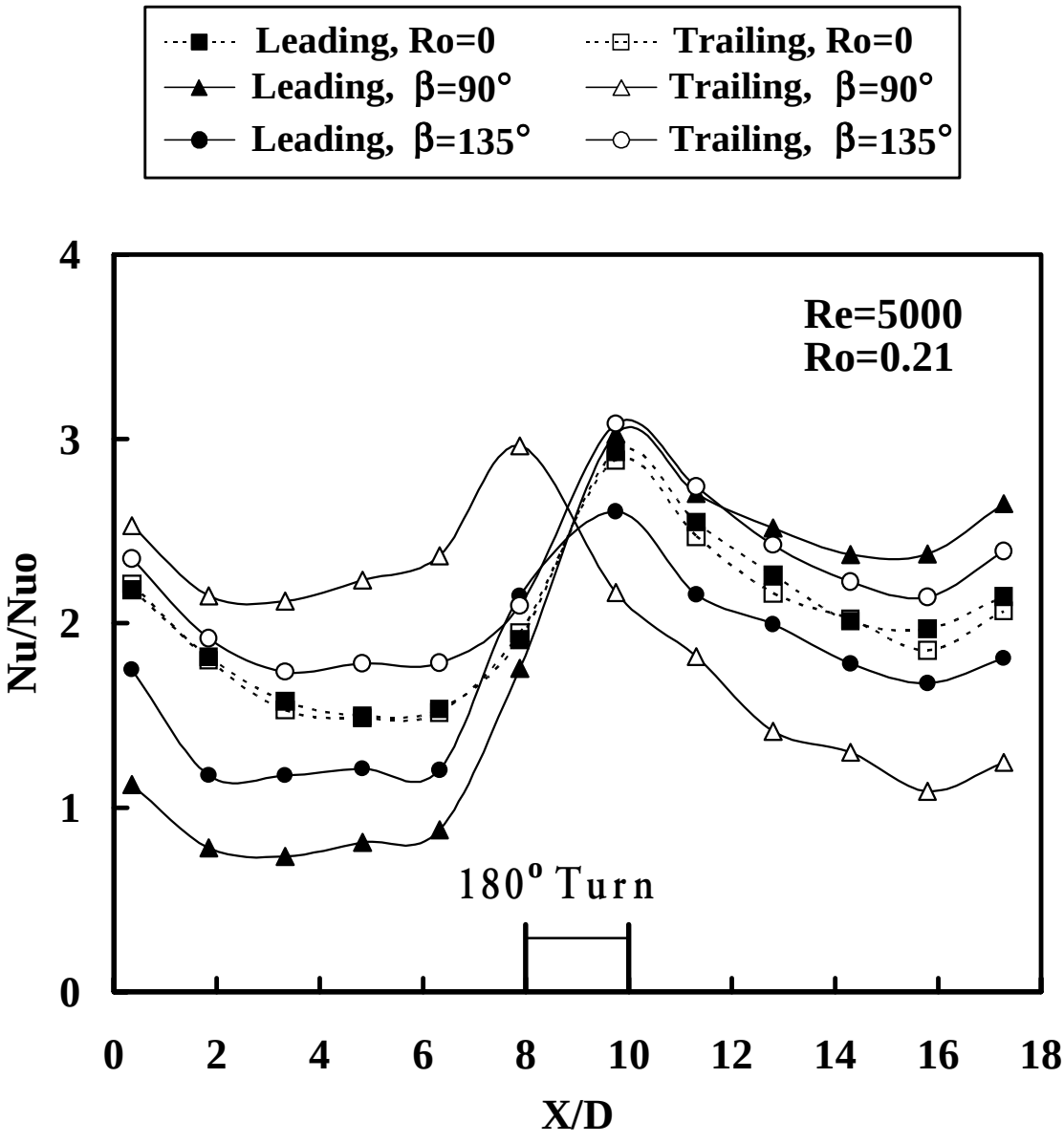

β= 13

Figure 8. Nusselt number distribution for case (a) Re = 5000.

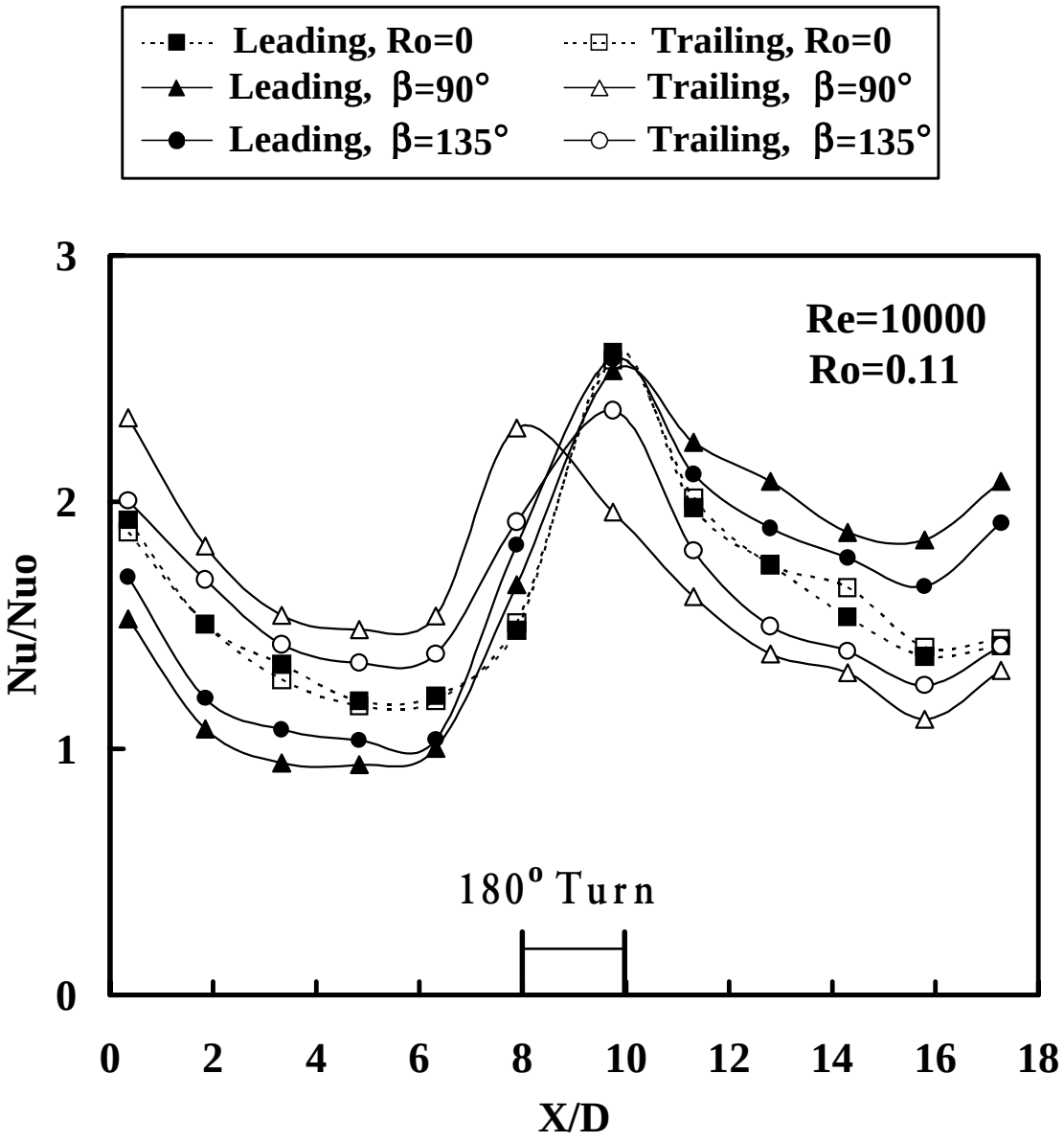

β=13

Figure 9. Nusselt number distribution for case (a) Re = 10000.

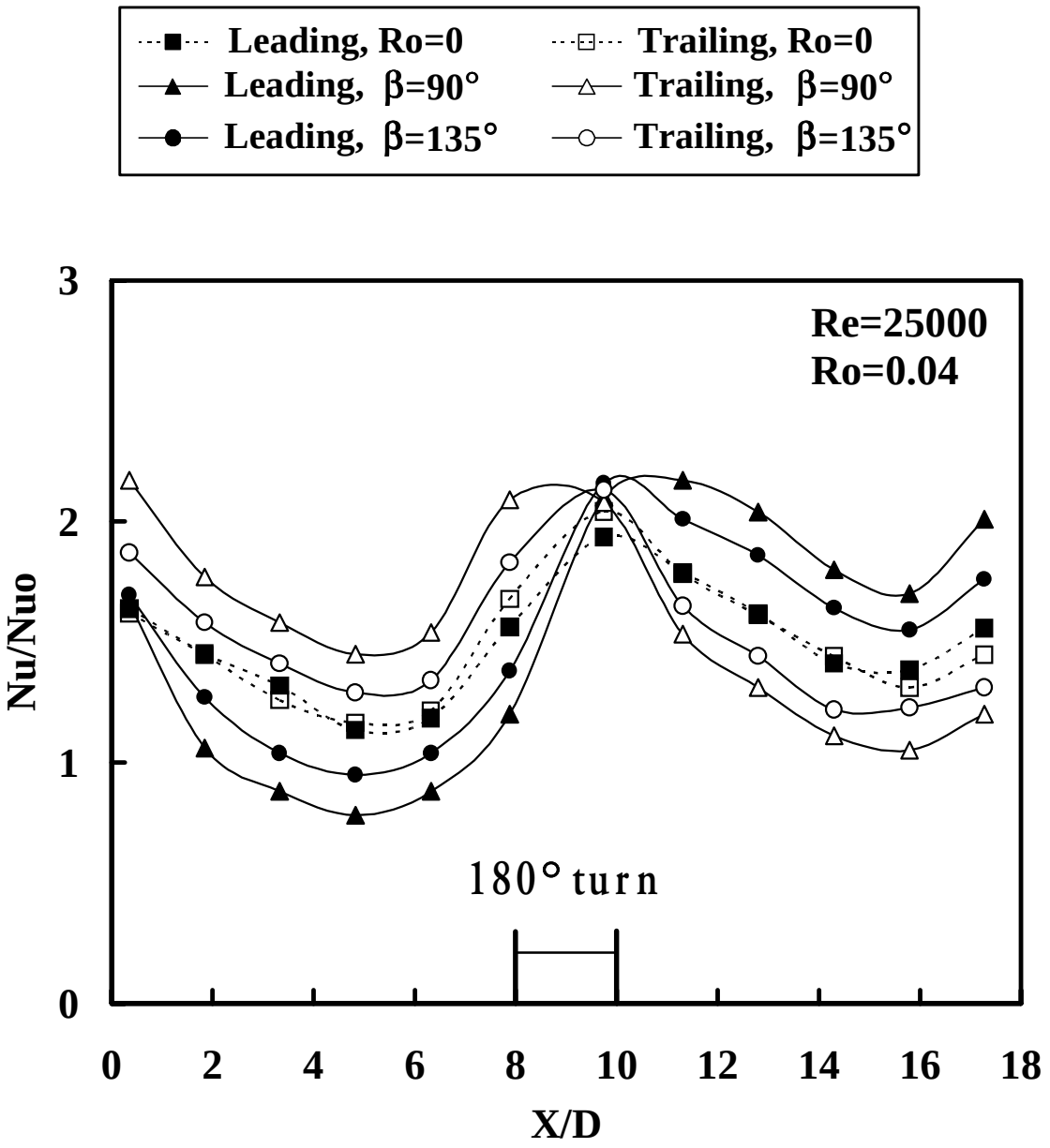

Figure 10. Nusselt number distribution for case (a) Re =250000.

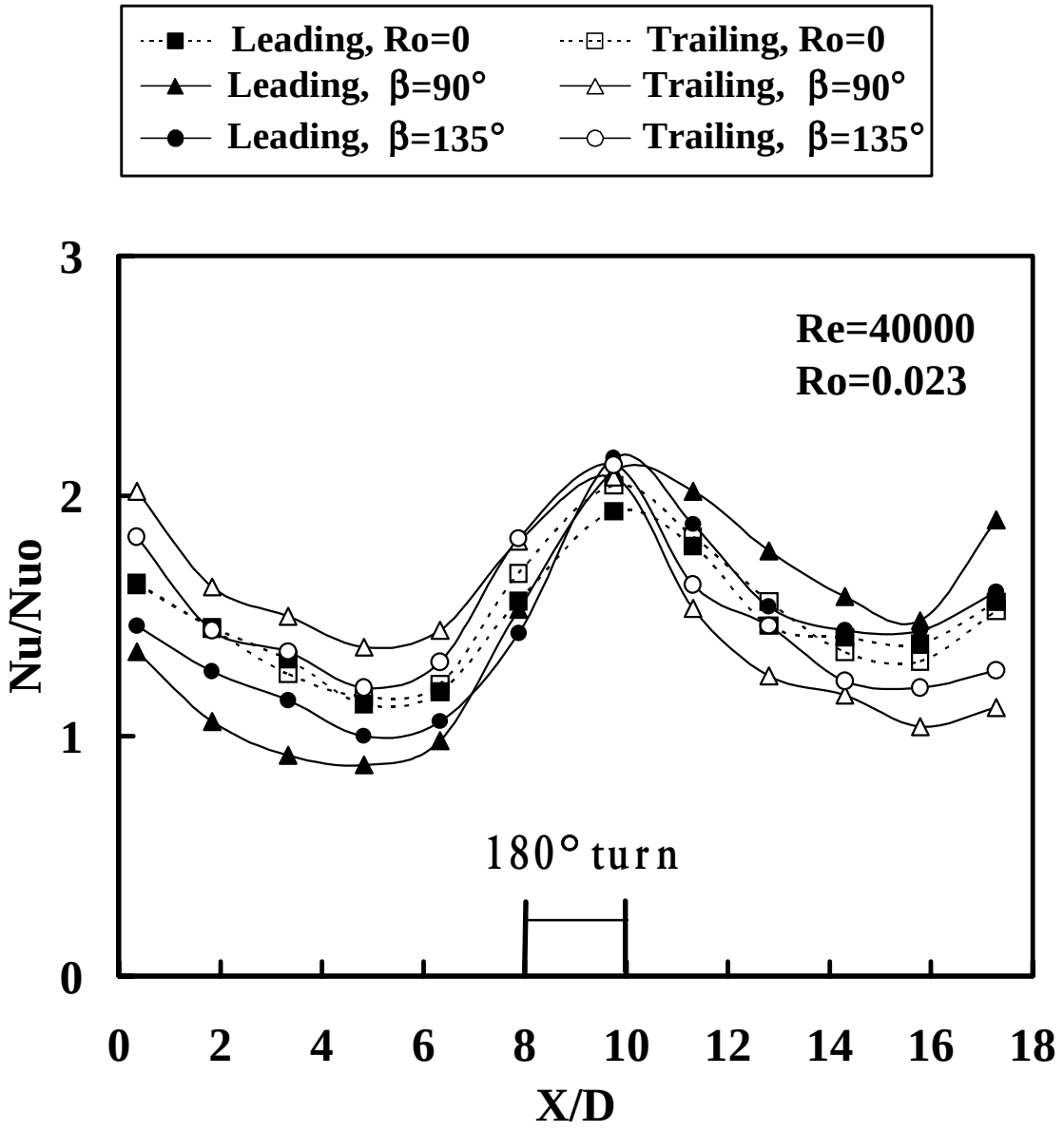

Figure 11. Nusselt number distribution for case (a) Re =400000.

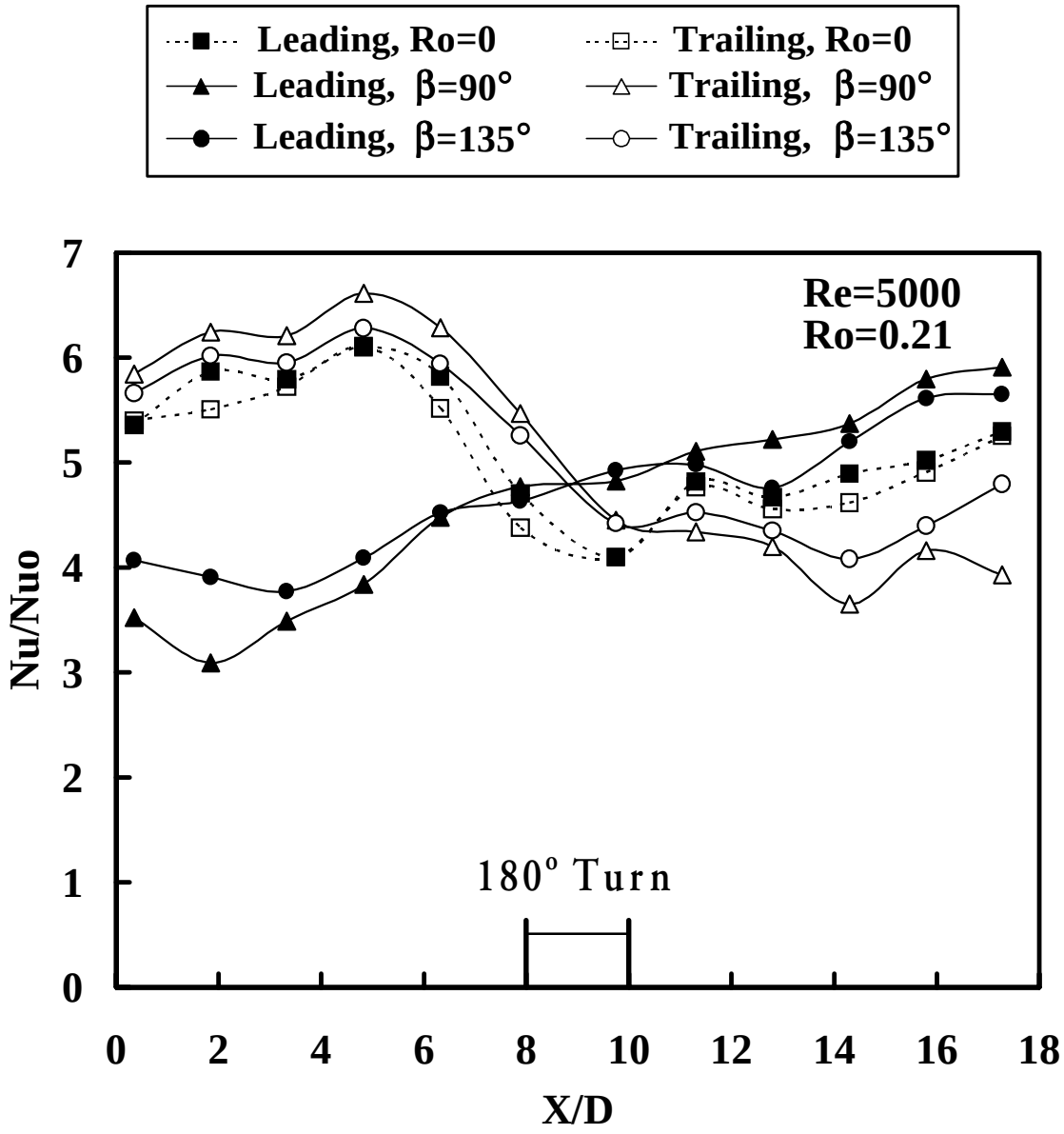

β= 13

Figure 12. Nusselt number distribution for case (b) Re = 5000.

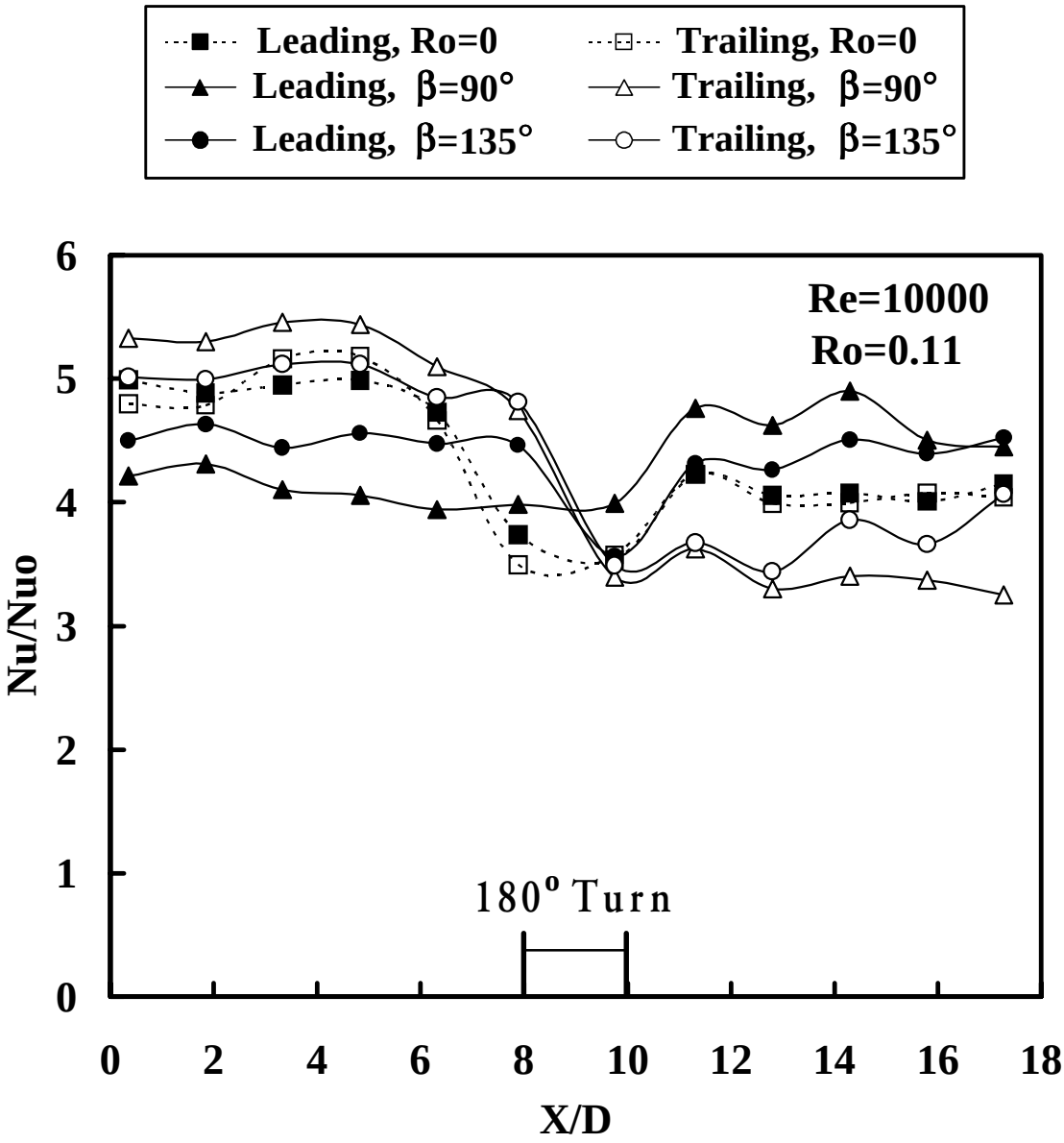

β=13

Figure 13. Nusselt number distribution for case (b) Re = 10000.

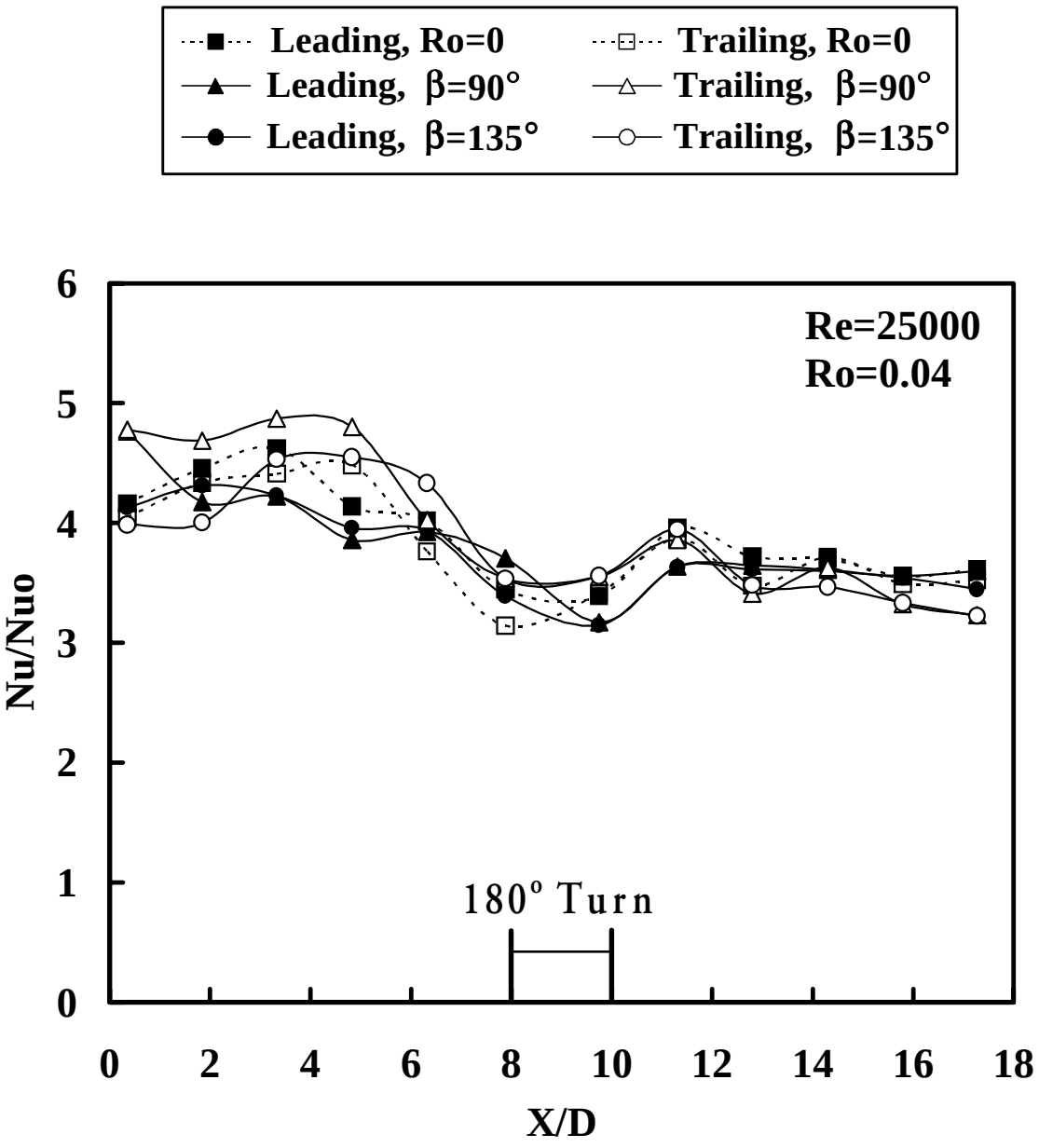

Figure 14. Nusselt number distribution for case (b) Re = 25000.

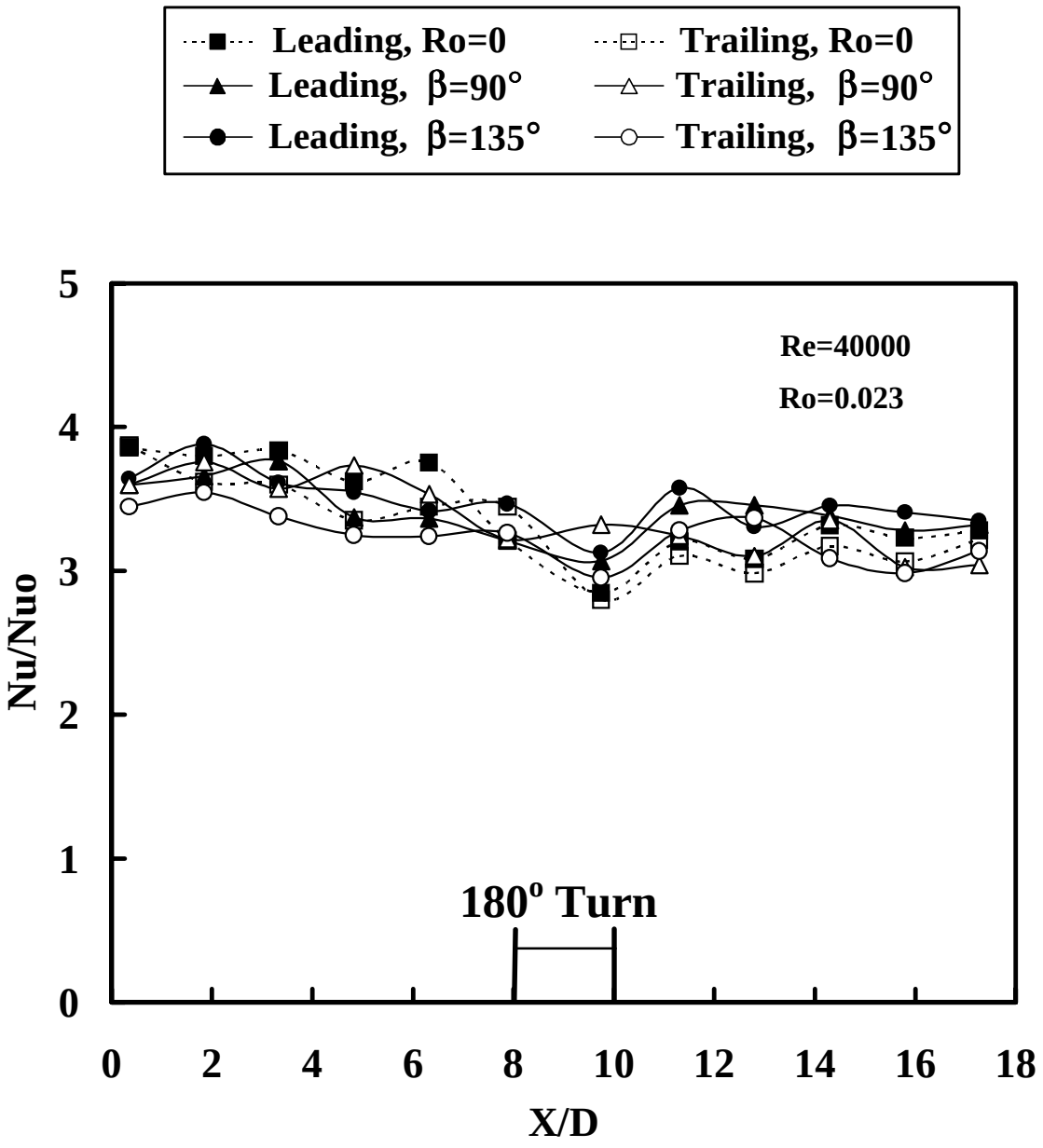

Figure 15. Nusselt number distribution for case (b) Re = 40000.

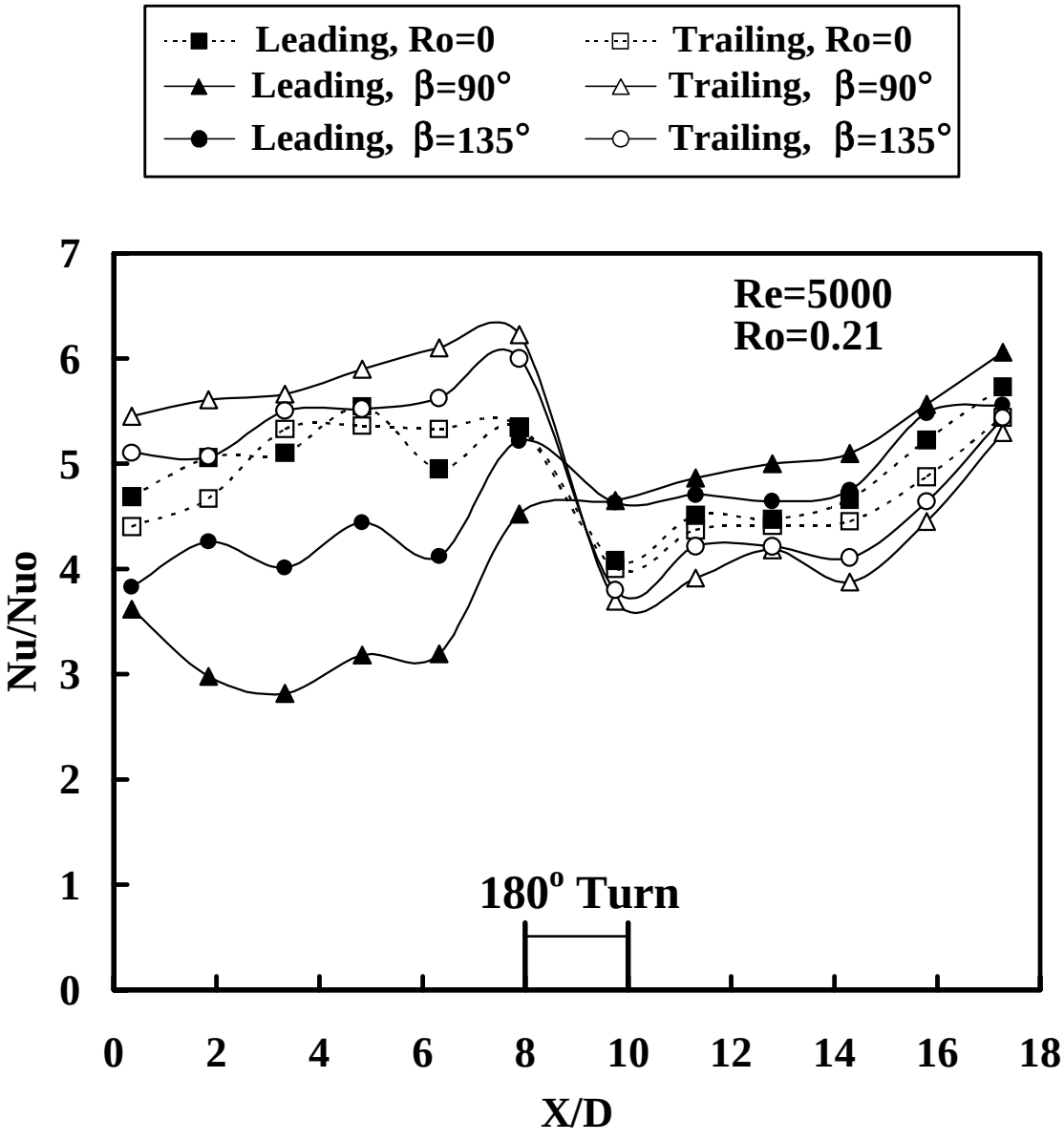

β= 13

Figure 16. Nusselt number distribution for case (c) Re = 5000.

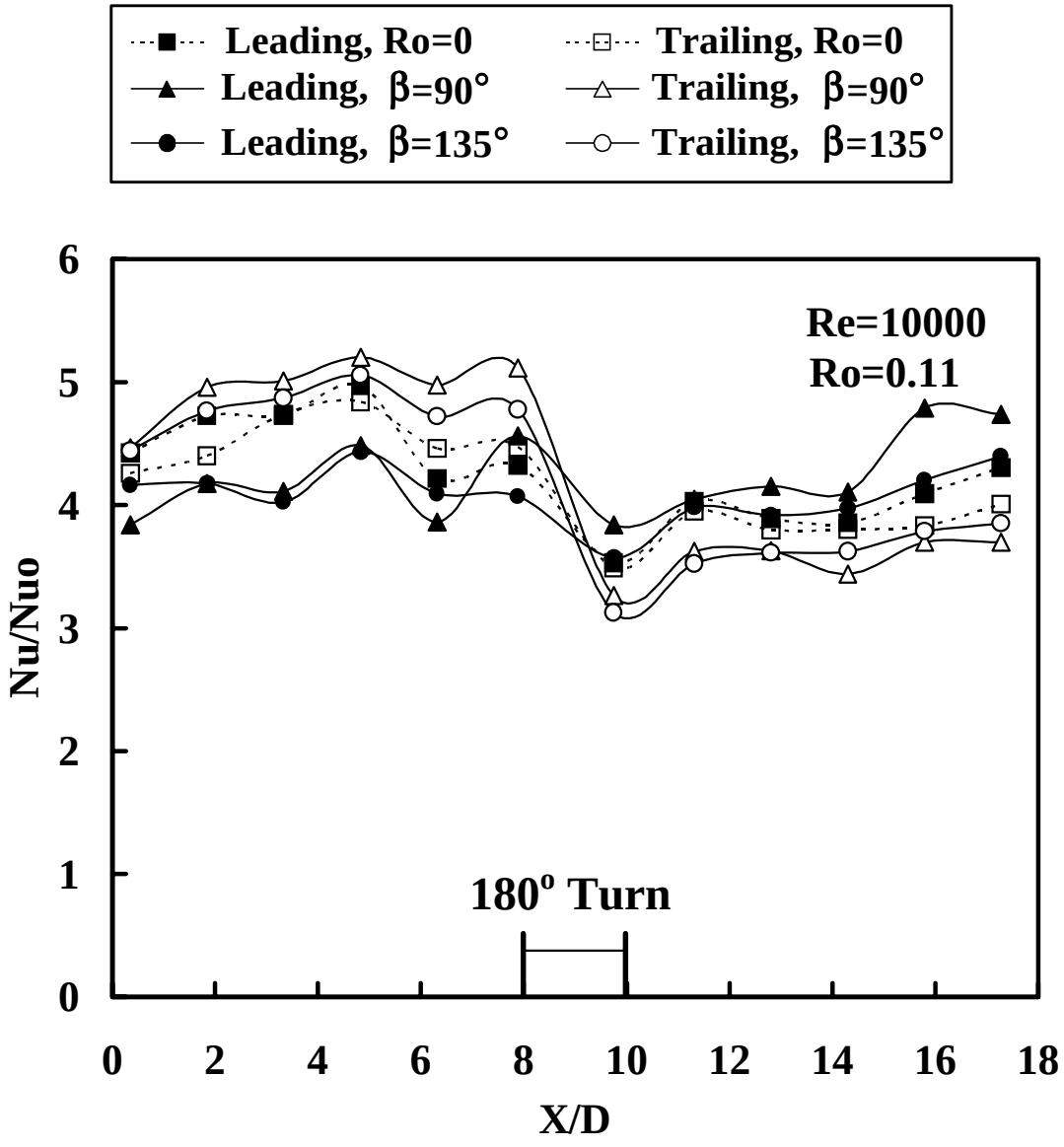

β=135°

Figure 17. Nusselt number distribution for case (c) Re = 10000.

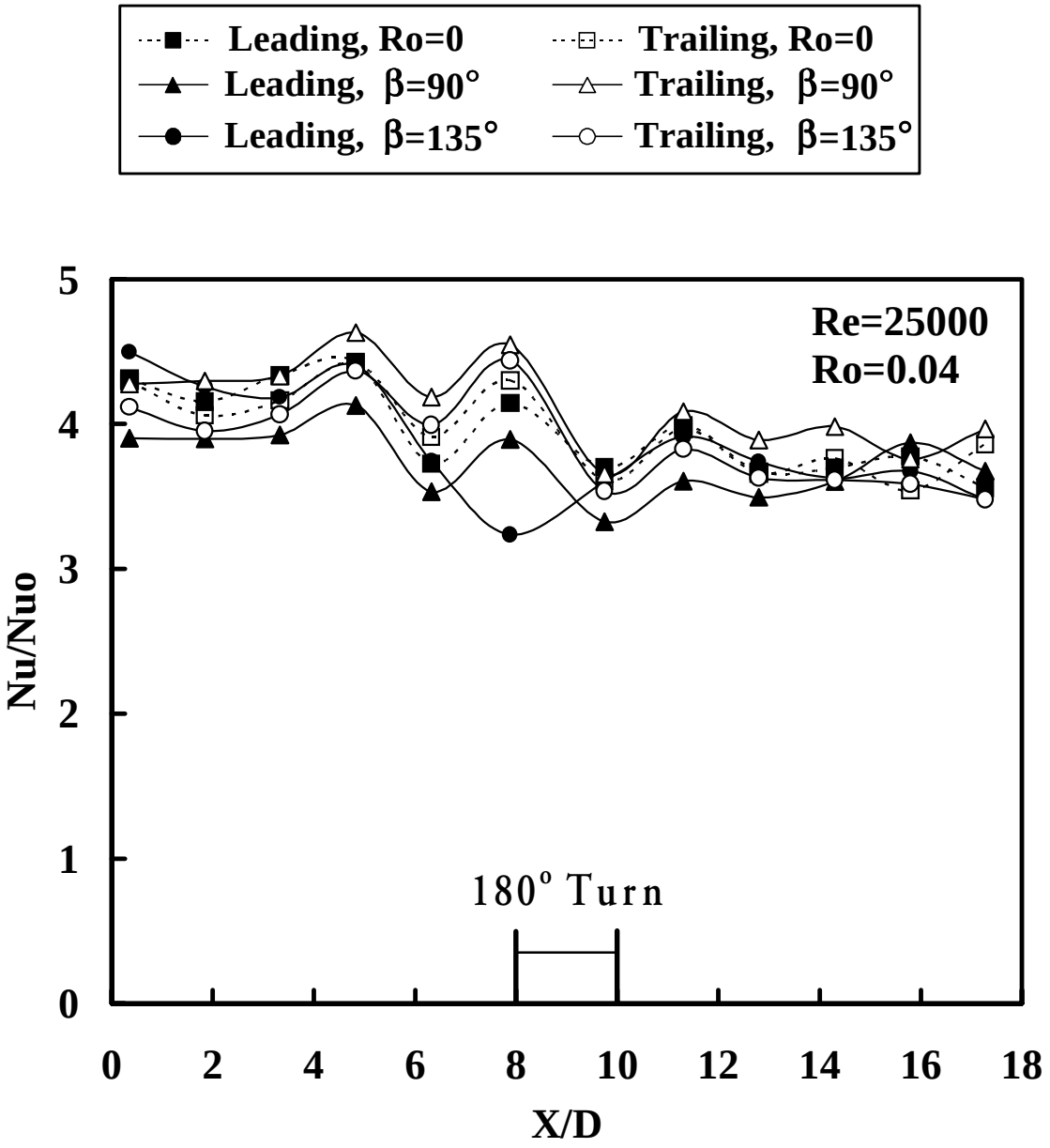

Figure 18. Nusselt number distribution for case (c) Re = 25000.

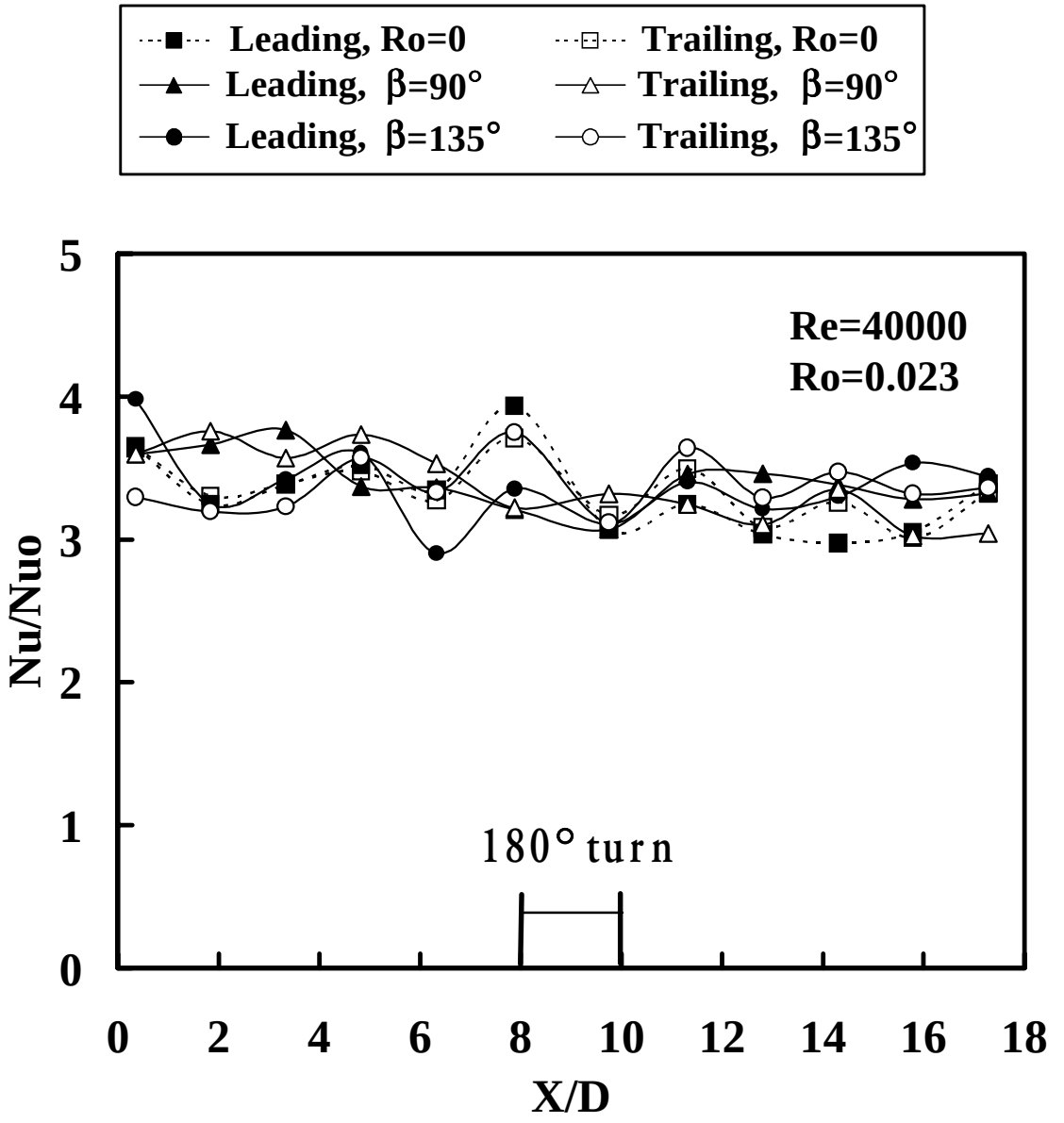

Figure 19. Nusselt number distribution for case (c) Re = 40000.

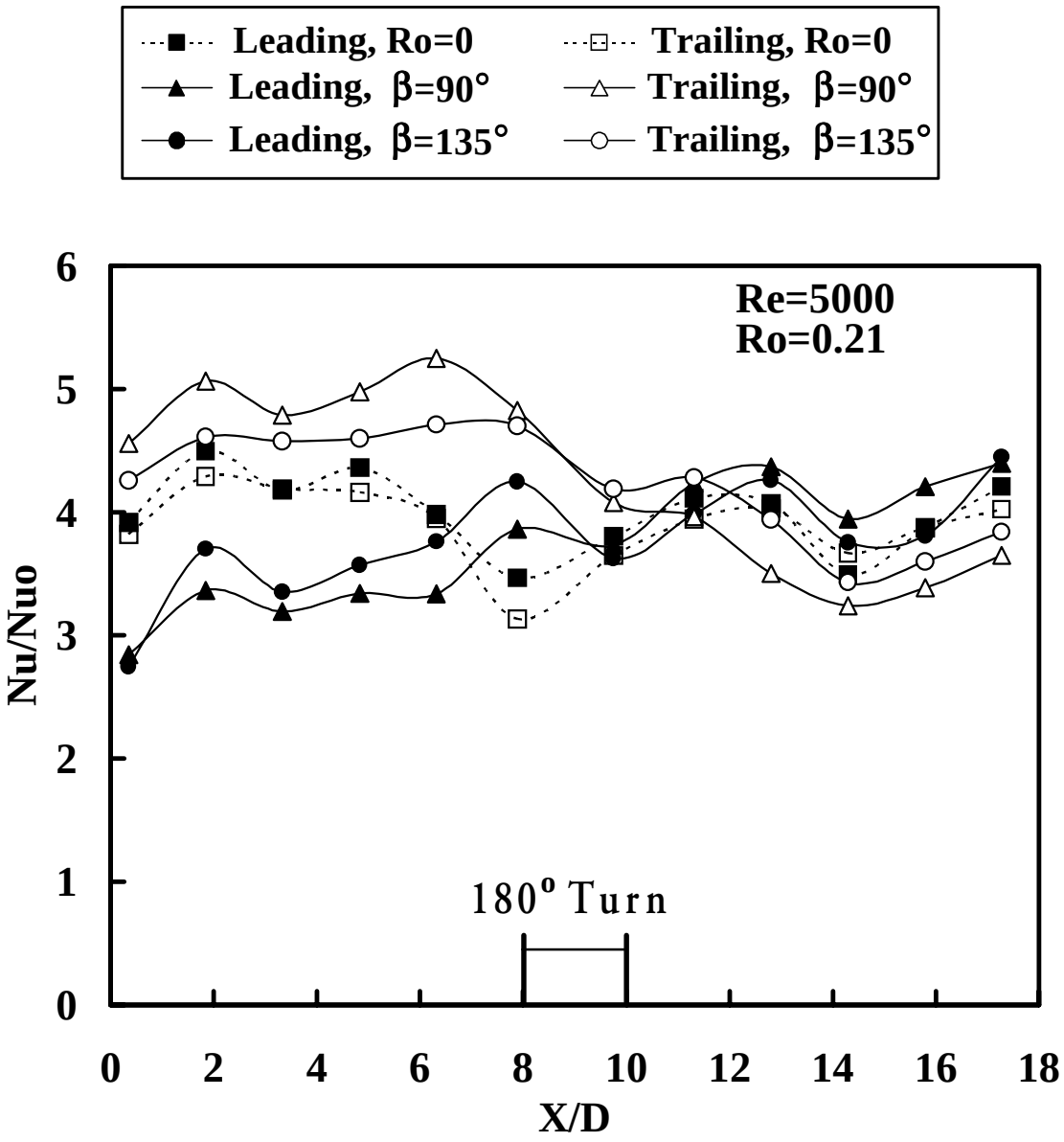

β=13

Figure 20. Nusselt number distribution for case (d) Re = 5000.

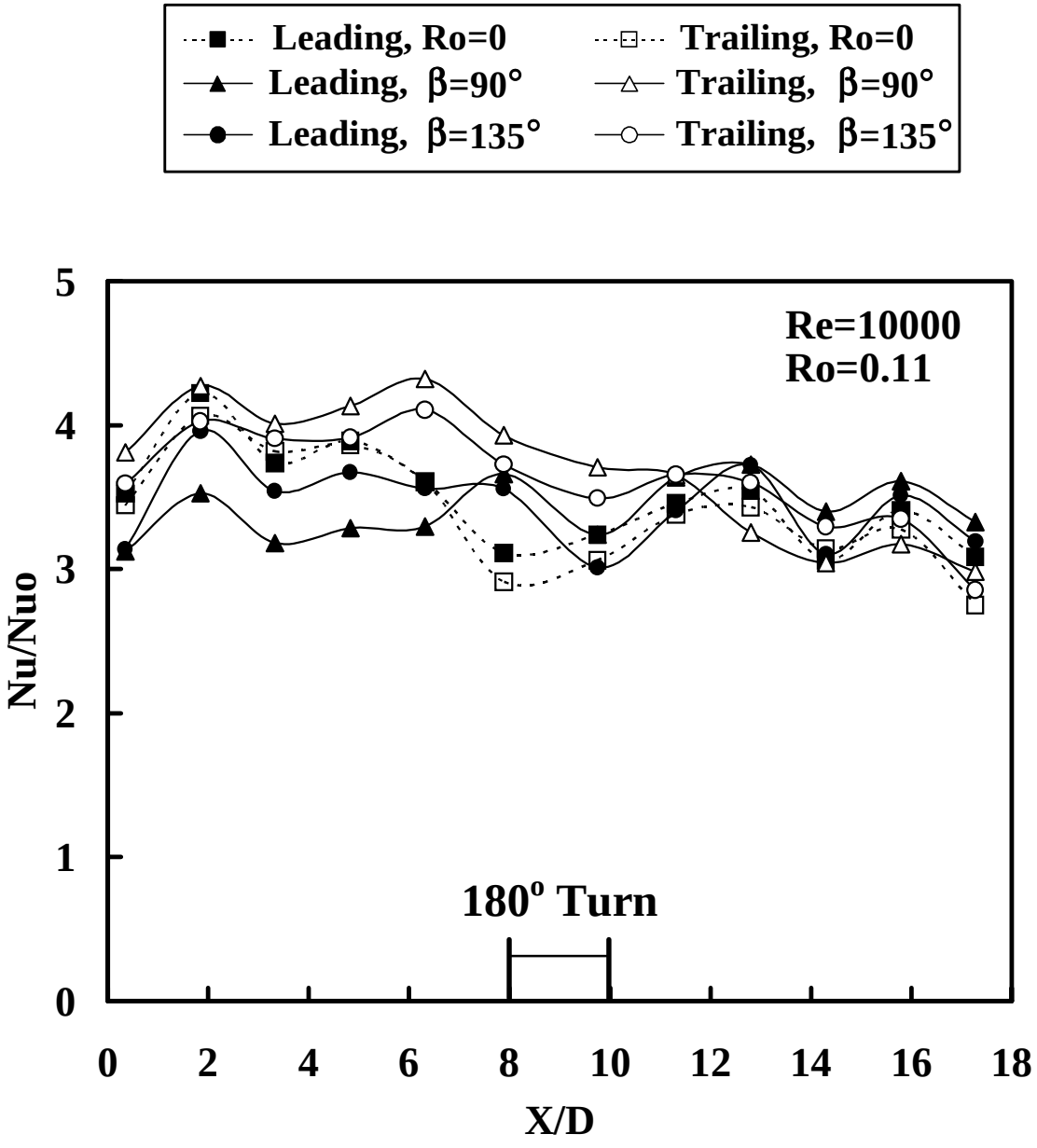

β=135°

Figure 21. Nusselt number distribution for case (d) Re = 10000.

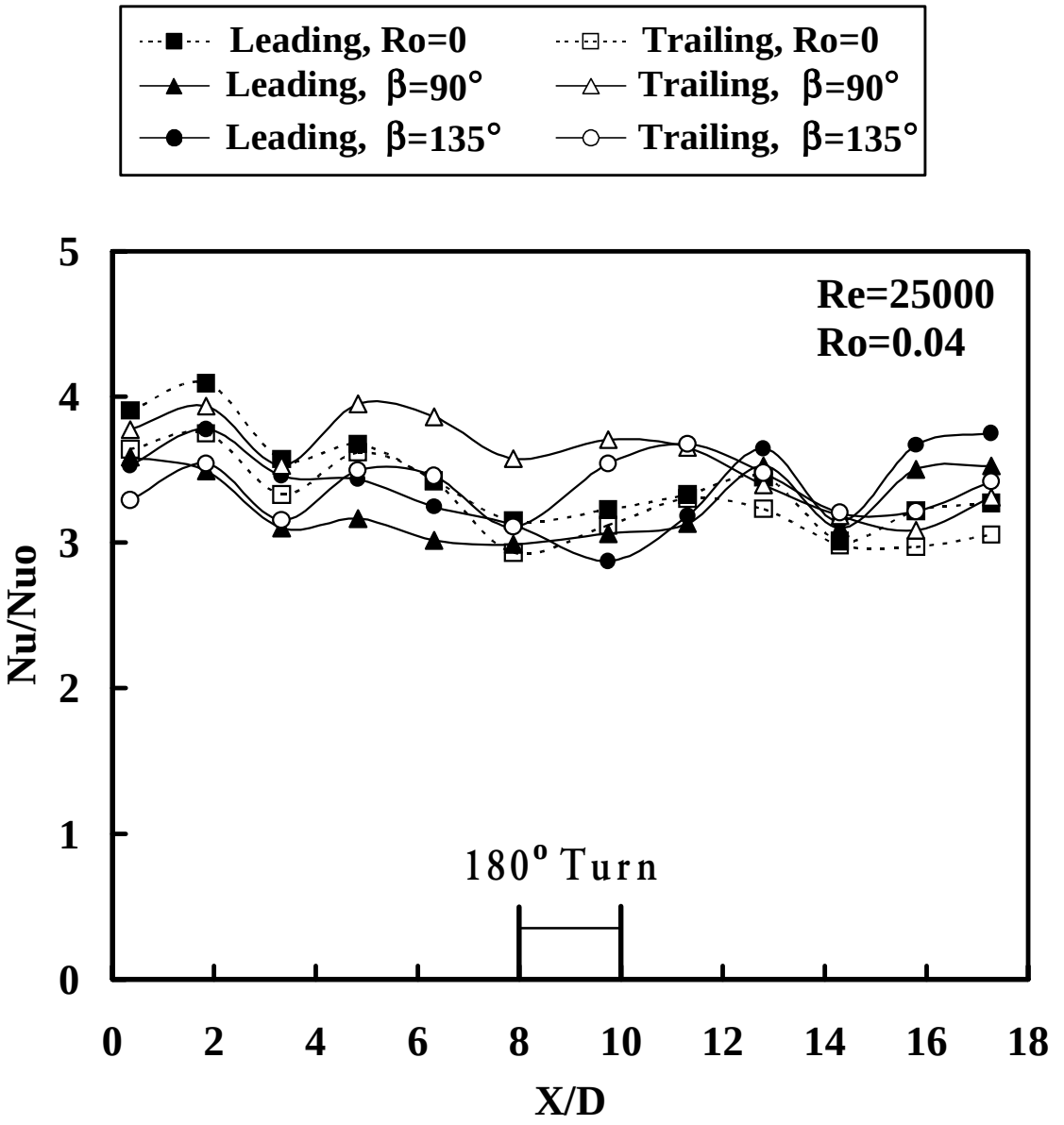

Figure 22. Nusselt number distribution for case (d) Re = 25000.

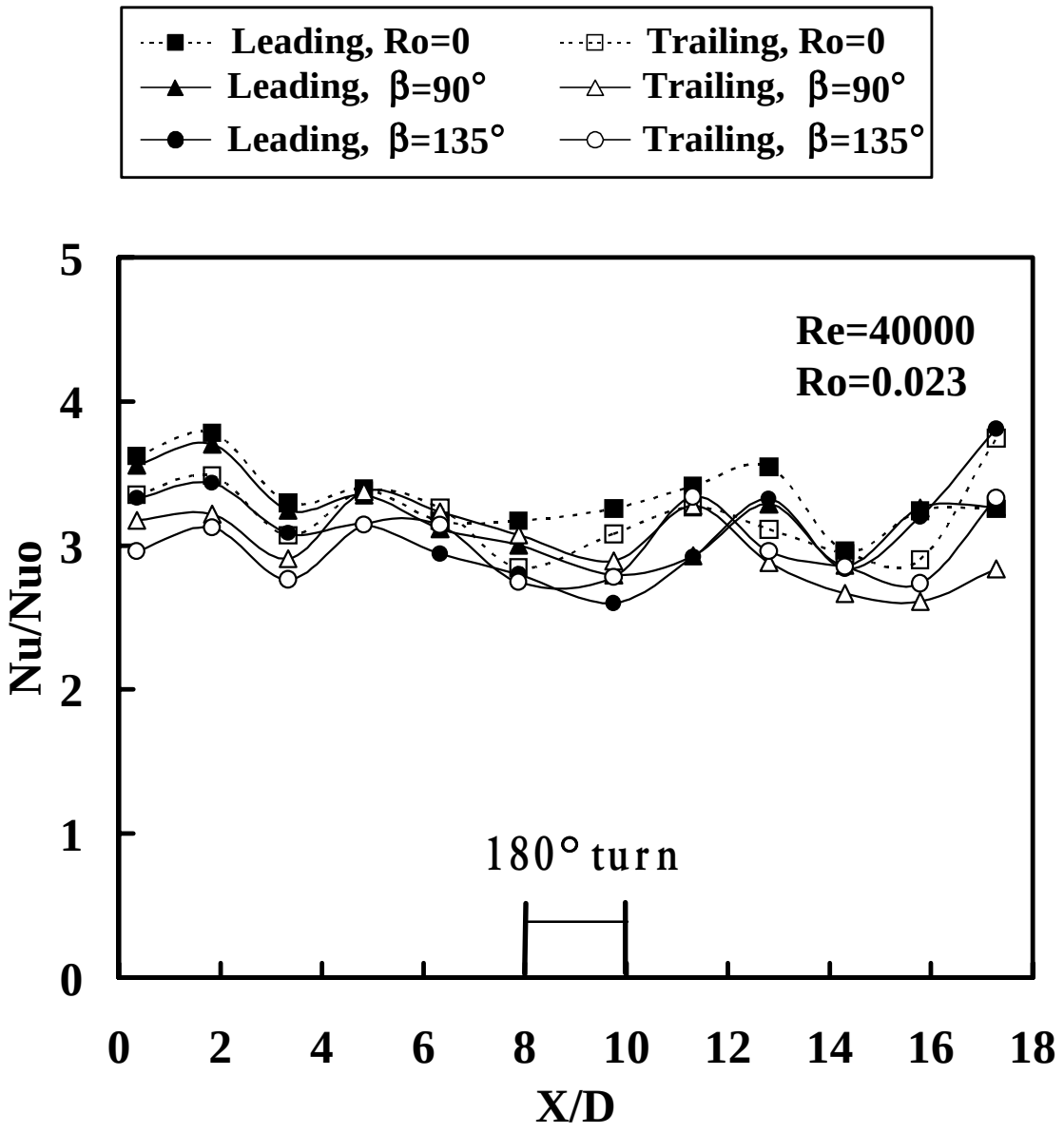

β= 135

Figure 23. Nusselt number distribution for case (d) Re = 40000.

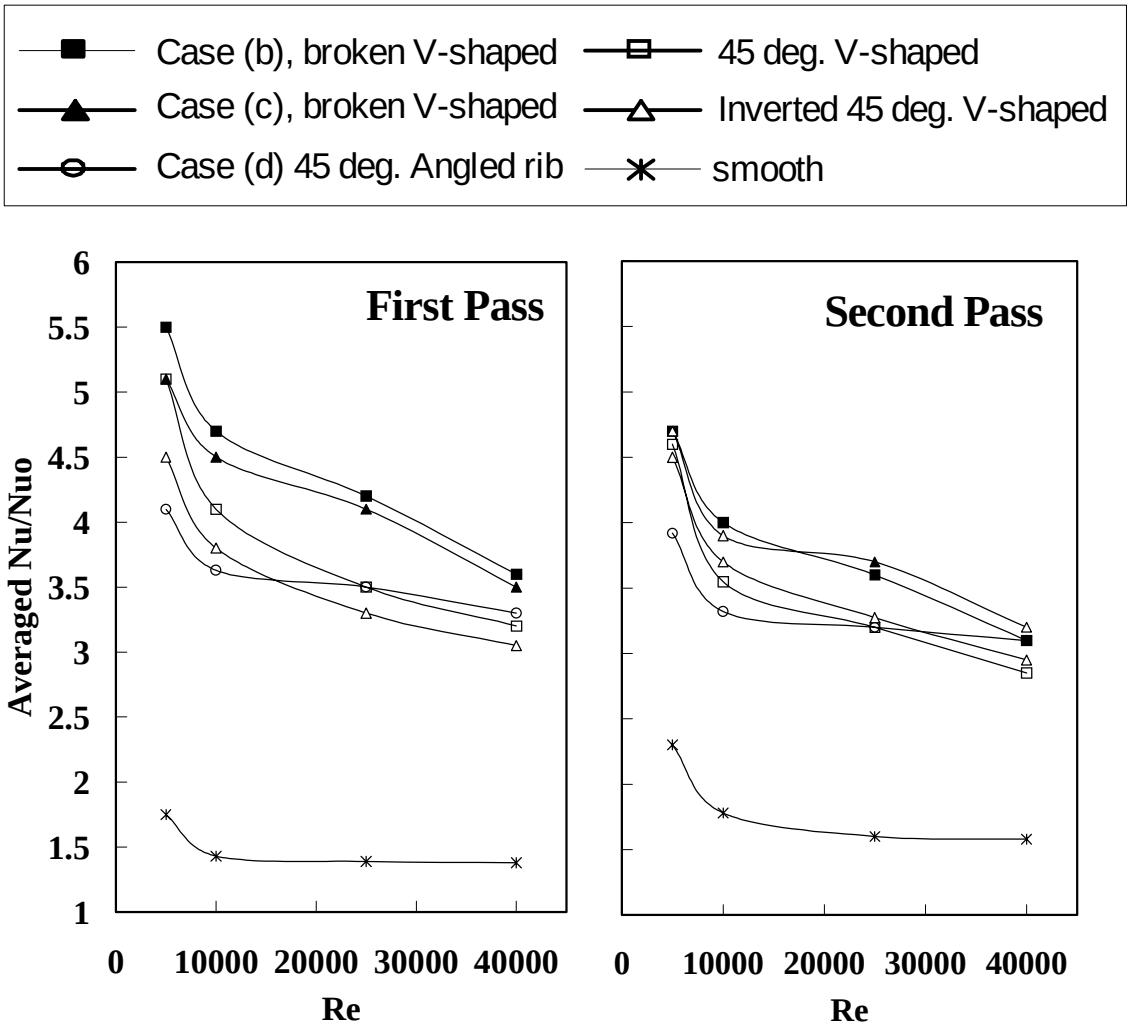

Figure 24. Averaged Nusselt number distribution for non-rotating (ω=0) cases.

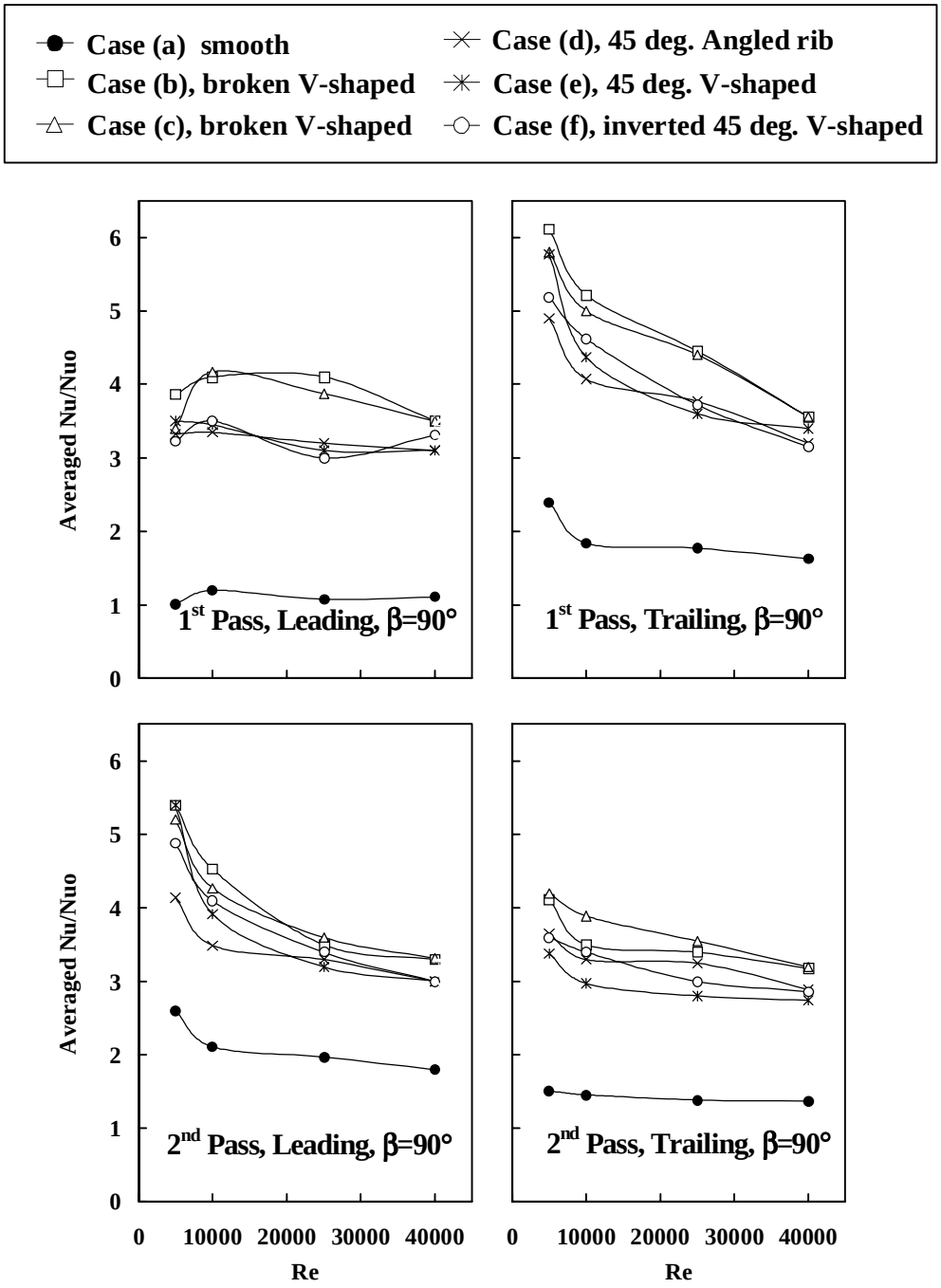

Figure 25. Averaged Nusselt number distribution for leading and trailing surfaces with rotation (ω=550 rpm) for β= 90°.

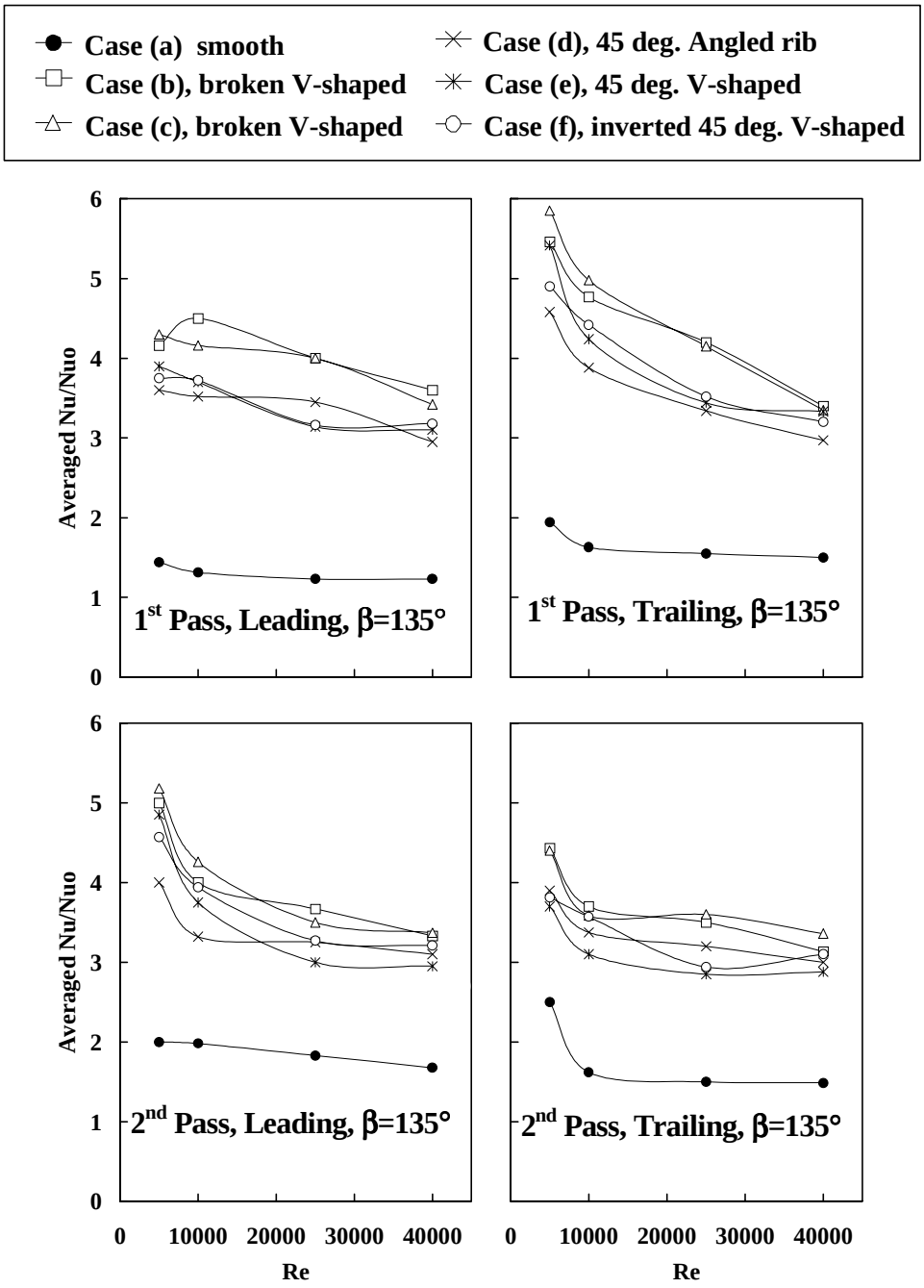

Figure 26. Averaged Nusselt number distribution for leading and trailing surfaces with rotation (ω=550 rpm) for β=135°.

Nomenclature

D	hydraulic diameter (m)
e	rib height (m)
h	heat transfer coefficient (W/m^2K)
k	thermal conductivity of coolant (W/mK)
Nu	local Nusselt number, hD/k
Nu_o	Nusselt number in fully-developed turbulent non-rotating tube flow with smooth wall
P	rib pitch (m)
Pr	Prandtl number
q_{net}	net heat at wall (W)
A	surface area of the copper plate (m^2)
Re	Reynolds number, $\rho VD/\mu$
R_o	rotation number, $\Omega D/V$
T_{bx}	local coolant temperature (^oC)
T_{bi}	coolant temperature at inlet (^oC)
T_w	wall temperature (^oC)
V	bulk velocity in streamwise direction (m/s)
β	angle of channel orientation with respect to the axis of rotation
Ω	rotational speed (rad/s)
ω	rotational speed (rpm)
α	rib angle
μ	dynamic viscosity of coolant (Pa-s)

ρ	density of coolant (kg/m^3)
$\Delta\rho / \rho$	inlet coolant-to-wall density ratio, $(T_w - T_{bi})/T_w$

REFERENCES

[1] Metzger, D. E. and Sahm, M. K., 1986, "Heat Transfer around Sharp 180° Turns in Smooth Rectangular Channels," *ASME Journal of heat transfer*, vol. 113, pp. 500-506.

[2] Fan, C.S. and Metzger, D. E., 1987, "Effects of Channel Aspect Ratio on Heat Transfer in Rectangular Passage Sharp 180° Turn," ASME Paper No. 87-GT-113.

[3] Han, J.C., and Park, J.S., 1988, "Developing Heat Transfer in Rectangular Channels With Rib Turbulators," *International Journal of Heat and Mass Transfer*, Vol. 31, No. 1, pp. 183-195.

[4] Han, J.C., Zhang, Y. M. and Lee, C.P., 1991, "Augmented Heat Transfer in Square Channels With Parallel, Crossed, and V-Shaped Angled Ribs," *ASME Journal of Heat Transfer*, Vol. 113, pp. 590-596.

[5] Ekkad, S.V., and Han, J.C., 1997, "Detailed Heat Transfer Distribution in Two-Pass Square Channels With Rib Turbulators," *International Journal of Heat and Mass Transfer*, Vol. 40, No. 11, pp. 2525-2537.

[6] Wagner, J.H., Johnson, B.V., and Hajek, T.J., 1991a, " Heat Transfer in Rotating Passage With Smooth Walls and Radial Outward Flow," *Journal of Turbomachinery*, Vol. 113, pp. 42-51.

[7] Wagner, J.H., Johnson, B.V., and Kooper, F.C., 1991b, " Heat Transfer in Rotating Serpentine Passage With Smooth Walls," *Journal of Turbomachinery*, Vol. 113, No. 3, pp. 321-330.

[8] Johnson, B.V., Wagner, J.H., Steuber, G.D., and Yeh, F.C., 1994a, " Heat Transfer in Rotating Serpentine Passage With Trips Skewed to the Flow," *Journal of Turbomachinery*, Vol. 116, pp. 113-123.

[9] Han, J.C., Zhang, Y.M., and Kalkuehler, K., 1993, "Uneven Wall Temperature Effect on Local Heat Transfer in a Rotating Two-Pass Square Channel With Smooth Walls," *ASME Journal of Heat Transfer*, Vol. 115, No. 4, pp. 912-920.

[10] Zhang, Y.M., Han, J.C., Parsons, J.A., and Lee, C.P., 1995, " Surface Heating Effect on Local Heat Transfer in a Rotating Two- Pass Square Channel With 60° Angled Rib Turbulators," *ASME Journal of Turbomachinery*, Vol. 117, pp. 272-280.

[11] Parsons, J.A., Han, J.C., and Zhang, Y.M., 1994, " Wall Heating Effect on Local Heat Transfer in a Rotating Two-Pass Square Channel With 90° Rib Turbulators," *International Journal of Heat and Mass Transfer*, Vol. 37, No. 9, pp. 1411-1420.

[12] Johnson, B.V., Wagner, J.H., Steuber, G.D., and Yeh, F.C., 1994b, " Heat Transfer in Rotating Serpentine Passage With Selected Model Orientations for Smooth or Skewed Trip Walls," *ASME Journal of Turbomachinery*, Vol. 116, pp. 738-744.

[13] Parsons, J.A., Han, J.C., and Zhang, Y.M., 1995, "Effects of Model Orientation and Wall Heating Condition on Local Heat Transfer in a Rotating Two-Pass Square Channel With 90° Rib Turbulators," *International Journal of Heat and Mass Transfer*, Vol. 38, No. 7, pp. 1151-1159.

[14] Dutta, S., and Han, J.C., 1996, "Local Heat Transfer in Rotating Smooth and Ribbed Two-Pass Square Channels With Three Channel Orientations," *ASME Journal of Heat Transfer*, Vol. 118, pp. 578-584.

[15] Dutta, S., and Han, J.C., and Lee, C.P., 1996, "Local Heat Transfer in a Rotating Two-Pass Ribbed Triangular Duct With Two Model Orientations," *International Journal of Heat and Mass Transfer*, Vol. 39, pp. 707-715.

[16] Taslim, M.E., Rahman, A. and Spring, S.D., 1991a, "An Experimental Investigation of Heat Transfer Coefficients in a Spanwise Rotating Channel With Two Opposite Rib-Roughened Walls," *ASME Journal of Turbomachinery*, Vol. 113, pp. 75-82.

[17] Taslim, M.E., Bondi, L.A., and Kercher, D.M., 1991b, "An Experimental Investigation of Heat Transfer in an Orthogonally Rotating Channel Roughened With 45º Criss-Cross Ribs on Two Opposite Walls," *ASME Journal of Turbomachinery*, Vol. 113, pp. 346-353.

[18] Prabhu, S.V., and Vedula, R.P., 1997, "Pressure Drop Distribution in a Rotating Rectangular Channel With One Ribbed Surface," *ASME Paper No. 97-AA-118*.

[19] Azad, GM S., Uddin, M. J., Han, J. C., Moon, H. K., and Glezer, B., 2001, "Heat Transfer in Two-Pass Rectangular Rotating Channels with 45° Parallel and Crossed rib Turbulators" *ASME Paper 2001-GT-0186.*

[20] Dutta, S., and Han, J. C., 1998, "Rotational Effect on the Turbine Blade Coolant Passage Heat Transfer," Annual Review of Heat Transfer, vol. IX, pp. 269-314.

[21] Han, J. C., Dutta, S., and Ekkad, S. V., 2000, "Gas Turbine Heat Transfer and Cooling Technology," Taylor & Francis, Inc., New York.

[22] Kline, S.J., and McClintock, F.A., 1953, "Describing Uncertainties in Single-Sample Experiments," *Mechanical Engineering*, Vol. 75, pp. 3-8.

[23] Al-Qahtani, M., Jang, Y., Chen, H., and Han, J.C., 2001, "Prediction of Flow and Heat Transfer in Rotating Two-Pass Rectangular Channels with 45° Rib Turbulators," *ASME Paper 2001-GT-187*

PART II: COMPUTATIONAL STUDY

Part 2 is conducted at Texas A&M University under the direction of Dr. H.C. Chen and Dr. J.C. Han

Computation of Flow and Heat Transfer in Rotating Rectangular Channels (AR = 4) with V-shaped Ribs by Reynolds Stress Turbulence Model

ABSTRACT

Computations were performed to study three-dimensional turbulent flow and heat transfer in a rotating rectangular channel with V-shaped ribs. The channel aspect ratio (AR) is 4:1, the rib height-to-hydraulic diameter ratio (e/D_h) is 0.078 and the rib-pitch-to-height ratio (P/e) is 10. A total of eight calculations will be performed with various combinations of rotation number, Reynolds number, coolant-to-wall density ratio, and channel orientation. The rotation number and inlet coolant-to-wall density ratios, $\Delta\rho/\rho$, will be varied from 0.0 to 0.28 and from 0.122 to 0.40, respectively, while the Reynolds number will be varied from 10,000 to 500,000. Also, three channel orientations (β = 90°, 45°, and 135° from the rotation direction) will be investigated. In this report, we will present detailed numerical results for three different channel configurations. Computations for the remaining five cases are still in progress and will be reported later. A multi-block Reynolds-Averaged Navier-Stokes (RANS) method was employed in conjunction with a near-wall second-moment turbulence closure for detailed predictions of mean velocity, mean temperature, and turbulent Reynolds stresses.

NOMENCLATURE

AR channel aspect ratio

D_h , D hydraulic diameter

e rib height

h heat transfer coefficient

k thermal conductivity of coolant

Nu local Nusselt number, hD/k

Nu_o Nusselt number in fully-developed turbulent non-rotating tube flow, hD/k

Pr Prandtl number

Re Reynolds number, $\rho W_b D_h / \mu$

Ro rotation number, $\Omega D_h / W_b$

R_r radius from axis of rotation

S streamwise distance

T local coolant temperature

T_o coolant temperature at inlet

T_w local wall temperature

W_b bulk velocity in streamwise direction

α rib angle

β channel orientation measured from direction of rotation

ρ density of coolant

$\Delta\rho/\rho$ inlet coolant-to-wall density ratio, $(T_w - T_o)/T_w$

Ω rotational speed

θ dimensionless temperature, $(T - T_o)/(T_w - T_o)$

μ dynamic viscosity of coolant

1. INTRODUCTION

1.1 Motivation: To improve thermal efficiency, gas-turbine stages are being designed to operate at increasingly higher inlet temperatures. A widely used method for cooling turbine blades is to bleed lower-temperature gas from the compressor and circulate it within and around each blade. The coolant typically flows through a series of straight ducts connected by 180° bends and roughened with ribs or pin fins to enhance heat transfer. These cooling ducts may not only be square in cross section or normal to the rotational direction of the blade. In fact, the aerodynamic shape of the turbine blade dictates the use of cooling channels that are rectangular in cross section (with different aspect ratios) and are at an angle, β, from the direction of rotation. Rotation of the turbine blade cooling passages adds another complexity to the problem. It gives rise to Coriolis and buoyancy forces that can significantly alter the local heat transfer in the internal coolant passages from the non-rotating channels. The presence of rib turbulators adds a further complexity since these ribs produce complex flow fields such as flow separation, reattachment and secondary flow between the ribs, which produce a high turbulence level that leads to high heat transfer coefficients.

1.2 Literature Review: Experimental Studies.

The complex coupling of the Coriolis and buoyancy forces with flow separation/reattachment by ribs has prompted many investigators to study the flow and temperature fields generated in heated, rotating ribbed wall passages. Most experimental studies on internal cooling passages have focused on non-rotating ducts. See, for example, Han and Park [1], Han et al. [2] Ekkard and Han [3] and Liou et al. [4] and the references cited there. Experimental studies on rotating

ducts have been less numerous. Wagner et al. [5], Dutta and Han [6], Soong et al. [7] and Azad et al. [8] investigated rotating ducts with smooth and ribbed walls. Wagner et al. [9], Johnson et al. [10 and 11], Parsons et al. [12] and Zhang et al. [13] reported studies on rotating square channels with normal and angled ribs. Azad et al. [8] also investigated the effect of channel orientation on rotating ribbed two pass rectangular channel. Griffith et al. [14] studied the effect of channel orientation on rotating smooth and ribbed rectangular channels with channel aspect ratio of 4:1. They investigated a broad range of flow parameters including Reynolds number (Re = 5000-40000), rotation number (Ro = 0.04-0.3) and coolant to wall density ratio ($\Delta\rho/\rho$ = 0.122). Their experimental results provided a database for the present work.

1.3 Literature Review: Numerical Studies

In addition to the experimental studies mentioned above, several studies have been made to predict numerically the flow and heat transfer in radially rotating smooth and ribbed ducts. Stephens et al. [15, 16] studied inclined ribs in a straight non-rotating square duct. Stephens and Shih [17] investigated the effect of angled ribs on the heat transfer coefficients in a rotating two-passage duct using a low-Re number k-ω turbulence model. They studied the effects of Reynolds numbers, rotation numbers, and buoyancy parameters. Prakash and Zerkle [18], employing a high Reynolds number k-ε turbulence model with wall function, performed a numerical prediction of flow and heat transfer in a ribbed rectangular duct (90° rib) with and without rotation. However, their calculations used periodicity and neglected buoyancy effects. They suggested that a low Reynolds number turbulence model is necessary to simulate real gas turbine engine conditions and a Reynolds stress model is required to capture anisotropic effects. Bonhoff et al. [19] calculated the heat transfer coefficients and flow fields for rotating U-shaped

coolant channels with angled ribs (45°). They used a Reynolds stress turbulence model with wall functions in the FLUENT CFD code. Using the periodicity of the flow, Iacovides [20] computed flow and temperature fields in a rotating straight duct with 90° ribs. Two zonal models of turbulence were tested: a k-ε with a one-equation model of k transport across the near-wall region and a low-Re differential stress model. He concluded that the differential stress model thermal computations were clearly superior to those of the k-ε/one-equation model.

Using the same model and method of Chen et al. [21, 22], Jang et al. [23, 24] studied flow and heat transfer behavior in a non-rotating two-pass square channels with 60° and 90° ribs, respectively. Their results were in good agreement with Ekkad and Han's [3] detailed heat transfer data which validated their code and demonstrated the second-moment closure model superiority in predicting flow and heat transfer characteristics in the ribbed duct. In a later study, Jang et al. [25] predicted flow and heat transfer in a rotating square channel with 45° angled ribs by the same second-moment closure model. Heat transfer coefficient prediction was well matched with Johnson et al. [11] data for both stationary and rotating cases. Al-Qahtani et al. [26] predicted flow and heat transfer in a rotating two-pass rectangular channel with 45° angled ribs by the same second-moment closure model of Chen et al. [21, 22]. Heat transfer coefficient prediction was compared with the data of Azad et al. [8] for both stationary and rotating cases. It predicted fairly well the complex three-dimensional flow and heat transfer characteristics resulting from the angled ribs, sharp 180° turn, rotation, centrifugal buoyancy forces and channel orientation.

In practice, the aerodynamic shape of the turbine blade dictates the use of cooling channels that are rectangular in cross section and are at an angle β from the direction of rotation. The effect of rotation, channel orientation and large channel aspect ratio on the secondary flow and heat transfer in rectangular channels may vary from the square channels.

The objective of this study is to use the second moment RANS method of Chen et al. [21, 22] to (1) predict the three-dimensional flow and heat transfer for rotating one-pass rectangular ducts (AR = 4:1) with V-shaped ribs and (2) to investigate the effect of high rotation and high density ratios on the secondary flow field and the heat transfer characteristics in a ribbed duct at 45° and 135° orientation.

2. DESCRIPTION OF PROBLEM

A schematic diagram of the geometry is shown in **Figure 1**. It has a rectangular cross section with channel aspect ratio, AR, of 4:1. Two of the four side walls, in the rotational direction, are denoted as the leading and trailing surfaces, respectively, while the other two side walls are denoted as the top and bottom surfaces. The channel hydraulic diameter, D_h, is 0.8 in (2.03 cm). The distance from the inlet of the channel to the axis of rotation (Y-axis) is given by R_r/D_h = 20.0 and the length of the channel is given as L/D_h = 22.5. The channel consists of unheated starting smooth length (L_1/D_h= 9.92), heated smooth or ribbed section (L_2/D_h= 7.58) and unheated exit smooth section (L_3/D_h=5.00). The arc length S is measured from the beginning of the heated section to the end of it. In the ribbed section, the leading and trailing surfaces are roughened with nine equally spaced V-shaped ribs of square cross section. The rib height-to-hydraulic diameter ratio (e/D_h) is 0.078 and the rib-pitch-to-height ratio (P/e) is 10. All ribs are

inclined at an angle $\alpha = 45°$ with respect to the flow. Three channel orientations of $\beta = 90°$, 45° and 135° are studied: $\beta = 90°$ corresponding to the mid-portion of a turbine blade and $\beta = 135°$ corresponding to the trailing edge region of a blade. A summary of the cases studied is given in Table 1.

Case #	Ro	$\Delta\rho/\rho$	β	Re
1	0.00	0.122	-	10,000
2	0.14	0.122	90°	10,000
3	0.14	0.122	45°	10,000
4	0.14	0.122	135°	10,000
5	0.00	0.122	-	100,000
6	0.00	0.122	-	500,000
7	0.28	0.200	135°	500,000
8	0.28	0.400	135°	500,000

Table 1: Summary of cases studied.

3. COMPUTATIONAL PROCEDURE

3.1 Overview

The Reynolds-Averaged Navier-Stokes equations in conjunction with a near wall Reynolds stress turbulence model are solved using the chimera RANS method of Chen et al. [21, 22]. The governing equations with the second-moment closure turbulence model were described in detail by Chen et al. [21, 22] and will not be repeated here. The flow is considered to be incompressible since the Mach number is quite low. However, the density in the centrifugal

force terms is approximated by $\rho=\rho_o T_o/T$ to account for the density variations caused by the temperature differences. ρ_o *and* T_o are the density and temperature at the inlet of the cooling channel. In general, the density is also a function of the rotating speed because the centrifugal force creates a pressure gradient along the duct. In the experiments of Griffith et al. [14], the maximum pressure variation between the channel inlet and the exit is approximately 0.0113 atm for the highest rotation number of 0.28 (i.e., Ω = 550 rpm) considered in the present study. This gives a maximum density variation of only about 1.1% from the inlet to the exit of the duct at the highest rotation number. It is therefore reasonable to omit the density variation caused by the pressure gradients induced by the channel rotation.

3.2 Boundary conditions

A uniform velocity profile was used at the inlet of the duct ($Z = 0$). The unheated length (L_1) was long enough for the velocity profile to be fully developed turbulent profile before the heating start-point ($Z = L_1$). At the exit of the duct, zero-gradient boundary conditions were specified for the mean velocity and all turbulent quantities, while linear extrapolation was used for the pressure field. The coolant fluid at the inlet of the duct is air at uniform temperature $T = T_o$ (i.e., $\theta = (T - T_o) / (T_w - T_o) = 0$). The wall temperature of the unheated sections is kept constant at $T = T_o$ ($\theta = 0$) while the wall temperature of the heated section is kept constant at $T = T_w$ ($\theta = 1$).

3.3 Computational grid details

Figure 2 shows the computational grid around the ribs for the ribbed duct. The grid was generated using an interactive grid generation code GRIDGEN [27]. It was then divided into

five overlapped chimera grid blocks (three for the case of smooth duct) to facilitate the implementation of the near-wall turbulence model and the specification of the boundary conditions. To provide adequate resolutions of the viscous sublayer and buffer layer adjacent to a solid surface, the minimum grid spacing for Re = 10,000 cases is maintained at 10^{-3} of the hydraulic diameter which corresponds to a wall coordinate y^+ of the order of 0.5. The number of grid points in the streamwise direction from inlet to outlet is 50 for the smooth case and 394 for the ribbed duct, and the number of grid points in the cross-stream plane is 33×75. The number of grid points and their distributions in the present smooth and ribbed ducts were obtained based on extensive grid-refinement studies that were performed in Chen et al. [21, 22], Jang et al. [23-25] and Al-Qahtani [26] for similar channels of a square and rectangular cross sections. The interested reader is referred to these references for the details of the grid refinement studies performed on the similar smooth and ribbed channels. In all calculations, the root-mean-square (rms) and maximum absolute errors for both the mean flow and turbulence quantities were monitored for each computational block to ensure complete convergence of the numerical solutions and a convergence criterion of 10^{-5} was used for the maximum rms error.

4. RESULTS AND DISCUSSION

As summarized in Table 1, computations will be performed for three Reynolds numbers (10,000, 100,000 and 500,000), rotation numbers ranging from 0 to 0.28 and inlet coolant-to-wall density ratios $\Delta\rho/\rho$ ranging from 0.122 to 0.40 with three channel orientations of $\beta = 90^o$, 45^o and 135^o. In this report, we will present detailed numerical results for the first three test configurations shown in Table 1, while the remaining five cases will be reported later. The Nusselt numbers presented here were normalized with a smooth tube correlation by Dittus-

Boelter/McAdams (Rohsenow and Choi [28]) for fully developed turbulent non-rotating tube flow:

$$Nu_o = 0.023\, Re^{0.8}\, Pr^{0.4}$$

4.1 Velocity and Temperature Fields

Figures 3 and **4** show the calculated temperature contours near the ribbed surfaces and at selected cross sections for the non-rotating case (case 1) listed in Table 1. It is seen that the coolant temperature increases gradually in the streamwise direction due to the heating of the channel walls. It is also noted that the temperature is relatively low near the center plane of symmetry, but increases gradually towards the side walls along the direction of the V-shaped ribs. The observed temperature distributions are closely related to the streamwise velocity and secondary flow patterns induced by the V-shaped ribs. It is seen that the ribs produce repeated flow separations and reattachment in the streamwise direction as shown in **Figure 5**. The temperature is high immediately downstream of each rib due to the flow separation behind the ribs. In the middle section between the ribs, however, the temperature is relatively low due to the impingement of cooler fluids in the flow reattachment zone.

Since the ribs are oriented at a negative 45° angle, the fluid near the center of the channel will reach the ribs first and moves along the ribbed surfaces toward the side walls as shown in **Figures 6** through 7. It then returns back to middle section of the channel along the centerline of the inclined cross-stream planes. It is clearly seen from **Figures 7(a)** and **8(a)** that the V-shaped ribs produced very strong tangential velocities which carried the cooler fluid from the center of the channel towards the side walls. On top of the ribs, the flow is nearly parallel to the ribbed

surfaces and the vertical velocity components are rather weak as seen in Figure 7(b). Behind the ribs, however, the vertical velocity components are significantly stronger as shown in Figure 8(b) due to the flow reattachment (impingement) between the ribs. In the same figure, one can also notice the early stage development of two pairs of counter-rotating vortices on top of the ribs (Figure 7b), which grow into four full symmetric counter-rotating vortices in the midsection of any two ribs (Figure 8b).

In order to provide a more detailed understanding on the heat transfer enhancement due to the V-shaped ribs, it is worthwhile to examine the secondary flow vectors and temperature contours at selected cross sections along the ribbed channel as shown in **Figure 9**. In the smooth section beofre the first rib, four pairs of corner vortices were generated as a result of the Reynolds stress anisotropy. On top of the first rib, these corner vortices were overpowered by two new pairs of rib-induced vortices. The strength of these four rib-induced vortices increased considerably in the middle section between the ribs. Along the streamwise direction, the size of these four counter-rotating vortices oscillates from the largest in the middle of each inter-rib distance to the smallest on the rib tops. This pattern keeps repeating until the last rib. The effect of the secondary flow on the temperature field is convecting the cooler fluid from the core region and along the ribbed surfaces towards the top and bottom surfaces (i.e., side walls). It then moves back along the sidewalls toward the center of the channel. This resulted in steep temperature gradients and high heat transfer coefficients on the ribbed surfaces as seen in the corresponding temperature contours.

Figure 10 shows the cross-stream velocity vectors and temperature contours for case 2 (Ro = 0.14 and $\beta = 90°$) at the same planes as in the non-rotating ribbed duct (case 1). Before the first

rib, the Coriolis force produced a cross-stream two-vortex flow structure similar to those observed in Al-Qahtani et al. [29] for the smooth rectangular duct (AR = 4:1). As the flow approaches the first rib, this Coriolis force induced secondary flow starts to distort the secondary flow induced by the V-shaped ribs. This effect can be clearly seen by comparing Figure 9 with Figure 8. From this comparison, the following conclusions can be drawn. (1) The magnitude of the Coriolis force induced secondary flow is weaker than the rib induced secondary flow. (2) The Coriolis force effect increases the size and strength of the two vortices adjacent to the trailing surface, while the other two vortices adjacent to the leading surface become weaker. (3) On top of the ribs, both vortices shrink in size and get distorted only near the side walls. The general effect of the Coriolis force induced secondary flow is to distort the rib-induced vortices. Consequently, the temperature contours are shifted toward the trailing surface, which affects the heat transfer coefficients from both the leading and trailing surfaces as seen from the corresponding temperature contour plot. The distortion of the temperature contours due to the Coriolis force can also be clearly seen from **Figure 11**.

Figure 12 shows the cross-stream velocity vectors and temperature contours for the $\beta = 45°$ case (case 3) at the same planes as in cases 1 and 2. In the smooth section before the first rib, the Coriolis force produce a secondary flow that pushes the cold fluid away from the corner of the leading and bottom surfaces. This produces two counter-rotating vortices with the one near the leading surface stronger than the one near the trailing surface. It is also noted that a smaller vortex is generated at the corner of the bottom and trailing surfaces and merged with the trailing vortex. As a result of this secondary flow, the fluid is pushed toward the top surface at which part of the secondary flow will move back along the trailing surface while the other part moves

along the leading surface such that they meet again at the leading corner. This flow pattern is qualitatively similar to that presented by Al-Qahtani et al. [29] for the $\beta = 135°$ smooth duct case, except that the flow direction is reversed.

Comparing Figure 12 with Figure 10, the following can be observed. Just before the ribbed section, the rotation induced secondary flow is still dominant as can be seen from the comparison between Figures 12(a) and 11(a). In the ribbed section, the rotation-induced secondary flow is combined with the rib-induced secondary flow to produce a larger vortex near the trailing and bottom surfaces. A net upward fluid motion from the bottom to the top surface was observed in the core region of the channel. The net effect of the secondary flow field is to push the cooler fluid towards the top surface as seen in the temperature contours shown in Figures 12(c)-(f).

4.2 Detailed Local Heat Transfer Coefficient Distribution

Figure 13 shows the local Nusselt number ratio contours of the ribbed leading and trailing surfaces, respectively. The non-rotating case in Figure 13(a) will be used as a baseline for comparison and discussion. The entrance and exit regions were cut to focus on the ribbed heated section. In Figure 13(a), the highest Nusselt number ratios were obtained near the tip of the V-shaped ribs, and the lower Nusselt number ratios were obtained right before and after the ribs. Between any two ribs, the Nusselt number ratios are highest near the middle section and decrease as we move towards the top and bottom surfaces. This is due to the rib induced secondary flow that moves from the middle of the channel (and parallel to the ribbed walls) to the side walls.

In Figures 13(b) and (c), the rotation number is 0.14 while the density ratio is kept fixed at 0.122. It is quite clear that the channel rotation leads to a significant decrease of the Nusselt number ratios on the leading surface in comparison with the non-rotating case. On the other

hand, the Nusselt number ratios were increased on the trailing surface due to the effects of channel rotation. It is also noted that the high Nusselt number ratios regions on the trailing surface are spreading toward the side walls. This is due to the rotation-induced secondary flow that pushes the cooler fluid towards the trailing surface and side walls as shown earlier in Figure 10.

4.3 Spanwise-Averaged Heat Transfer Coefficients and Comparison with Experimental Data

Figure 14 shows the spanwise-averaged Nusselt number ratios (Nu/Nu_o) for both the non-rotating and rotating cases (cases 1–3). The inlet coolant-to-wall density ratio was held constant at 0.122. In all three cases, the spanwise-averaged Nusselt number distributions on the leading and trailing surfaces show periodic spikes. The higher spikes which occur on the ribs tops are caused by the flow impingement on the ribs, and the lower spikes (which occur right before and after the ribs) are caused by the flow reattachment between the ribs. The Nusselt number ratios are high in the regions between the ribs. The Nusselt number ratios reached a peak value around the eighth rib. This phenomenon is caused by the rib-induced secondary flow becoming stronger along the duct.

As noted earlier, the channel rotation leads to an increase of Nusselt number on the trailing surface and a decrease of Nusselt number on the leading surface. The Nusselt number ratios were also increased on the top and bottom surfaces as a result of the secondary flow impingement on the side walls. However, the overall rotation effects are quite small at Ro = 0.14 when comparing to the heat transfer enhancement caused by the rib-induced flows. The change of channel orientation from $\beta = 90°$ to 45° leads to an increase of Nusselt number ratios on the top surface, but it has only minor effects on the leading and trailing surfaces.

5. CONCLUSIONS

A multi-block RANS method was employed to predict three-dimensional flow and heat transfer in a rotating smooth and AR = 4:1 rectangular channel with V-shaped ribs. It predicted fairly well the complex three-dimensional flow and heat transfer characteristics resulting from the large channel aspect ratio, rotation, centrifugal buoyancy forces and channel orientation. The main findings of the study may be summarized as follows.

1. The V-shaped ribs start four counter-rotating vortices that oscillate in size along the streamwise direction. For the non-rotating case, the secondary flow results in steep temperature gradients and high heat transfer coefficients on both the ribbed surfaces and side walls.
2. For rotating cases, the rotation-induced cross-stream secondary flow distorts the rib-induced vortices and affects the heat transfer coefficients from both the leading and trailing surfaces.
3. The effect of channel orientation is fairly small for the low rotation number cases considered here. However, additional studies are needed to investigate the channel orientation effects for higher rotation number and higher coolant-to-wall density ratio cases.

ACKNOWLEDGEMENT

The project was also supported by the DOE Advanced Gas Turbine Systems Research (AGTSR) Program through project number SR-094. The computations were performed on the SGI Origin 3800 at the Texas A&M Supercomputer Center under a supercomputer research grant, and Cray C90 of Cray Research Inc. under the sponsorship of Frank Kampe. The

GRIDGEN software was supported by Pointwise Inc. The support of all of the above institutions is greatly appreciated.

REFERENCES

1. Han, J. C. and Park, J. S., 1988, "Developing Heat Transfer in Rectangular Channel with Rib Turbulators," Int. J. Heat and Mass Transfer,. **31**, No. 1, pp. 183-195.
2. Han, J. C., Zhang, Y. M. and Lee, C. P., 1991, "Augmented Heat Transfer in Square Channels with Parallel, Crossed, and V-Shaped Angled Ribs," ASME Journal of Heat Transfer, **113**, pp. 590-596.
3. Ekkad S.V. and Han, J. C., 1997, "Detailed Heat Transfer Distributions in Two-pass square Channels with Rib Turbulators," Int. J. Heat and Mass Transfer,. **40**, No.11, pp. 2525-2537.
4. Liou T.-M. Tzeng, Y.-Y., and Chen, C.-C., 1998, "Fluid Flow in a 180 Deg Sharp Turning Duct with Different Divider Thicknesses," ASME Paper 98-GT-189.
5. Wagner, J. H., Johnson, B. V. and Kopper, F. C., 1991, "Heat transfer in Rotating Serpentine Passage with Smooth Walls", ASME J. of Turbomachinery, **113**, No. 3, pp.321-330
6. Dutta, S. and Han, J. C., 1996, "Local Heat Transfer in Rotating Smooth and Ribbed Two-Pass Square Channels with Three Channel Orientations", ASME J. of Heat Transfer, **118**, No.3, pp. 578-584.
7. Soong, C. Y., Lin, S. T., and Hwang, G. J., 1991, "An Experimental Study of Convective Heat Transfer in Radially Rotating Rectangular Ducts," ASME J. of Heat Transfer, **113**, pp. 604-611.

8. Azad, GM S., Uddin, M. J., Han, J. C., Moon, H. K., and Glezer, B., 2001, “Heat Transfer in Two-Pass Rectangular Rotating Channels with 45° Parallel and Crossed Rib Turbulators” ASME Paper 2001-GT-0186.
9. Wagner, J. H., Johnson, B. V., Graziani, R. A., and Yeh, F. C., 1992, “Heat Transfer in Rotating Serpentine Passages with Trips Normal to the Flow,” ASME J. of Turbomachinery, **114**, No. 4, pp. 847-857.
10. Johnson, B. V., Wagner, J. H., Steuber, G. D., and Yeh, F. C., 1994a, “Heat Transfer in Rotating serpentine Passage with Trips Skewed to the Flow,” ASME J. of Turbomachinery, **116**, pp. 113-123.
11. Johnson, B. V., Wagner, J. H., Steuber, G. D., and Yeh, F. C., 1994b, “Heat Transfer in Rotating serpentine Passage with selected Model Orientations for Smooth or Skewed Trip Walls,” ASME J. of Turbomachinery, **116**, pp. 738-744.
12. Parsons, J. A., Han, J. C., and Zhang, Y. M., 1995, “Effects of Model Orientation and Wall Heating Condition on Local Heat Transfer in a Rotating Two-Pass Square Channel with Rib Turbulators,” Int. J. Heat Mass Transfer, **38**, No.7, pp. 1151-1159.
13. Zhang, Y. M., Han, J. C., Parsons, J. A., and Lee, C. P., 1995, “Surface Heating Effect on Local Heat Transfer in a Rotating Two-pass Square Channel with 60 deg Angled Rib Turbulators,” ASME J. of Turbomachinery, **117**, pp. 272-280.
14. Griffith, T. S., Al-Hadhrami, L. and Han, J. C., 2001, “Heat Transfer in Rotating Rectangular Cooling Channels with Angled Ribs,” AIAA Paper 2001-2820.
15. Stephens, M. A., Shih, T. I-P., and Civinskas, K. C., 1995, “Computation of Flow and Heat Transfer in a Rectangular Channel with Ribs,” AIAA Paper 95-0180.

16. Stephens, M. A., Chyu, M. K., and Shih, T. I-P., 1996, “Computation of Convective Heat Transfer in a Square Duct with Inclined Ribs of Rounded Cross Section,” ASME Paper 96-WA/HT-12.
17. Stephens, M. A. and Shih T. I-P., 1997, “Computation of Compressible Flow and Heat Transfer in a Rotating Duct with Inclined Ribs and 180Deg Bend,” ASME Paper 97-GT-192.
18. Prakash, C. and Zerkle, R., 1995, “Prediction of Turbulent Flow and Heat Transfer in a Ribbed Rectangular Duct with and without Rotation,” ASME J. of Turbomachinery, **177**, pp. 255-264.
19. Bonhoff, B., Tomm, U., Johnson, B. V. and Jennions, I., 1997, “Heat Transfer Predictions For Rotating U-Shaped Coolant Channels with Skewed Ribs and with Smooth Walls,” ASME Paper 97-GT-162.
20. Iacovides, H., 1998, “Computation of Flow and Heat Transfer Through Rotating Ribbed Passage,” International J. of Heat and Fluid Flow, **19**, pp. 393-400.
21. Chen, H. C., Jang, Y. J., and Han, J. C., 2000, “Computation of heat transfer in rotating two-pass square channels by a second-moment closure model,” Int. J. Heat and Mass Transfer, **43**, No. 9, May, pp.1603-1616
22. Chen, H. C., Jang, Y. J., and Han, J. C., 2000, “Near-Wall Second-Moment Closure for Rotating Multi-pass Cooling Channels,” Journal of Thermophysics and Heat Transfer, **14**, No. 2, pp.201-209.
23. Jang, Y. J., Chen, H. C., and Han, J. C., 2001a, “Computation of Flow and Heat Transfer in Two-Pass Channels with 60° Ribs,” ASME J. of Heat Transfer, **123**, No. 3, pp. 563-575.

24. Jang, Y. J., Chen, H. C., and Han, J. C., 2001b, “Numerical Prediction of the Flow and Heat Transfer in a Two-Pass Square Duct with 90° Ribs,” *International Journal of Rotating Machinery*, Vol. 7, No. 3, pp. 195-208.
25. Jang, Y. J., Chen, H. C., and Han, J. C., 2001c, “ Flow and Heat Transfer in a Rotating Square Channel with 45° Angled Ribs by Reynolds Stress Turbulence Model,” ASME J. of Turbomachinery, **123**, No. 1, pp. 124-132.
26. Al-Qahtani, M. S., Jang, Y. J., Chen, H. C., and Han, J. C., 2001, “Prediction of Flow and Heat Transfer in Rotating Two-Pass Rectangular Channels with 45° Rib Turbulators,” ASME Paper 2001-GT-0187.
27. *GRIDGEN User Manual*, Version 13.3, Pointwise Inc., 1999.
28. Rohsenow, W. M., and Choi, H., 1961, *Heat, Mass and Momentum Transfer,* Prentice-Hall, Englewood Cliffs, NJ.
29. Al-Qahtani, M. S., Chen, H. C., and Han, J. C., 2002, “A Numerical Study of Flow and Heat Transfer in Rotating Rectangular Channels (AR = 4) with 45° Rib Turbulators by Reynolds Stress Turbulence Model,” ASME Paper GT-2002-GT-30216.

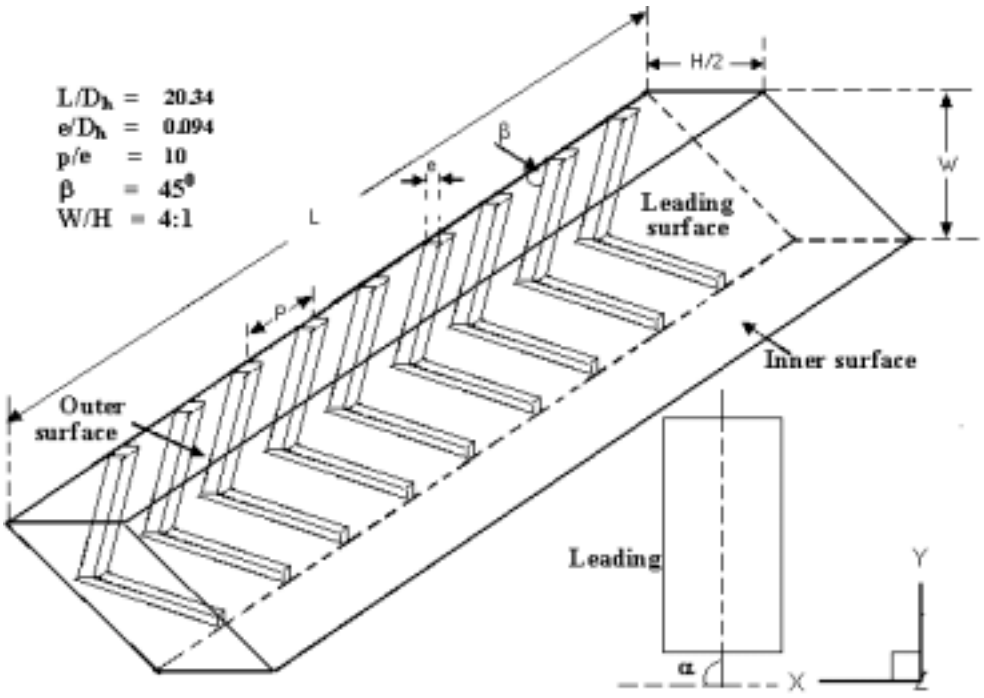

Figure 1. Geometry of AR = 4:1 rectangular duct with V-shaped ribs.

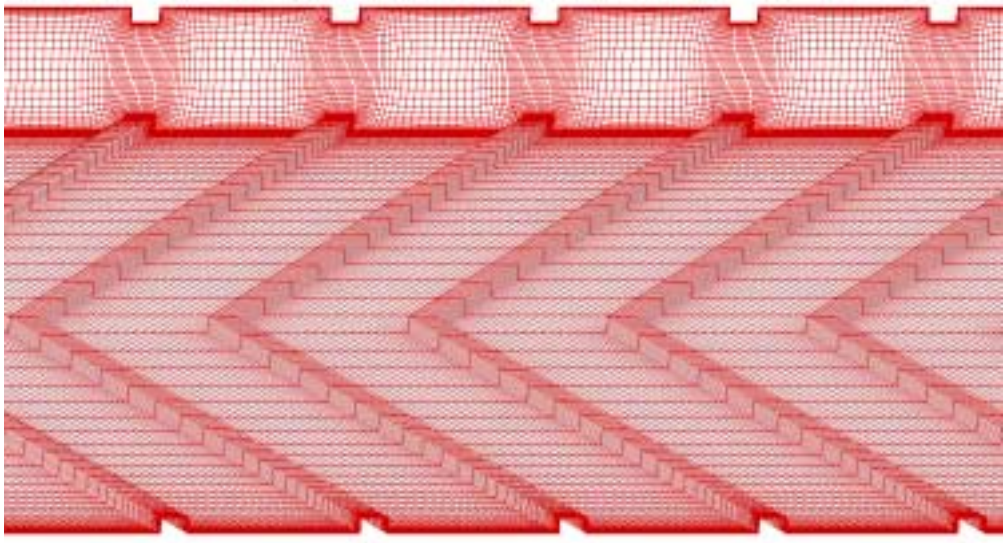

Figure 2. Computational grid of AR = 4:1 rectangular duct with V-shaped ribs.

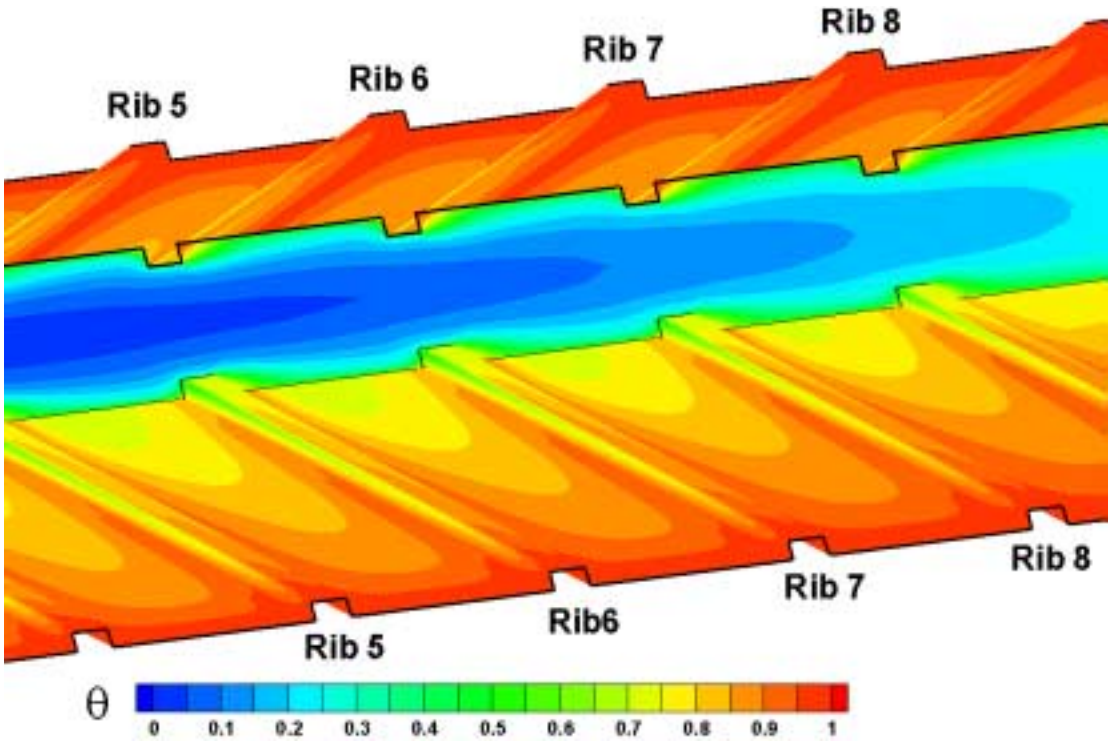

Figure 3. Temperature [$\theta = (T - T_o)/(T_w - T_o)$] contours for non-rotating channel near the rib surface and along the center plane of symmetry.

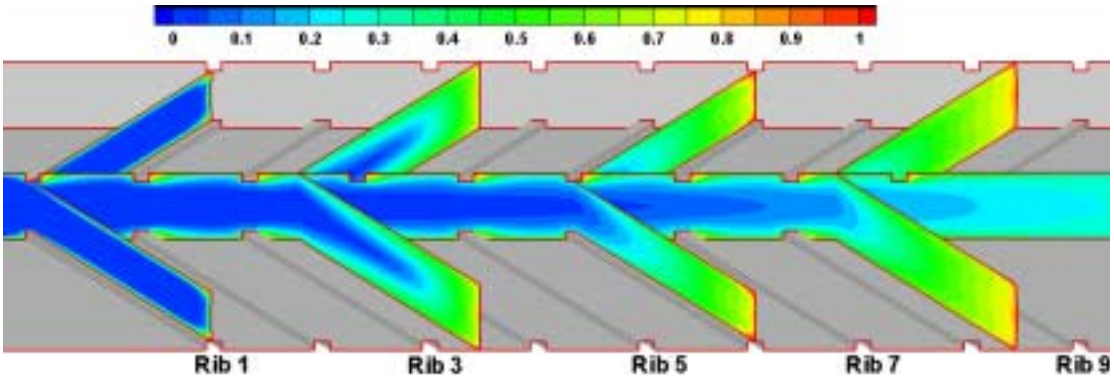

Figure 4. Temperature [$\theta = (T - T_o)/(T_w - T_o)$] contours for non-rotating ducts at selected cross sections.

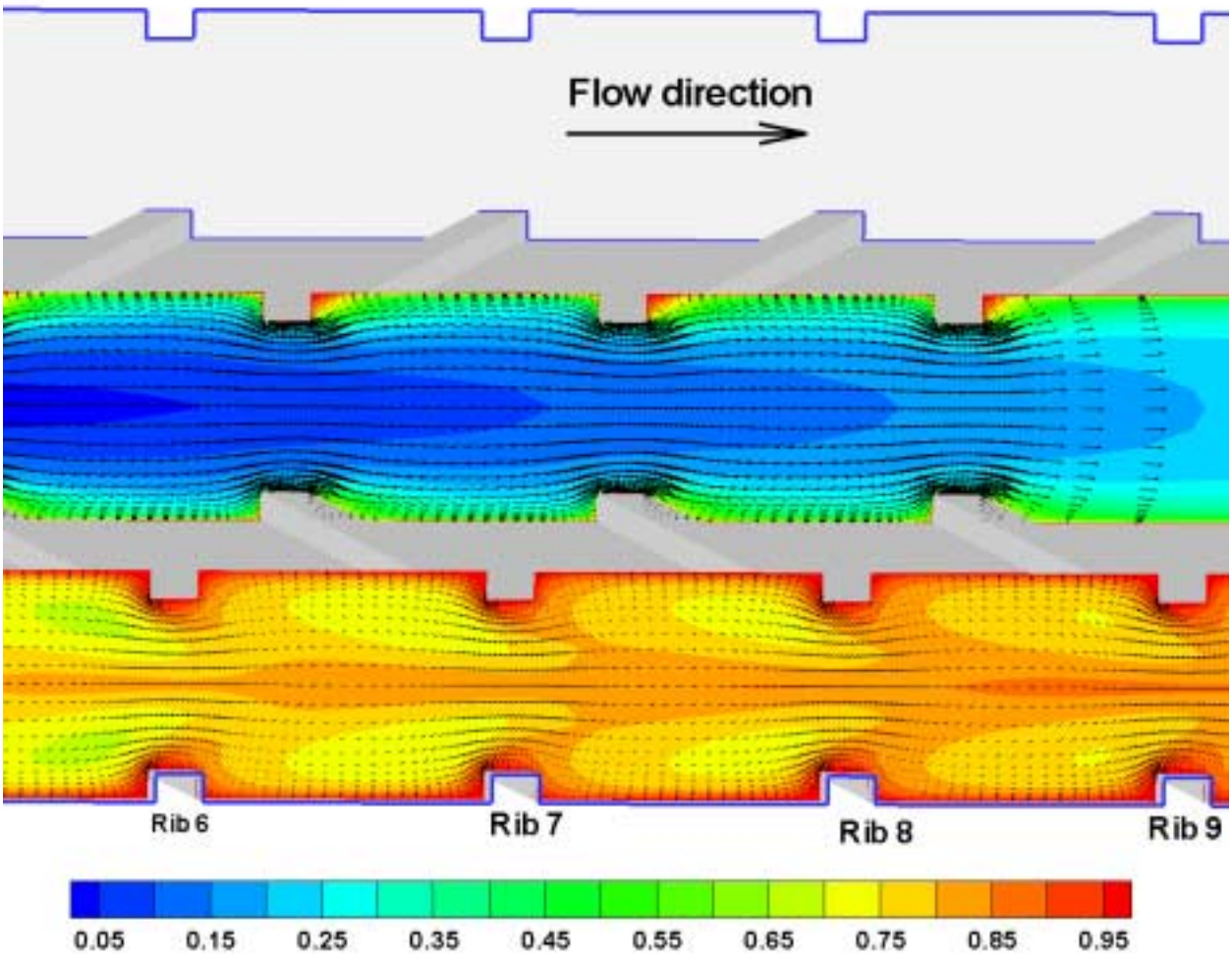

Figure 5. Streamwise velocity vectors and temperature [$\theta = (T - T_o)/(T_w - T_o)$] contours for non-rotating channel.

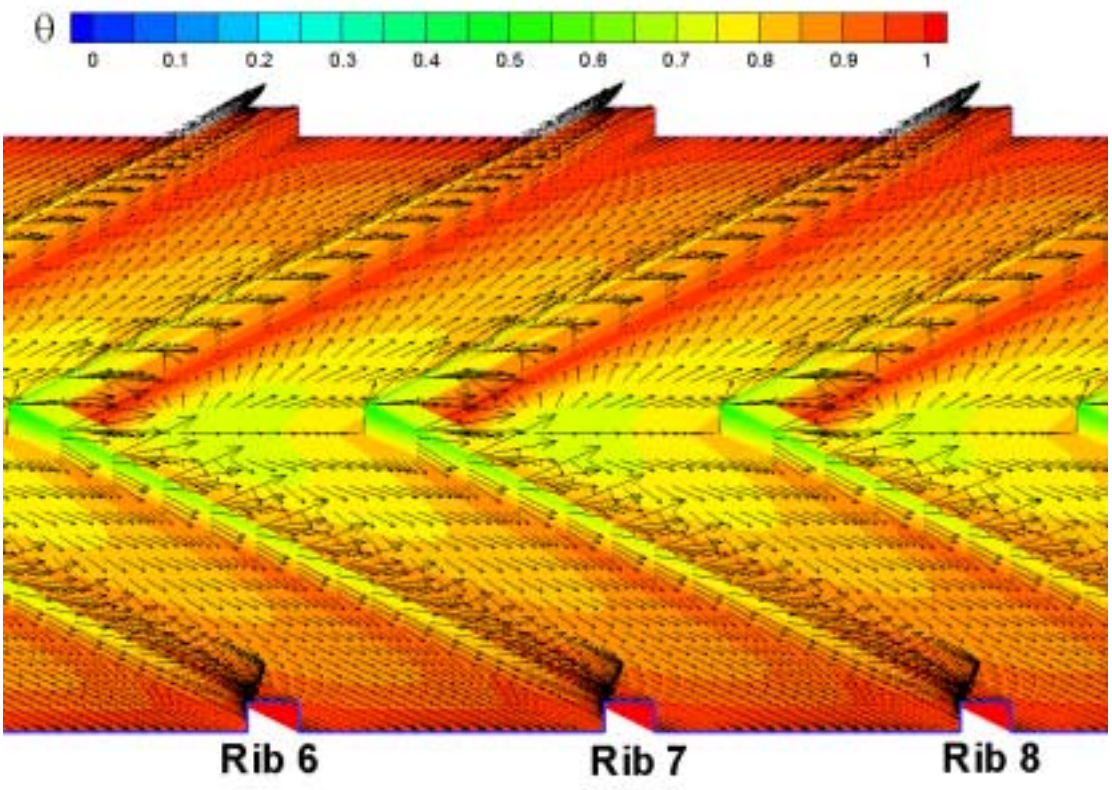

Figure 6. Velocity vectors and dimensionless temperature [$\theta = (T - T_o)/(T_w - T_o)$] contours close to the rib surface; Ro = 0.

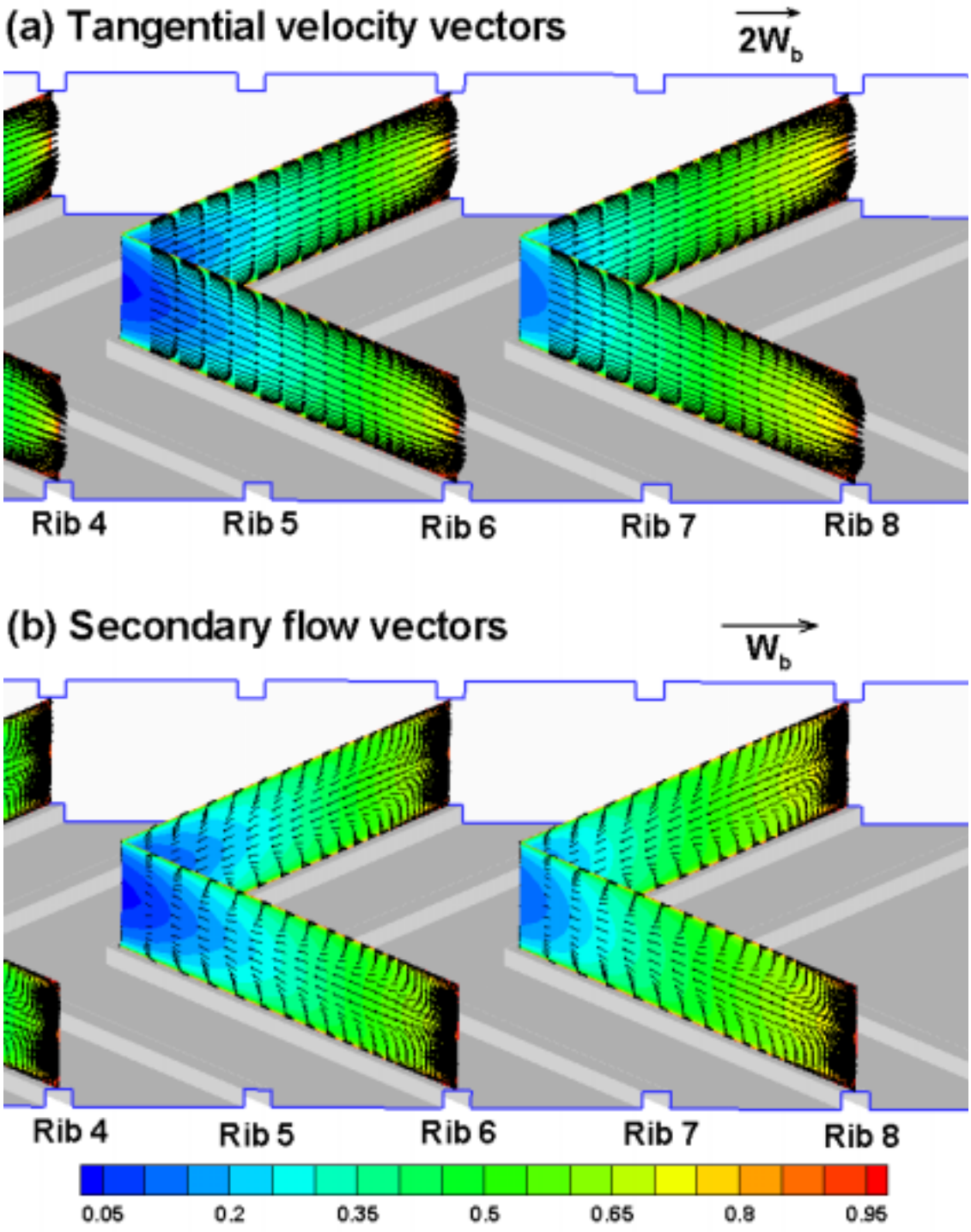

Figure 7. Secondary flow vectors and temperature [$\theta = (T - T_o)/(T_w - T_o)$] contours on top of the V-shaped ribs, Ro = 0

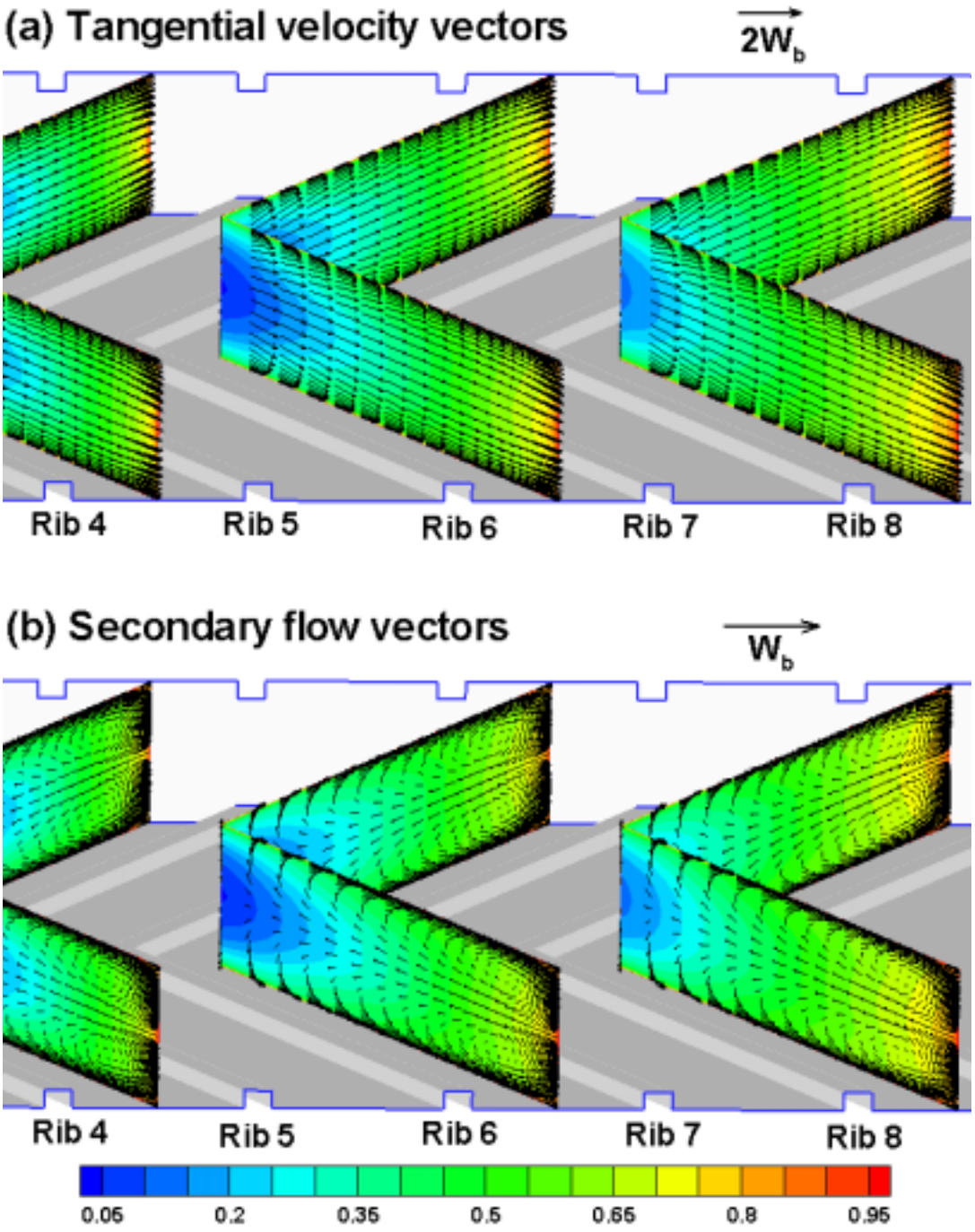

Figure 8. Secondary flow vectors and temperature [$\theta = (T - T_o)/(T_w - T_o)$] contours between the V-shaped ribs, Ro = 0

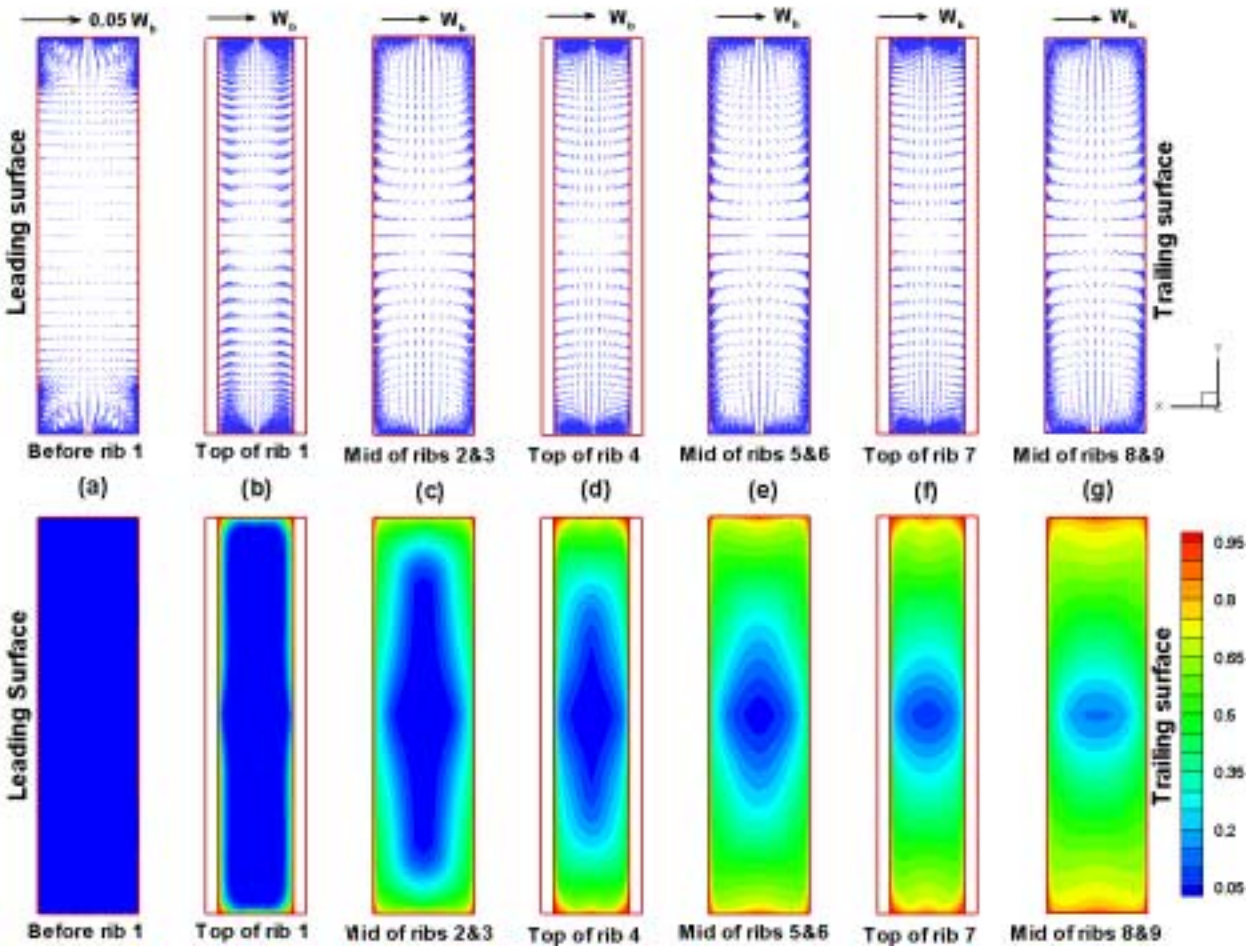

Figure 9. Secondary-flows and dimensionless temperature [$\theta = (T - T_o)/(T_w - T_o)$] for non-rotating ribbed channel.

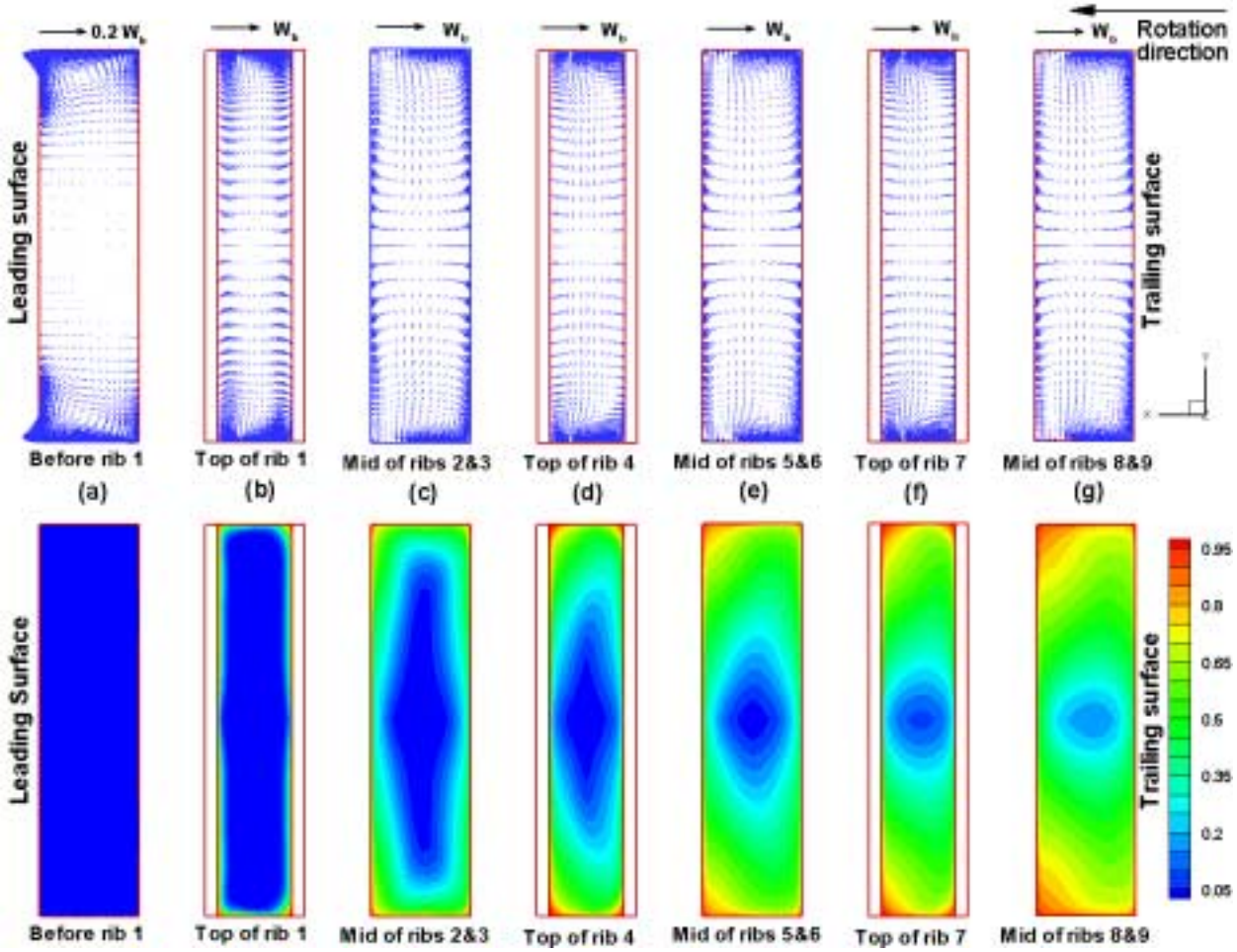

Figure 10. Secondary flow and temperature [$\theta = (T - T_o)/(T_w - T_o)$] for rotating ribbed channel, Ro = 0.14 and $\beta = 90°$.

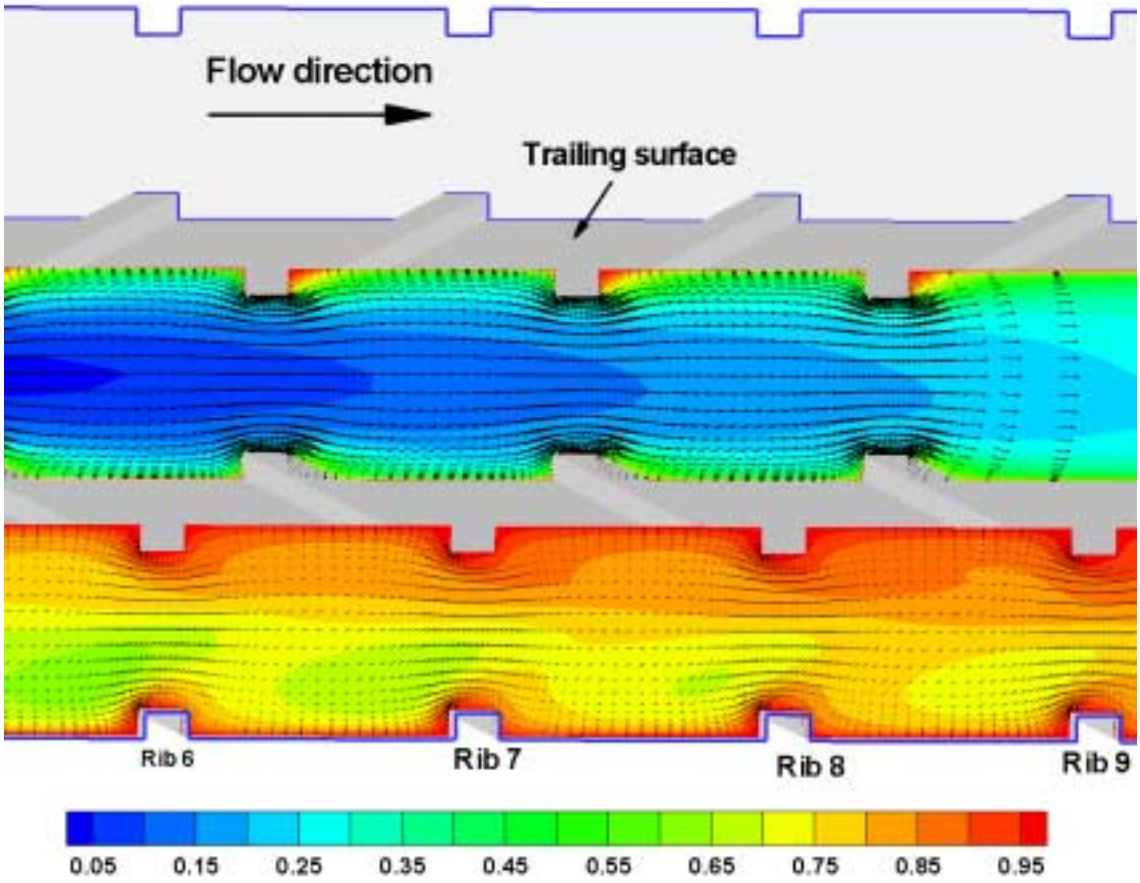

Figure 11. Streamwise velocity vectors and temperature [$\theta = (T - T_o)/(T_w - T_o)$] contours for rotating ribbed channel; Ro = 0.14 and $\beta = 90°$.

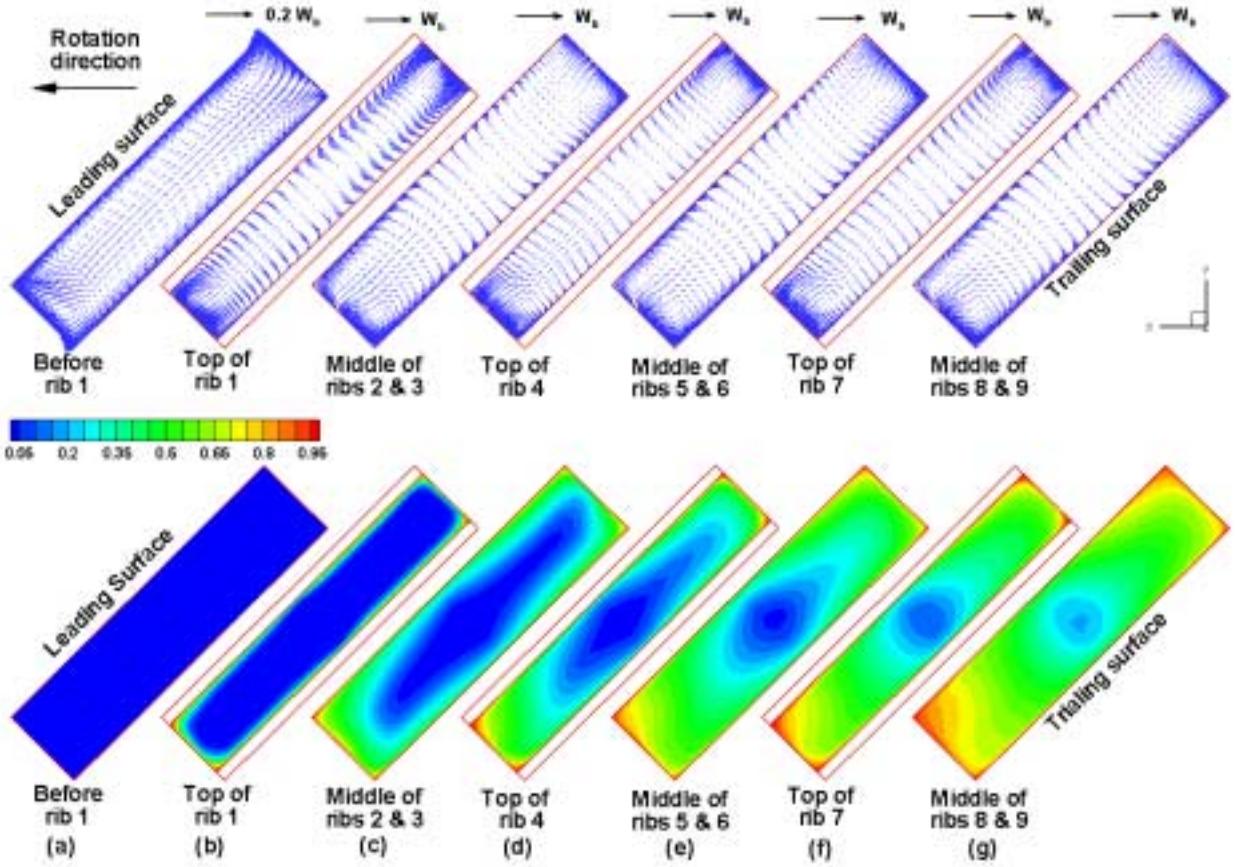

Figure 12. Secondary flow and temperature [$\theta = (T - T_o)/(T_w - T_o)$] for rotating ribbed channel, Ro = 0.14, $\Delta\rho/\rho = 0.122$ and $\beta = 45°$.

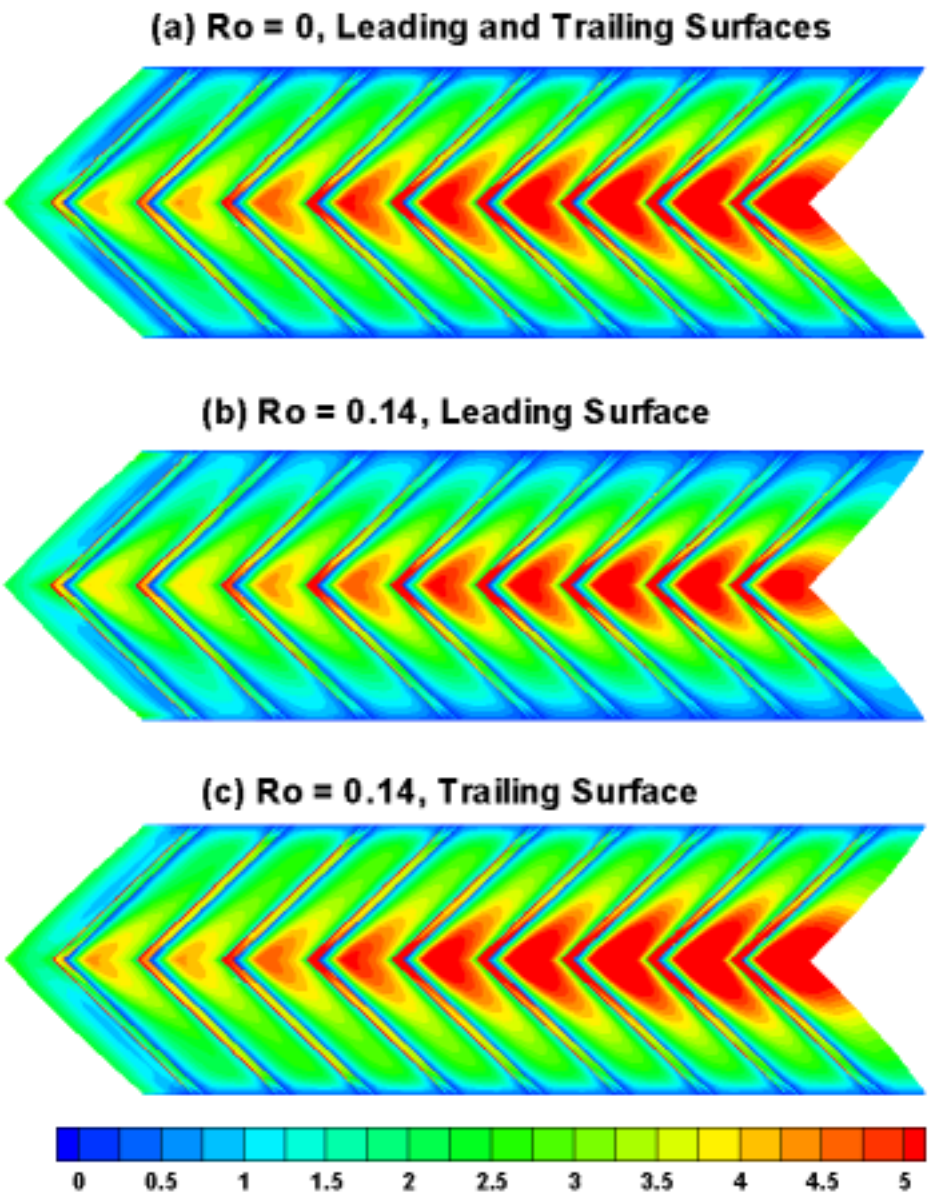

Figure 13. Detailed Nusselt number ratio distribution in ribbed channel

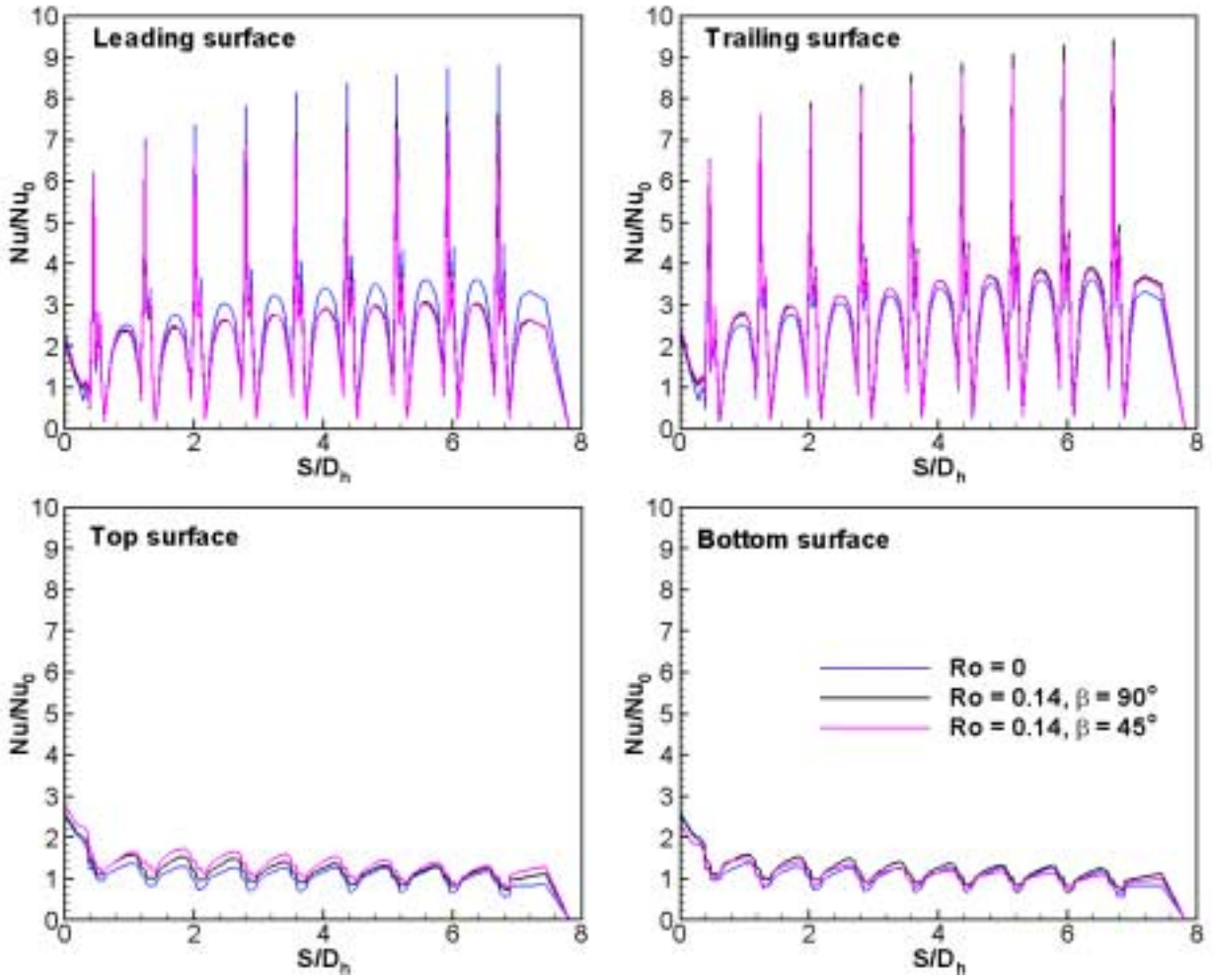

Figure 14. Calculated Nusselt number ratio distribution for AR = 4:1 rectangular channel with V-shaped ribs.

ONGOING WORK

Part I: Rotating Heat Transfer

- Design, fabricate and instrument a two-pass smooth wall rectangular channel with an aspect ratios of 2:1 (AR = a/b = 2:1).
- Measured local heat transfer distributions and pressure drops in the smooth wall rectangular channels for the effects of Reynolds number (Re = 10,000-100,000), Rotation number (Ro = 0-0.4), Coolant to wall temperature ratio (TR = 0.8-0.9), and rotating angle ($\gamma = 90^0$ and 135^0).
- Have done the effect of rotation in a two-pass rectangular channel with aspect ratio of 2:1 with five different V-shaped rib turbulators for two rotating channel orientations as showed in this report.
- Have done the effect of rotation in a two-pass rectangular channel with aspect ratio of 2:1 with three high performance turbulence promoters (broken angled ribs, broken V-shaped ribs) for two rotating channel orientations as showed in this report.
- Correlate the new data and compare with the existing data (AR = 1:1).
- Compare with predictions in part II for rotating channels.

Part II: Computational Study

- Calculate flow field, heat transfer coefficients and pressure drops in the rectangular channels with V-shaped ribs for higher rotation number, higher coolant to wall temperature ratio cases using two-layer k-ε model and second moment closure model.
- Calculate flow field, heat transfer coefficients and pressure drops in the rectangular channels with V-shaped ribs for different channel orientations by the two-layer k-ε model and second moment closure model.
- Validate the numerical predictions with above-mentioned flow, heat transfer, and pressure drop measurements (part I) for assessment of the general performance of RANS code and turbulence models.
- Extend above-mentioned calculations for a very high Reynolds numbers (Re = 100,000 and 500,000) and buoyancy parameter (Bo = 10) conditions.
- Have done the effect of rotation in a 4:1 aspect ratio rectangular channel with V-Shaped ribs for three channel orientations as shown in this report.